DESIGN OPTIMIZATION OF COMPRESSION STOCKINGS BASED ON FLUID-STRUCTURE INTERACTION MODELING

YE CHONGYANG

PhD

The Hong Kong Polytechnic University

2024

The Hong Kong Polytechnic University

School of Fashion and Textiles

Design Optimization of Compression Stockings Based on Fluid-Structure Interaction Modeling

Ye Chongyang

A thesis submitted in partial fulfillment of the requirements for the degree of Doctor of Philosophy

August 2023

CERTIFICATE OF ORIGINALITY

I hereby declare that this thesis is my own work and that, to the best of my knowledge and belief, it reproduces no material previously published or written, nor material that has been accepted for the award of any other degree or diploma, except where due acknowledgement has been made in the text.

(Signed):

(Name of student): Ye Chongyang

ABSTRACT

Compression textiles have been widely applied for the prevention and treatment of venous disorders (e.g., deep vein thrombosis, leg ulcers, lymphedema, and superficial phlebitis) through the designed external pressure system. Elastic compression stockings (ECSs) are one of typical types of compression textiles for reduction of venous hypertension and promotion of venous return. However, limited studies develop numerical simulation methods combined with transmission mechanism analysis to systematically predict interface pressure in the ECS-leg system. The integration of the numerical simulation and optimization approach to determine sensitive design parameters of the ECS-leg system for achieving the target pressure levels is few reported. The aim of this study is to construct a numerical model combined with the experimental validation for the investigation of interface pressure, stress transmission, and venous hemodynamics induced by ECSs with different pressure designs based on our determined ECS and tissue properties and constructed geometric models. Based on the simulation results, an optimization system was obtained to optimize design parameters for required pressure function.

This thesis consists of six parts to achieve these objectives. The first part is to construct an analytic model to determine the ECS mechanical properties in a three-dimensional (3D) scale to improve and optimize the simulation precision of the pressure. The second part is to construct the geometric leg models of three subjects using reverse engineering technology based on the magnetic resonance imaging. The third part is to construct the finite element model (FEM) for three subjects to

numerically simulate the mechanical performances of ECS-leg system based on the determined material properties and the constructed geometric models. Both the referred and determined leg tissue properties were applied in our developed FE models. A good agreement existed between the simulated and the experimental pressure data, especially for the results by using the determined tissue properties. In addition, tissue stresses gradually decreased from the skin surface to the deeper soft tissues till vein walls, which influenced the venous hemodynamic responses. The fourth part is to construct a fluid-solid interaction (FSI) model with experimental validation to numerically simulate hemodynamic responses in the ECS-leg system. The results showed that the venous flow velocities appeared an increased trend with the increased interface pressure by ECSs. The fifth part is to assess the subjective comfort perception towards the pressure applied by the ECSs with the aid of statistical analysis. The last part is to develop an optimization approach to determine the optimal fabric parameters for achieving a balanced mechanical function and wearing comfort of ECSs based on our developed FE and FSI ECS-leg system.

This study provides a novel method to optimize the design of ECS products through numerical analysis and modelling of the lower limbs, tissue properties, and ECS material properties. This study not only investigated the mechanical interaction of the ECSs and lower limbs, but also improved the simulation precision of the ECS-leg system, which enhance the understanding of the mechanisms underlying the interactions between elastic compression textiles and the human body, thereby facilitating compression material optimization and pressure dose control for improved compression therapeutic efficacy.

ACKNOWLEDGEMENTS

I am extremely grateful to my chief supervisor, Dr. Rong Liu, for her kind guidance, professional comments, and patience for my PhD studies. I would like to extend my sincere gratitude to my co-supervisor, Prof. Michael Ying, who provided some supports and necessary comments in the experimental testing. As well, I would like to sincerely thank my co-supervisor, Prof. Fuyou Liang, for his guidance in some research methodology.

I also would like to thank my colleagues, Dr. Lingxiao Jing, Dr. Xinbo Wu, Dr. Shumi Zhao, Ms. Yu Shi, Mr. Chenghe Dong, Ms. Luoling Gu, Ms. Joyce Liu, Mr. Andy Ho, and Mr. Mohiuddin Choudhry for their comments and help. I would like to thank all staff and students in the Hong Kong Polytechnic University to give me the support and environment through the studies.

PUBLICATIONS ARISING FROM THE THESIS

Journal papers:

● Ye, C., Liu, R., Wu, X., Liang, F.Y., Ying, M.T., & Lv, J. (2022). New Analytical Model and 3D Finite Element Simulation for Improved Pressure Prediction of Elastic Compression Stockings. *Materials & Design,* 217, 110634.

● Ye, C., Liu, R., Ying, M.T., Liang, F.Y., & Shi, Y. (2023). Characterizing the Biomechanical Transmission Effects of Elastic Compression Stockings on Lower Limb Tissues by Using 3D Finite Element Modelling. *Materials & Design,* 232, 112182.

● Shi, Y., Ye, C., & Liu, R. (2024). A Novel Optimization Approach for Bio-design of Therapeutic Compression Stockings with Pressure Fit. *Computers in Biology and Medicine,* 168, 107768. (Co-first author).

● Shi, Y., Liu, R., Lv, J., & Ye, C. (2024). Biomedical Therapeutic Compression Textiles: Physical-mechanical Property Analysis to Precise Pressure Management. *Journal of the Mechanical Behavior of Biomedical Materials,* 151,106392.

● Zhao, S., Liu, R., Wu, X., Ye, C., & Zia, A. W. (2020). A Programmable and Self-adaptive Dynamic Pressure Delivery and Feedback System for Efficient Intermittent Pneumatic Compression Therapy. *Sensors and Actuators A: Physical*, 315, 112285.

● Ye, C., & Liu, R. (2020). Biomechanical Prediction of Veins and Soft Tissues beneath Compression Stockings Using Fluid-Solid Interaction Model[J]. *International Journal of Biomedical and Biological Engineering*, 14(10): 285-290.

● Ye, C., & Liu, R. (2023). Determination of Poisson’s Ratio and Elastic Modulus of Compression Textile Materials. *International Journal of Materials and Textile Engineering*, 17(2), 23-26.

Book chapter:

● Liu, R., Xu, B., & Ye, C. (2020). Biodigital Design and Functional Visualization of Multi-Class Personalized Compression Textiles for Ergonomic Fit. *Advances in Design for Inclusion.* Proceedings of the AHFE 2019 International Conference on Design for Inclusion and the AHFE 2019 International Conference on Human Factors for Apparel and Textile Engineering, 24th-28th July, 2019, Washington DC, USA 10, 488-499. Springer International Publishing.

Conference paper:

● Ye, C., Liu, R. (2020). 3D Fluid-Solid Interaction Model for Pressure Transmission and Hemodynamics Analysis of Customized Elastic Compression Stockings. *Digital Fashion Innovation*, 28th-30th Sept., 2020, Manchester, UK.

CONTENTS

List of Tables

List of Figures

LIST OF ABBREVIATIONS

0-D Zero-dimensional

1-D One-dimensional

2-D Two-dimensional

3-D Three-dimensional

AVF Average venous flow

CAD Computational fluid dynamics

CFD Computational fluid dynamics

CVI Chronic venous insufficiency

DRO Deviation ratios

DOF Degree of freedoms

DUR Doppler ultrasound test

ECS Elastic compression stocking

FEM Finite element model

FSI Fluid-solid interaction

GSV Great superficial vein

KEF Knitted elastic fabrics

MRI Magnetic resonance imaging

KES Kawabata evaluation system

OCM Orthotropic compliance matrix

POV Popliteal vein

PV Peroneal vein

RSM Response surface model

SSV Small superficial vein

TE Echo time

TR Time of repetition

UDF User Defined Function

CHAPTER 1 INTRODUCTION

1.1 Research Background

Compression textiles have been widely applied to prevent and treat venous disorders, e.g., deep vein thrombosis, leg ulcers, lymphedema, and superficial phlebitis, through the designed external pressure system (Liu, et al. 2017; Lattimer, et al. 2016; Li, et al. 2006). Elastic compression stockings (ECSs) are one of typical types of compression textiles for reduction of venous hypertension (Partsch, et al. 2012) and promotion of venous return (Mosti, et al. 2010). Based on the clinical reports (Li, et al. 2006), high non-compliance of ECSs occurred in patients' use, resulting from "pain", "discomfort", or "ill-fitting" (Liu, et al. 2017; Tandler, et al. 2016; Raju, et al. 2007). However, few systematical pressure strategies are available to guide ECSs design to address the aforementioned problems**.**

The existing finite element (FE) models show the capabilities to analyze and simulate the mechanical performances of various functional textile/garment products (e.g., ECSs, gloves, and bras) (Liu, et al. 2006; Yu, et al. 2016; Liang, et al. 2019). Subject-specific FE models have been developed to analyze various biomechanical objects in the fields of medical assistant technologies and healthcare devices. The application of subject-specific FE models in ECS analysis can be traced back in the early 2000s. The existing ECS-FE models assumed materials to be homogenous and linearly elastic (Avril, et al. 2010; Dubuis, et al. 2012), and the effects of different pressure levels and profiles by ECSs on skin pressure, tissue stress, and venous flow have not been fully understood. Rohan et al. and Wang et al. developed two-dimensional (2D) FE models to predict ECSs pressure on deep veins of the calf to analyze displacement boundary conditions of vein caliber deformation and further studied the effects on wall shear stress of veins using the computational fluid dynamics (CFD) models (Downie, et al. 2008; Rohan, et al. 2015; Wang, et al. 2013). However, the working mechanisms of elastic compression with different material moduli and pressure designs on skin pressures and underlying venous flows on different aged subjects were not fully reported.

Experimental methods were proposed to determine the plane Young's modulus, Poisson's ratio, and shear modulus in 2D scales (Zhou, et al. 2010). For example, Hursa et al. presented a digital image correlation method to determine the Poisson's ratio of the woven fabric in the *x* and *y* axes directions during the uniaxial tensile test (Hursa, et al. 2009). Experimental approaches (e.g., optical method, Kawabata evaluation system (KES) system, and Instron system) and basic theoretical analysis (e.g., orthotropic Hooke's Law and Laplace's Law) were applied to quantify the elastic moduli of knitted elastic fabrics (KEFs). However, some limitations remain exist. For example, Gotoh et al. studied the plane stress to analyze the elastic modulus of KEFs worn on the human bodies (Gotoh, et al. 1977). Gommers et al. proposed a theoretical model to determine the Young's modulus and Poisson's ratio based on the rule of mixtures with a consideration of a plane stress problem (Gommers, et al. 1996), Huang et al. further determined the Young's modulus and Poisson's ratio with consideration of the laminated composites via plane stress problem (Huang, et al. 2004), and Liu et al. considered the failure conditions in a 3D scale of the KEF based on the plane stress problem (Liu, et al. 2017). Recently, Balcioglu et al. combined the laminated composites theories and tensile, compressive and shear loads testing to assess the mechanical properties of the KEFs (Balcioglu, et al. 2021). However, the determination of the mechanical properties of the elastic compression knitted fabrics in a three-dimensional (3D) scale remains attract less attention. The plane stress cannot reflect the real deformation of the elastic fabrics during dynamic wear three-dimensionally (i.e., along wale, course, and thickness directions), which would result in a certain deviation in pressure simulation. A referable approach to determine Young's modulus, Poisson's ratio, and shear modulus in a 3D scale of the garment pressure distributions is, therefore, highly necessary to improve the simulation efficiency for the ECS design optimization.

Interface pressure between the ECSs and the lower limb could be determined by formula calculation using Laplace's law or the modified Laplace's Law (Barhoumi, et al. 2020), or by applying pressure sensors (actuators), or FE modeling and simulation (Finnie, et al. 2000; Stolk, et al. 2004; Liu, et al. 2005). Internal stress transmission from the skin to the deeper underlying tissues largely determines the pressure function of ECSs in practical use, which further reflects the effects of the mechanical forces applied to the venous walls relating to hemodynamics. However, there is no available reports to reveal the effects of KEF materials and tissue properties on the stress transmission among different subjects. Moreover, the determination of venous hemodynamics induced by ECSs remains challenging. The previous studies applied a zero-dimensional (0D) or one-dimensional (1D) model to predict venous hemodynamic properties (Shi, et al. 2011). The venous velocity was usually measured by using Doppler ultrasound (Bonnefous, et al. 1986; Stuart, et al. 1980; Hoskins, et al. 1999). However, these existing models did not take the effects of soft tissue properties and venous positions into account. Moreover, few studies addressed the essential question relating to the effects of ECSs on venous hemodynamic properties including flow velocity and wall shear stress in the 3D leg models. To address the aforementioned limitations, in this thesis study, a fluid-solid interaction model will be constructed to predict and analyze interface pressure and its biomechanical transmission effects of ECSs, including venous velocity, wall shear stress, and venous pressure, induced by ECSs with different structural and properties design, thus guiding the design optimization of ECSs in terms of materials, pressure, and functional performances. Moreover, to further facilitate material selections and user applications, a parameter optimization method integrated with the sensitive analysis were developed to determine the sensitive parameters and their quantitative ranges in a ECS-leg system for achieving the expected pressure levels for individual end users.

1.2 Research Objectives

The aim of this study was to investigate the mechanical performance of the interface pressure and tissue stress between the lower limb and ECSs, as well as the stress transmission from the skin surface to the underlying bones and deeper tissues (including venous system) effected by the ECSs with different pressure design, and to build optimized materials parameters combinations for the expected pressure design. The study work contributions to enhance fundamental understanding of the compression textiles applied in compression therapy and also provides a referable technology to design functional pressure for improved leg health. The research objectives include,

to analyze and determine physical-mechanical properties of ECS fabrics in two- and three-dimensions;

to build finite element model to characterize the mechanical transmission effects of ECS fabrics from the skin to the deeper soft tissues of lower limb;

to build fluid-solid coupling model to analyze venous hemodynamics effects of the lower limb applied by the ECS fabrics;

to develop optimization algorithms to determine the optimal fabric parameters for achieving a balanced mechanical function and wearing comfort of ECSs.

1.3 Research Methodology

To achieve the objectives as aforementioned, the major research methodologies were applied in the follows three sections. Section 1 presented the development of the FE model of ECS-leg system; Section 2 presented the development of the fluid-solid interaction (FSI) model; Section 3 presented the development of the ECS material optimization based on our developed FE model of the ECS-leg system for size fitting.

The details on the three sections of the methodologies are as follows.

(1) FE Modelling of ECS-Leg System

Mechanical properties analysis of the lower limbs and ECS fabrics

Geometric modeling of the lower limbs and ECS fabrics

Meshing construction and boundary condition settings

Validation of the interface pressure induced by ECSs

Mechanical Properties Analysis of the Lower Limbs and ECS Fabrics The ECS fabrics are commonly assumed as an orthotropic lamina, thus, the mechanical properties including Young's modulus, Poisson's ratio, and shear modulus in a 3D scale were determined based on Hooke's Law via Instron and KES system measurement in this study. Among them, the uniaxial tension testing by using Instron system was applied to determine the Young's modulus and Poisson's ratio, and the shear testing and bending testing by using KES system was applied to determine the shear modulus in a 3D scale. The lower limb is assumed as homogeneous, isotropic, incompressible hyperelastic material, which was governed by the Neo-Hookean model and measured based on shear wave elastography testing.

Geometric Modeling of the Lower Limbs and ECS Fabrics In the ECS-leg modeling, the FE leg models were built based on lower limbs of different subjects aged 40-60 year old, while the FE ECS models were designed based on the realistic leg morphologies of these subjects. The detailed procedures and methods to obtain the geometric structures, material properties, and boundary conditions of the numerical modelling were systematically described in this thesis study. Based on the FE simulation results, the parameter optimization to determine ECS fitting for specific users were presented.

The geometry models of the ECS samples were constructed based on the actual tailor-made ECS tubular dimension by using Ansys workbench design modeler (Computer Aided Design (CAD) system). The 3D geometric model of the lower limbs was reconstructed using Mimics software (v20.0, Materialise, Hungary) based on the extracted multiple cross-sectional magnetic resonance imaging (MRI) slices of the lower limbs in the masks. The biocomponents (skin, soft tissue, and bones) were segmented through the custom thresholds' settings and were reconstructed to form a 3D leg geometric model, which would be further imported to the 3-matic software (v20.0, Materialise, Hungary) and Ansys workbench space claim (v19.2, ANSYS, Pennsylvania, Pittsburgh, USA) to eliminate the stitch, gap, and missing faces, and repair gaps between faces to obtain an optimized 3D leg geometric model for finite element (FE) analysis.

Meshing Construction and Boundary Conditions The constructed 3D lower limb tissue models and ECS shell models were meshed by using tetrahedrons elements and hexahedron elements, respectively. The tetrahedron elements were a volume with four faces and were analogous to a triangle in two dimensions. The tibia and fibula bones were fixed in the FE leg model while FE ECS tubular can freely move longitudinally along the lower limb from the ankle to the knee with a specific displacement loading in accordance with wearing practice.

Validation of the Interface Pressure Induced by ECSs

The simulated pressure value would be validated by using a flexible pressure sensing system via the deviation ratios (DRO) analysis (DRO = (simulated results - measured results)/measured results). Simulation algorithms that combined the FE and multi-body techniques (several flexible or rigid bodies interact each other in one system, e.g., ECS-leg system), in a framework of continuum mechanics, were developed with an aid of Ansys Workbench system (v19.2, ANSYS, Pennsylvania, Pittsburgh, USA). The developmental procedure of the 3D FE model involved pre-processing, simulation, and post-processing steps. The pre-processing step determined the geometric models, constitutive relationships, boundary conditions, and meshing constrictions of the ECS-leg system. The post-processing steps was to analyze the simulation results by programming and comparing the simulated data with the experimental results.

(2) Fluid-Solid Interaction (FSI) Modelling of ECS-Leg System

Geometric modeling of the venous flow

Mechanical properties of the venous flow

Meshing Construction and Boundary Condition Settings and validation

Geometric Modelling of Venous Flow The geometry of peroneal vein, small saphenous vein, and great saphenous vein of the lower limb was reconstructed from the axial images via MRI scanning. The venous cross section was assumed as a regular circle considering the real venous morphologies and the fewer pixels induced irregular venous surface. The spatial position of veins was based on MRI images. The reconstruction regular venous cross sections were further reconstructed into a 3D venous model by using Ansys workbench Design modeler.

Mechanical Properties of the Venous Flow

Considering the mechanical properties of the venous flow are similar based on previous studies among different human groups, thus, the venous density and viscosity coefficient were referred to the published data, where the blood flow density is approximate 1060 kg/m^3 (Moser, et al 1988), and the viscosity coefficient of the blood flow is nearly 0.003 Pa•s (Sun, et al. 2020).

Meshing Construction and Boundary Condition Settings and Validation The venous models were meshed using the linear fluent tetrahedron elements with the boundary layer. When the fluid is exercised under the conditions of the Greater Renault, the viscosity and thermal conductivity of the fluid can be regarded as concentrated on the thin layer of the fluid surface, that is, the boundary layer. According to the characteristics of the boundary layer, simplified the Navier-Stokes equation and solved it to obtain the resistance and heat transfer law. Dynamic mesh was applied in the FSI model at the fluid-solid interaction boundary through smoothing, layering and remeshing methods.

The lower and higher external pressures applied by the Class-I-ECS and Class-III-ECS on the skin surface were applied, respectively. The solid-fluid interface was defined as the venous flow, which indicated the boundary between the soft tissue and veins. The velocity inlet (v_{inlet}) was determined based on Doppler ultrasound test via User-Defined Function (c language) and the pressure outlet (P_{outlet}) was set as free flow (0 m/s), respectively. The simulated venous velocity was validated by using the Doppler ultrasound testing via DRO analysis.

(3) Parameter Optimization of the ECSs

Sensitivity analysis in the ECS-leg system

Optimization of material and pressure properties for improving ECS fitting

Sensitivity Parameters Analysis in the ECS-Leg System To determine the design parameters that most sensitively influence the pressure magnitudes in the ECS-leg system, an analytical model was built to construct the relationship among the interface pressure, mechanical properties, and lower limb geometries. Based on our constructed the analytical model, a Sobol sensitive algorithm was applied to calculate the sensitive indexes from the mechanical properties and the geometry properties. The determined sensitive parameters were input to the optimization system for analysis of design sensitive parameters to fit the target pressure level.

Optimization of Material and Pressure Properties for Improving ECS Fitting Based on the developed FE simulation methods in Chapter 3 and Chapter 5 and the sensitivity analysis results, a parameter optimization model was further developed by using Ansys Workbench parameter set module to determine an ECS fitting matrix for the most critical segments of the lower limbs (the ankle and the calf). The purpose was to propose an operable solution to applying ECSs products with appropriate physical-mechanical properties to correspondingly fit the different individual users' bodies, so as to realize the expected or prescribed pressure levels in treatment via a response surface analysis method. The studied design parameters mainly included: (i) the determined pressure ranges and gradients based on the RAL-GZ 387/1 standard, (ii) the determined Young's modulus ranges of the ECS fabrics based on our tested data, and (iii) the leg circumference ranges based on our developed wooden leg system, especially for Asian leg sizes. All these design parameters were analyzed by using an Ansys Workbench parameter set to develop their quantitative relationships and to establish the ECS fitting matrix for guiding product applications in end uses.

1.4 Thesis Outline

In general, this thesis study included nine Chapters. Chapter 1 introduced the research background, existing problems, research objectives, significance, and research methodology with a research flow display. The methodology of the FE model of ECS-leg system were presented. The geometric models, material mechanical properties, and boundary conditions prescribed were described in detail. The geometry models of several human legs were reconstructed based on MRI imaging by using reverse engineering, and the geometry models of the ECS fabrics were constructed by using CAD system based on the morphologies of our developed ECS samples. The mechanical properties of the ECS fabrics were determined by the integrated instrumental experiments and theory calculations.

Following this introductory chapter, Chapter 2 conducted an extensive literature review from different aspects, including an introduction of the design, function, and classification of the ECS fabrics and products, and the existing studies on compression therapies by using compression textiles and garments. It also presented various assessment techniques to explore working mechanisms and performances of ECS. The FE analysis and FSI simulation of the ECS materials were introduced. Finally, the interactions between the ECSs and the applied bodies (lower limbs) were reviewed and discussed.

In Chapter 3, a novel analytical modelling of design material properties was constructed based on Hooke's Law and Airy's stress function. The testing methods of the ECS fabrics were described. The developed elastic modulus methods of the ECS fabrics were applied in Chapter 5 to determine our designed ECS fabrics mechanical properties.

In Chapter 4, the geometry models of the human legs and ECS fabrics were reconstructed. The constructed geometric models were future input into FE modelling for numerical simulation. The reconstructed 3D legs and ECS geometric models were input into FE modelling to numerically simulate the mechanical behaviors of the lower limbs exerted by the different ECS fabrics.

In Chapter 5, FE modeling was employed to predict the biomechanical performance of the ECS-leg system. The interface pressure between the ECSs and soft tissues, the tissue stress transmission within the soft tissues, and the tissue deformation were numerically simulated. The predicted interface pressures were validated by using the pressure sensing system. The average simulated interface pressures were input to the FSI model in Chapter 6 to determine the venous hemodynamics responses.

To further analyze stress transmission effects on the venous system, in Chapter 6, the FSI modelling was developed to predict the venous velocities caused by the studied

ECS fabrics. The geometry modelling was determined based on Chapter 4 and the pressure values on the leg surface were set as the average interface pressure simulated in Chapter 5. The predicted venous velocities by applying FSI modelling were validated by using the Doppler ultrasound testing system. The simulated venous velocities in the ECS-leg system reflected the venous flow conditions affected by the ECS fabrics, which provided a reference facilitating the understanding of compression therapeutic effect of ECSs on the venous disorders treatment.

To balance and optimize pressure function and wearing comfort of ECSs in uses, Chapters 7 and 8 conducted the comfort assessment by applying the subjective questionnaires. Optimization of design parameters of the ECS-leg system was conducted based on our developed simulation methods and quantified results.

In Chapter 9, the summary and conclusions of this thesis study were given. Further research plan on elastic compression for compression therapy were discussed from the aspects of constructing the FE ECS-leg model by using different ECS structural design; constructing the optimized Laplace's Law to improve the accuracy of the interface pressure prediction; and predicting the venous pressure and wall shear stress by developed FSI modelling to further reflect hemodynamic responses in the ECS-leg system.

A flow chart to generally display this thesis study is shown in Figure 1.1.

Figure 1.1 A flow chart of the thesis study.

CHAPTER 2 LITERATURE REVIEW

2.1 Design, Function, and Structures of Elastic Compression Stockings (ECSs)

Textile technology plays a critical role in constructing functional compression materials to achieve the expected efficacy in modern compression therapy (Liu, et al. 2016). Various compression textiles have been applied for venous disorders treatment, including compression stockings, compression bandages, leggings, and orthosis (Li, et al. 2006). Among them, ECS as a typical kind of compression textiles that can provide a controllable external pressure for treating the specific venous symptoms. The venous flow velocity could be promoted by the external pressure exerted on the skin and tissues based on the continuity equation (Spurk, et al. 2020). However, the mechanism of action of ECSs in compression therapy remains unclear, which resulted from several aspects, (i) the mechanical properties of the ECS fabrics in a 3D scale are rarely to determine, (ii) the soft tissues exerted by the ECS generated a large deformation, (iii) the determination of anatomic structures and mechanical properties of muscle components are challenging, and (iv) the venous hemodynamics effected by the ECSs relate to a complex fluid-solid interaction problem.

The venous system of the lower limb includes the superficial and deep veins (Fig. 2.1), which are defined by their respective relationships to the muscular fascia (Liu, et al. 2016) (Fig. 2.2). Superficial veins are located between the skin and the muscular fascia, whereas the deep veins are accompanied by the arteries encompassed by muscular fascia. Blood hydrostatic pressure, the compressive force generated by leg and foot muscles, competence of valves, and respiration are the principal forces affecting venous return. Venous insufficiency is a condition in which the veins have problems sending blood from the legs back to the heart. CVI is a long-term progressive condition, which is most commonly caused by the incompetent valves in the venous system. If superficial or perforating venous valves become incompetent, blood can flow back from deep veins into the superficial veins, resulting in increased intra-luminal pressure, causing various veins even deep venous thrombosis. It has been estimated that approximately 5 million people have CVI in the United States (Rhode, et al. 1998), and around 100 million people suffer from venous disorders in lower extremities in China (Wang, et al. 2007).

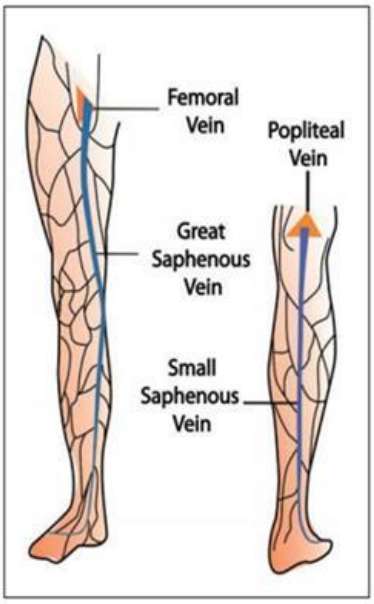

Effectivenss of ECSs
• Increased venous flow velocity
• Improved venous return
• Decreased venous blood volume
• Reduced reflux in diseased superficial and/or deep veins
• Reduced diameters of deep calf veins in standing position
• Increased muscle efficiency and beneficial in reducing muscle fatigue
• Improved healing of venous ulcers
• Reduced rates of re-ulceration of venous ulcers
• Improved pain, swelling, activity tolerance and wellbeing

Figure 2.1 Venous system of the lower extremity and the effectiveness of ECSs (Liu, et al. 2016).

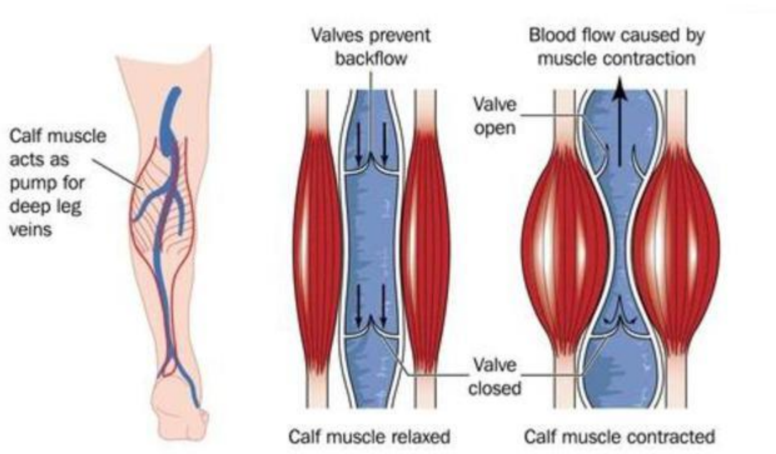

Figure 2.2 Interaction between the veins and the muscular fascia (Liu, et al. 2018).

The ECS fabrics are commonly fabricated by the laid-in knitted structures that is composed by the intermeshing loops of yarns (Fig. 2.3). Their material properties, knitting structures, and fabrication technologies directly affect the physical-mechanical behaviors of the compression textiles as well as their pressure performances in CVI treatment. Circular and flat knitting technologies are the major approaches to fabricate custom-made and ready-to-wear ECSs (Liu, et al. 2016). Both of them have their merits in the fabrication flexibility, production efficiency and wearing perceptions.

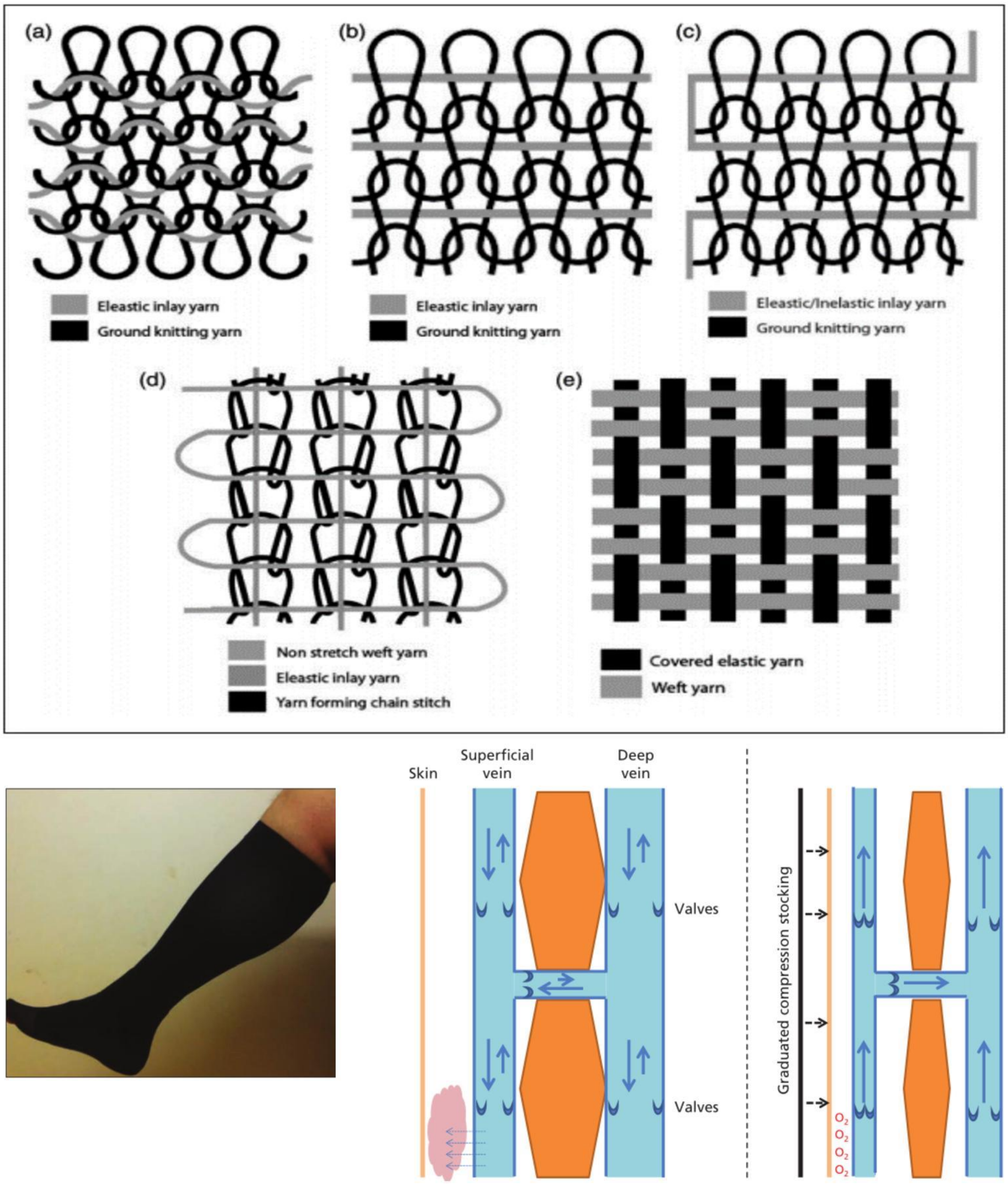

Figure 2.3 Laid-in stitch structures of the functional fabrics and the appearance and functions of the ECS fabrics (Liu, et al. 2016; Gopalakrishnan, et al. 2018; Lim, et al. 2014).

The application of ECSs has been demonstrated to be effective in enhancing venous return and reducing venous stasis. Based on the pressure magnitudes and symptoms to be treated, the ECSs are commonly classified into the four levels based on the pressure dosages exerted at the ankle (Liu, et al. 2016) (Table 2.1). Class-I-ECS provides the lower pressure level (15-20 mmHg) for the relief of the leg fatigue, tiredness, and heaviness. Correspondingly, Class-II and Class-III ECSs provide a moderate pressure dosage, which range from approximate 20-40 mmHg, respectively, for the prevention or treatment of CVI or the reduction of postoperative pain in the primary varicose treatment (Elderman, et al. 2014). Class-IV-ECS provides the higher-pressure level (>40 mmHg) (Rohan, et al. 2015), which are widely applied in relieving CVI symptoms or treating more serious symptoms such as lymphatic edema (Jungbeck, et al. 1997). The selection of the ECS depends on the lower limb size of the users, pressure tolerance, and symptom severities.

The ECS modalities also can be classified into three main styles: full-length, thigh-length, and knee-length. Compared with the full-length, thigh-length ECS and knee-length ECS are easier to be worn and are more comfortable in use. There are no significant differences in the increase of deep venous flow velocity among the three types (Porteous, et al. 1989). Relatively, the knee-length ECS have higher comfort scores and cost-effectiveness than that of using the thigh-length or full-length ECS in the venous treatment based on the clinical investigation (Williams, et al. 1994).

Table 2.1 The classification system of the ECSs.

Class	Description	Classification system of ECS pressure (mmHg)				
		DE	FR	UK	EU	USA
I	Light	18-21	10-15	14-17	15-21	15-20
II	Medium	23-32	15-20	18-24	23-32	23-30
III	Strong	34-46	20-36	25-35	34-46	30-40
IV	Very Strong	>49	>36	N/A	>49	N/A

DE: Germany [RAL-GZ387]; FR: France [ASQUAL]; UK: British [BS:6612]; USA: America; EU: Europe [ENV12718].

2.2 Assessment Techniques of ECSs Performances

To analyze the functional performances of the ECSs in the ECS-leg system, the interface pressures are the critical indicators to reflect ECS biomechanical effects in compression therapy. The interface pressure levels can be assessed based on the direct measurement methods and indirect prediction or simulation methods.

Sensor measurement has been commonly applied to determine the ECSs performances through directly detecting the interface pressure between the lower limb and the ECSs. By the insertion of a pressure sensor in the form of a fluid (detecting the fluid position by electric signal to measure fluid pressure), piezoresistance (changing the electrical resistance of the sensor material to measure the interface pressure), or air-filled balloon (changing the air volume in the balloon to measure the interface pressure) (e.g., Picopress system, Tally system, and Kikuhime system, etc) (Fig. 2.4) between the fabric/garment layer and the applied body surfaces, the interface pressure can be recorded (Momota, et al. 1993; Harries, et al. 1989; Flaud, et al. 2010). Flaud et al. compared the measured interface pressures tested by using both Tally system and Kikuhime system and assessed the errors of these two systems. The Tally system required to test pressure values at the exact time with the electrical contact, it produced the lower systematic error in the leg model testing (errors= ± 3.2 mmHg at the calf, while the Kikuhime system required to test the pressure values in a real time, it produced a higher pressure error (±14.8 mmHg at the calf) (Flaud, et al. 2010). The advantage of the Picopress system was that the measured pressure values at the leg profile was relatively accurate (errors = ±3.0 mmHg) (Khaburi, et al. 2011; Lao, et al. 2019). Considering the precision of the pressure measurement on the leg, Picopress system was applied to measure the interface pressure in the ECS-leg system in this thesis to validate the simulated interface pressures by our developed FE model.

In addition, 3D FE models, as an indirect assessment technology, have been applied as numerical simulation method to investigate pressure performances exerted by ECSs (Dubuis, et al. 2013; Rohan, et al. 2013), which not only visualized the interface pressure between the lower limb and the ECS, but also reflected the tissue deformation and stress transmission in the deeper tissues exerted by the elastic compression.

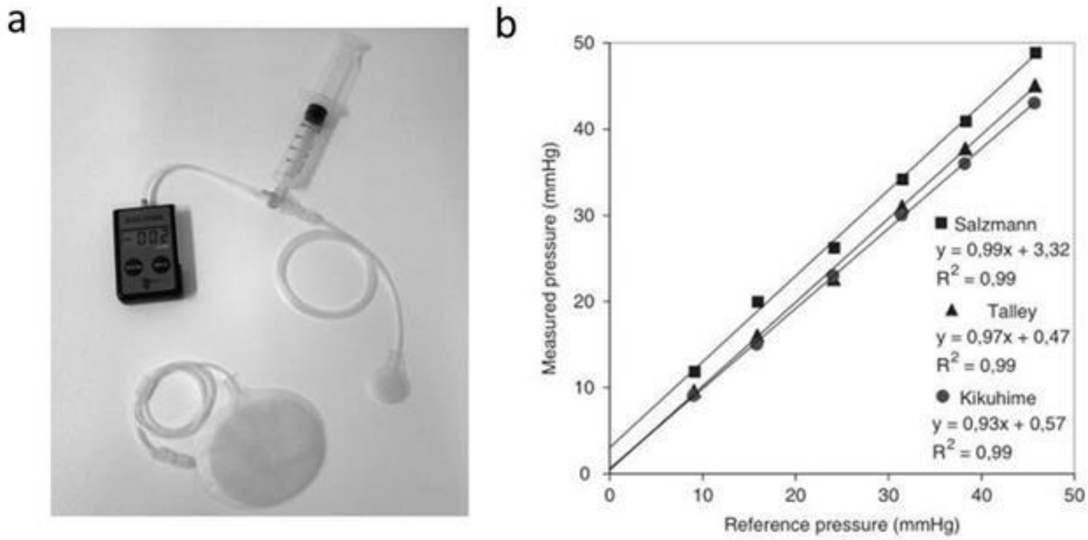

Figure 2.4 (a) Pressure measurement system; and (b) the measured pressure results (Flaud, et al. 2010).

The interactions between the lower limb and the ECS are significantly influenced by the material mechanical properties (Ye, et al. 2020). The assessment techniques of the ECS performances also included various objective or instrumental material testing and physical-mechanical analysis. For example, elastic moduli are most critical parameter to control tension, shear, compression, bending, and recovery properties of the compression textiles (Silva, et al. 2014; Liu, et al. 2006), mainly including Young's modulus, Poisson's ratio, and shear modulus, which describe the relationships between the stresses and the strains of the elastic solids (materials). For the ECSs, the Young's modulus is commonly applied to assess the tension stiffness undergoing extension or compression deformation in one direction (Silva, et al. 2014), which describes the linear relationship between normal stress and normal strain in the elastic deformation and was defined as the ratio of normal stress to normal strain. The elastic deformation indicates that the deformation properties satisfy the Hooke's Law, and the elastic material can return to its original shape after the extension or compression loading is removed (Beer, et al. 2020). Poisson's ratio is a measure of Poisson's effect, which indicates that the elastic material tends to contract in the direction perpendicular to the direction of tension. The value of Poisson's ratio is a negative ratio of the transverse strain to the longitudinal strain (Silva, et al. 2014; Gercek, et al. 2007). Shear modulus is used to assess the shear stiffness undergoing the shear deformation (an opposing force acted on its opposite surface), which describes the linear relationship between the shear stress and the shear strain in the elastic deformation and is defined as the ratio of shear stress to the shear strain (Silva, et al. 2014; McNaught, et al. 1997).

To determine the mechanical properties of elastic compression fabrics, experimental tests integrated with the orthotropic stiffness matrix based on the Hooke's Law have been applied. Hooke's Law provides the basic theories to determine the relationship between the force, deformation, and mechanical properties, and the force and deformation magnitude can be measured by experimental test.

Kawabata evaluation system (KES) and Instron testing systems have been applied to build correlation between materials mechanical properties and digital images. KES system is an advanced testing solution to determine fabric mechanical properties (tension, compression, and shear) (Carr, et al. 1988). Instron is an apparatus to especially measure tension properties of materials (Turl, et al, 1956). Based on Hooke's Law, Ruan et al. also proposed an analytical model based on the orthotropic Hooke's Law to predict elastic behavior of knitted-fabric composites (Ruan, et al. 1996). Ramakrishna et al. also developed an analytical model of the plain knitted reinforced composites with integration of yarns' geometric studies based on Hooke's Law as well as the rules of mixture (Ramakrishna, et al. 1997). Thus, the relationship among the deformation, force, and mechanical properties in a 2D scale has been established. By using previous study proposed model, Hu et al. determined the tensile moduli of the knitted fabric in multiple directions combined with Instron 4466 experimental (Hu, et al. 1998). Furthermore, Zhou et al. combined the analytical model with the strip biaxial tensile test by using the KES system to predict the Young's moduli and Poisson's ratios for elastic knitted fabrics (Zhou, et al. 2010) (Fig. 2.5). Recently, Liu et al. applied the KES and Instron systems to determine the KEFs' elastic moduli systematically (Liu, et al. 2006). The results of the elastic moduli provide the essential mechanical parameters for the related numerical simulation of the ECS fabrics to determine the pressure level in the FE ECS-leg system.

These methods can be also applied in the woven fabrics, for example, Hursa et al. presented a digital image correlation method to determine the Poisson's ratio of the woven fabric according to the displacement and deformations in the *x* and *y* axis directions in a uniaxial tensile test (Hursa, et al. 2009) (Fig. 2.5). Sun et al. proposed a mechanical model for the woven fabric to predict fabric Poisson's ratio based on Hooke's Law (Sun, et al. 2005).

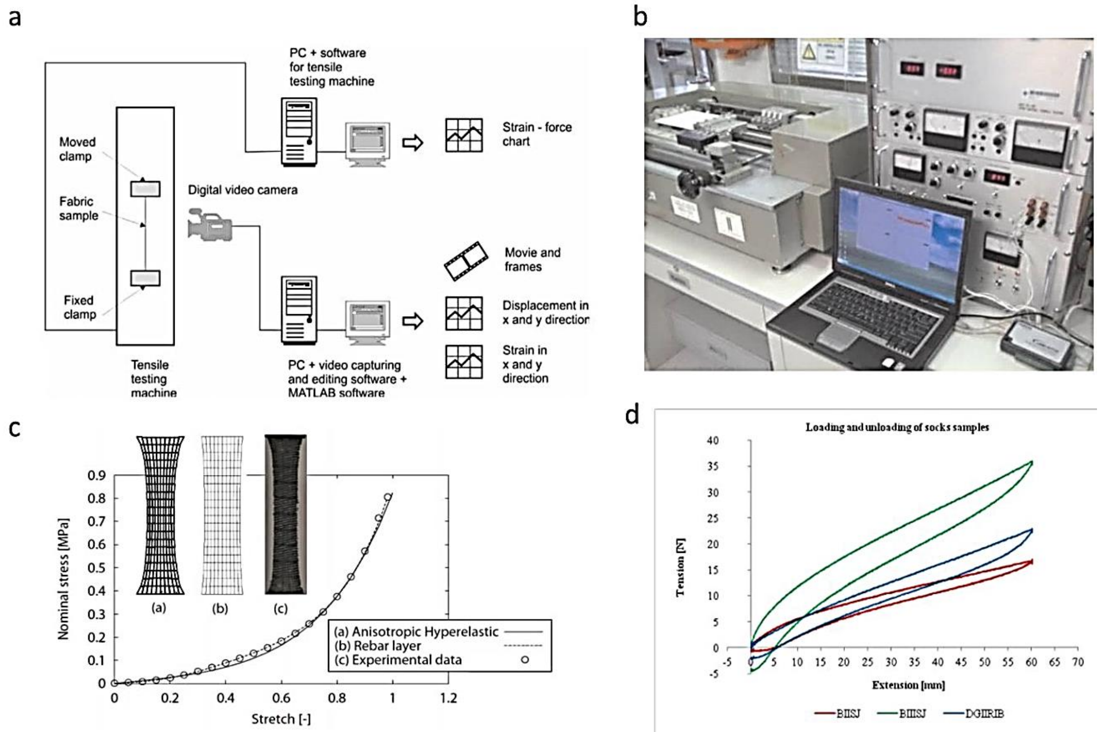

Figure 2.5 (a) Experimental scheme of Poisson's ratio measurement (Hursa, et al. 2009); (b) experimental system of the biaxial tension test for Young's modulus measurement (Zhou, et al. 2010); the stress-strain curves recorded by Instron system; (c) stress-stretch curves of the uniaxial tension; (d) tension-extension curves of the uniaxial tension.

In general, combining the analytical models with Instron and FES system is a common method to determine the mechanical properties of the ECS fabrics in the current studies. However, the existed 2D analytical models are complex and cannot reflect the mechanical performances of the ECS fabrics along thickness direction and the effects of fabric properties along their course, wale, and thickness directions on the pressure performances holistically. Therefore, a new 2D analytical model based on the Hooke's Law combined with Instron and FES systems were developed to determine the mechanical properties of the ECS fabrics in Chapter 3. In summary, the mechanical properties in a 2D scale ignored their mechanical properties across the fabric thickness, which directly contribute to the normal pressure in practical applications. And, to further analyze the effects of ECS fabrics on pressure performances in a three-dimensional scale, a new 3D analytical model based on the Hooke's Law by using Airy's stress function combined with Instron and FES systems were further constructed to improve the simulation precision of the FE ECS-leg model in the Chapter 3 of this thesis work.

2.3 Finite Element Analysis of the ECS-Leg System

The venous hemodynamics of patients with venous disorders are different with that of the health human (Lattimer, et al. 2016). The lower limb's venous hemodynamics is dependent on the interface pressure as well as the material properties of the ECS (Ye, et al. 2020). Finite element method (FEM) has been applied to analyze the interaction mechanisms between textile shell and body tissues (Liang, et al. 2019), which are a numerical method to solve the partial differential equations (Liu, et al. 2013; Hsu, et al. 2012; Hutton, et al. 2004) (Fig. 2.6). FEM are developed on the basis of variation principle, which is widely used in analysis of the mechanical performance of a solid material (e.g., stress, strain and deformation) (Hsu, et al. 2012) through subdividing a large problem into smaller, simpler parts that are called finite elements. The simple equations that model these finite elements are then assembled into a larger system of equations that models the entire problem.

FEM uses variation methods from the calculus of variations to approximate a solution by minimizing an associated error function. FEM was initially proposed by Hrennikoff and Courant in the early 1940s (Hrennikoff, et al. 1994; Courant, et al. 1943). This method is based on the variation principle, which meshes the discretization of a continuous domain into a set of discrete sub-domains called ‘element’. FEM was further developed in the 1960s and 1970s (Hinton, et al. 1968). In recent years, the appearance of the advanced FEM software (Ansys, Abques and Comsol) promoted the FEM development, which has been generalized for the numerical modeling of the physical systems in a wide variety of engineering disciplines, e.g., electromagnetism, heat transfer, fluid dynamics, and solid mechanics (Ye, et al. 2019; Gandzha, et al. 2019; Wang, et al. 2019) (Fig.2.6).

In the studies of human-compression garments system, the FEM has been used as a numerical simulation method to evaluate interface pressure between the soft tissues and various compression textiles, as well as stress transmission from the skin to the bones and veins. Liu et al. applied FEM to predict the dynamic pressure functional performances on the whole leg of ECSs (Liu, et al. 2006), that is, the pressure and stress variations with application time. Dai et al. predicted and visualized the skin pressure and stress profiles on the lower leg applied by ECSs using FEM (Dai, et al.

2007). Takaya et al. predicted the interface pressure and stress profile of the vest via FEM (Takaya, et al. 2012). Hedigalla et al. also applied FEM to numerically simulate the interface pressure between the sleeve and soft tissues (Hedigalla, et al. 2022) (Fig 2.6).

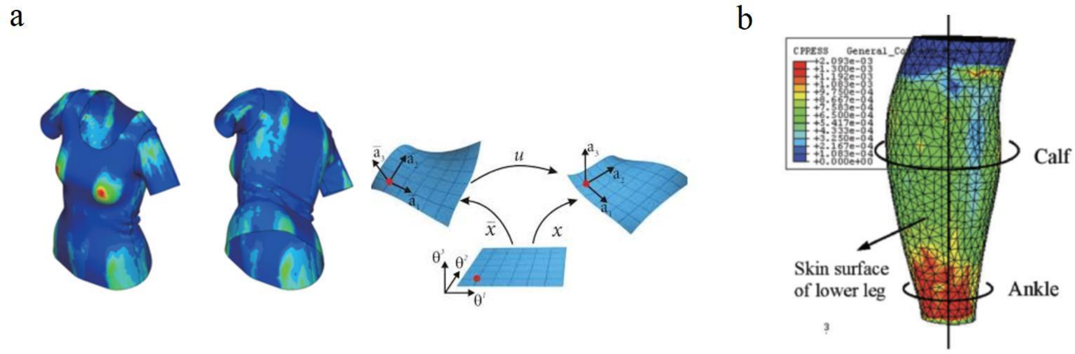

Figure 2.6 Interface pressure and stress profiles of the vest (Takaya, et al. 2012), and (b) the ECS (Dai, et al. 2007).

FEM is based on the minimum total potential energy principle (Hsu, et al. 2012) to determine the relationship among the stress distribution, strain distribution, displace, and external loading in each element. In general, the FEM construction can be divided into five steps, i.e., (i) discretizing the research objective (Fig. 2.7); (ii) determining the shape function of each element; (iii) determining the relationship between the strain and deformation (strain matrix); (iv) determining the relationship between the stress and strain (stress matrix); and (v) determining the relationship between the stress and deformation (stiffness matrix). The stiffness matrix can be expressed as follow:

$$\int B^T DBtdxdy = K^e \tag{2.1}$$

where D and C are the stress matrix and strain matrix, respectively, and K^e is the local stiffness matrix (stiffness matrix for each element).

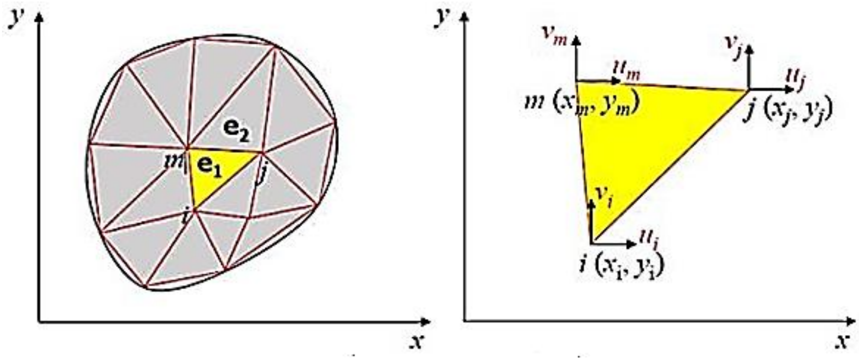

Figure 2.7 The diagram of finite element method for discretization of the triangle element.

Based on the relationship between the stress and deformation of elastic solid bodies, various FEM software have been applied to analyze the mechanical performances of elastic materials. The pre-process using the software can be divided into two steps, i.e., material properties' definition and geometry modeling. The materials properties such as Young's modulus and Poisson's ratios can be determined by performing tension test, which has been discussed in Chapter 2.2. The geometry model of the studied object can be constructed by CAD system (e.g., Auto CAD, Catia, Design modeler, Solidworks and Spaceclaim). In previous study, Liu et al. applied CAD system in the FE Package ABAQUS to establish the geometric models of ECSs including four portions (ankle, calf, knee, and thigh) based on the magnetic resonance imaging (MRI) of the actual leg dimensions (Liu, et al. 2006). The MR images built based on reverse engineering method offer abundant informative data from the living subjects for musculoskeletal modeling. Blemker et al. constructed the muscle and bone surfaces from multiple series of MR images. Surface models of the bones and muscles were generated from 2D outlines that were defined manually in the images (Blemker, et al. 2007).

Carbone et al. presented a new comprehensive musculoskeletal geometry dataset of the lower extremity based on the medical images and dissection measurements of a single cadaver specimen (Fig. 2.8) (Carbone, et al. 2015). Rohan et al. constructed the 2D leg geometry model based on the MRI integrated with echography to determine the cross-section area (Rohan, et al. 2013). Manafi-Khanian et al. further applied the reverse engineering approach to reconstruct the 3D leg geometry model based on MRI slices for the numerical analysis (Manafi-Khanian, et al 2016).

Commonly, the geometry modelling of the lower limb can be reconstructed by using reverse engineering technology based on the MR imaging. However, few studies considered the pressure magnitudes effected by the muscle segments in the FE leg-ECS system, that is, the existed studies mainly considered the lower limb as an overall soft tissue. Therefore, in the Chapter 4 and Chapter 5, the FE ECS-leg geometry model with muscle segments would be constructed based on MR imaging for analysis of the working mechanisms of the ECS fabrics and their effects on the soft tissues.

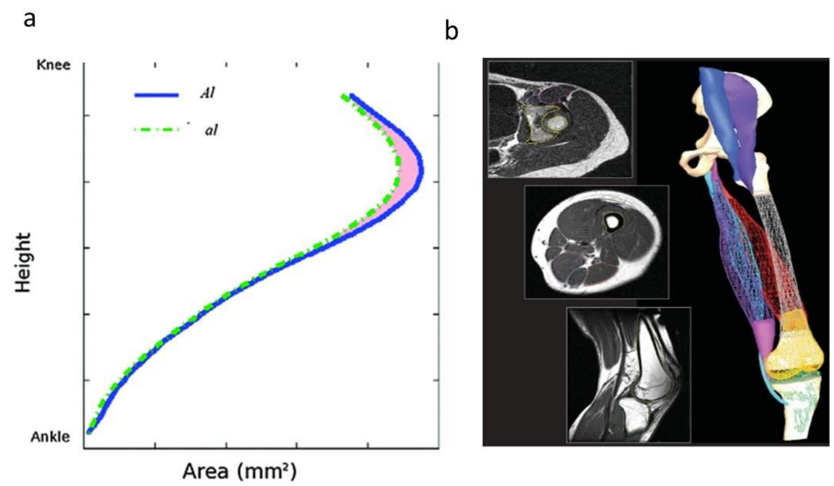

Figure 2.8 (a) Contour variety with and without pressure; (b) reconstruction of muscle and bone surfaces from multiple medical images (Blemker, et al. 2007).

After the geometry model and mechanical is input into the FE model, the developed FE model can be discretized to form meshing structures with different shapes (e.g., tetrahedron and hexahedron) and the amounts of elements. The accuracy and simulation time of the FE modeling are largely determined by the number of meshing elements, element types, and contact settings. The setting of the contact condition is to determine the interactive properties between the two bodies (e.g., limb and garment), including interface pressure, tissue stress, skin deformation, and frictional forces. In general, there are five main types of contact conditions, i.e., bonded, no separation, frictionless, rough and fictional (Raous, et al. 1995), which are dependent on the solid mechanics' theories (Hosford, et al. 2010). The boundary conditions set in the FE modeling is to analyze the effects of the applied materials on the studied object, e.g., force, pressure, or moment loading (Hsu, et al. 2012).

The existed studies showed that the FEM can be applied to visualize the pressure profile between compression garments and soft tissues. However, few studies conducted the internal mechanical behaviors of the soft tissues effected by the ECS fabrics. To address this issue, the stress transmission within the lower limb tissues would be simulated and analyzed in Chapter 5. Moreover, few studies detected the tissue interface pressure difference exerted by the ECS fabrics among multi-subjects via FE methods. Thus, three subject-specific FE ECS-leg models would be constructed to simulate the pressure magnitudes induced by ECS materials.

2.4 Fluid Dynamics Analysis of ECS Effects on Lower Limb

The venous flow hemodynamics and morphologies were changed when the human suffer from CVI (deep veins thrombosis, varicose discords, and lymphedema) (Smith, et al. 1991; Rabe, et al. 2012; Lattimer, et al. 2016). Computational fluid dynamics (CFD) have been applied to simulate, analyze, and evaluate the venous hemodynamic properties (Amans, et al. 2018), which is a branch of fluid mechanics that uses numerical analysis and data structures to analyze and solve problems that involve fluid flows. CFD has a wide range of applications in biomedicine, meteorology, and aerospace (Chandra, et al. 2021; Colognesi, et al. 2021; Zhao, et al. 2021), such as the determination of the blood flow velocity under the pulse for predicting the weather patterns (Chandra, et al. 2021), the computation of the mass flow rate of the oil through pipe for predicting the oil transportation volumes (Colognesi, et al. 2021), and the calculation of the force and the moment of the airplane for optimizing the airplane structural design (Zhao, et al. 2021).

The solution of CFD includes the computation of flow velocity, pressure, and wall shear stress based on the Navier-Stokes equations using finite volume method (Ma, et al. 2019; Muhammad, et al. 2020; Wang, et al. 2013) (Fig. 2.9). The fluid properties such as fluid density and viscosity coefficient, are commonly determined by using the published data, e.g., the water density is approximate 1000 kg/m^3, and the viscosity coefficient of water is approximately 0.001 Pa • s (Kumar, et al. 2020); correspondingly, the blood flow density is approximate 1060 kg/m^3 (Moser, et al. 1998), and the viscosity coefficient of the blood flow is nearly 0.003 Pa•s (Sun, et al.

2020).

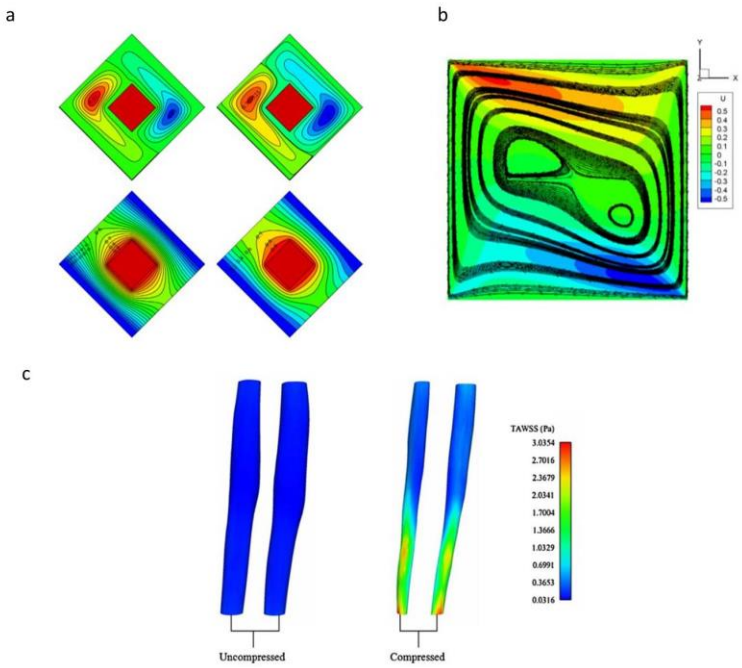

Figure 2.9 Flow hemodynamics simulated by CFD; (a) the simulated flow velocity of a nano-fluid in an inclined square (Ma, et al. 2019); (b) simulated flow velocity of $C_2H_6O_2$-Ag nano-fluid along horizontal heater (Muhammad, et al. 2020); and (c) simulated wall shear stress of peroneal veins under external pressure (Wang, et al.2013).

The fluent meshing (e.g., tetrahedron and hexahedron) are applied in the geometry model to compute the fluid mechanic behaviors. The boundary conditions of the fluid mechanic properties can be divided into inlet, outlet, and wall properties. Velocity inlet as the boundary condition is usually used to simulate incompressible fluid mechanical properties (Altuntop, et al. 2006). Mass flow inlet is used to simulate the compressible fluid where the mass flow inlet distribution is known.

For the outlet boundary conditions, the pressure outlet is usually applied in the fluent system for subsonic flow. The pressure outlet is generally set at 0 Pa, which means that the fluid can be regarded as a free outflow. The boundary conditions of the wall are divided into three types, including sliding wall (e.g., cone and plate system) (Fig. 2.10a), moving wall (e.g., the particle–solid interactions and particle–fluid interactions)

(Akbarzadeh, et al. 2016), and stationary wall (e.g., vascular wall) (Swillens, et al. 2010) (Fig. 2.10). All the boundary conditions of the fluid mechanic properties as the aforementioned can be computationally determined based on the demands of the applications.

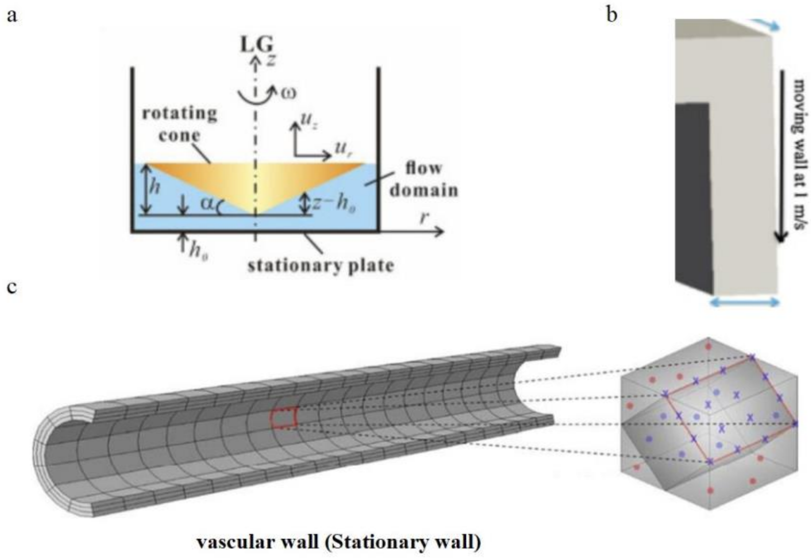

Figure 2.10 (a) Sliding wall boundary condition (Ye, et al. 2019); (b) moving wall boundary condition (Akbarzadeh, et al. 2016); and (c) stationary wall boundary condition (Swillens, et al. 2010).

In the CFD model, the flow patterns mainly include laminar flow and turbulence flow. The flow patterns can be determined by the value of Reynolds's number (Spurk, et al. 2020). If the Reynolds's number is less than 2300, the flow can be assumed as laminar flow. Correspondingly, if the Reynolds's number is more than 2300, the flow can be regarded as turbulence flow, which is influenced by its intensity and hydraulic diameter. The hydraulic diameter of the turbulence flow relates to the shape and size of the pipe (e.g., vessel).

The turbulence intensity can be determined through measuring the strength of the turbulence. The Reynolds-averaged Navier–Stokes equations are time-averaged equations of motion for fluid flow, which are commonly used to predict the fluid dynamic properties of the turbulence flow (Spurk, et al. 2020). The venous flow in the lower limb can be assumed as laminar flow (Li, et al 2019). The hydraulic diameter and turbulence intensity hence would be not considered in the simulation of the leg-ECS system. Amans et al. investigated the sigmoid colon venous flow velocity for patients with sigmoid sinus diverticulum (SSD) based on magnetic resonance (MR) images by using CFD model. The sigmoid colon venous velocity of the patients with SSD was approximately 0.2 m/s (Amans, et al. 2018).

Sigovan et al. applied a non-contrast-enhanced magnetic resonance imaging (MRI) protocol combined with CFD modeling to simulate the shear stresses, venous velocities, and cross sections of the arm's venous walls for the patients with arterio-venous fistula. The arm's venous velocities in the swing segment increased from 0.5 m/s to 1.0 m/s effected by arterio-venous fistula. Similarly, venous wall shear stress at the arm in the swing segment could be also increased from 10 Pa to 20 Pa effected by arterio-venous fistula (Sigovan, et al. 2013). Liu et al. analyzed the blood hemodynamic properties (blood velocity and blood pressure) in cerebral venous sinus with stenosis by using CFD modeling based on MR venography. It was found that the blood pressure and velocity distributions were different with positions caused by gravitational acceleration (Liu, et al. 2018).

The CFD modeling has been applied to quantitatively analyze the venous hemodynamics of the lower limb exerted by ECSs. Smith et al. investigated the effect of graduated compression stockings on the distension of the deep veins of the calf. It can be found that the application of the stockings decreased the calf venous diameters by 20% for the patients with deep vein thrombosis (Smith, et al. 1991) (Fig. 2.11a). Lattimer et al. analyzed the venous hemodynamics varieties (e.g., venous volume and outflow fraction) effected by lymphedema using air-plethysmograph testing (Lattimer, et al. 2016) (Fig. 2.11b). Rohan et al. developed a 2D FEM of the lower leg to study the response of the main deep veins to both elastic compression and muscle contraction. However, these developed 2D models cannot reflect the venous flow hemodynamics in a 3D scale (Rohan, et al. 2015), and few studies constructed 3D FSI (CFD combined with FE) model to detect the venous hemodynamics response effected by the ECS fabrics. Therefore, a new 3D FSI model was built to characterize the venous velocity response by the ECS fabrics in Chapter 6.

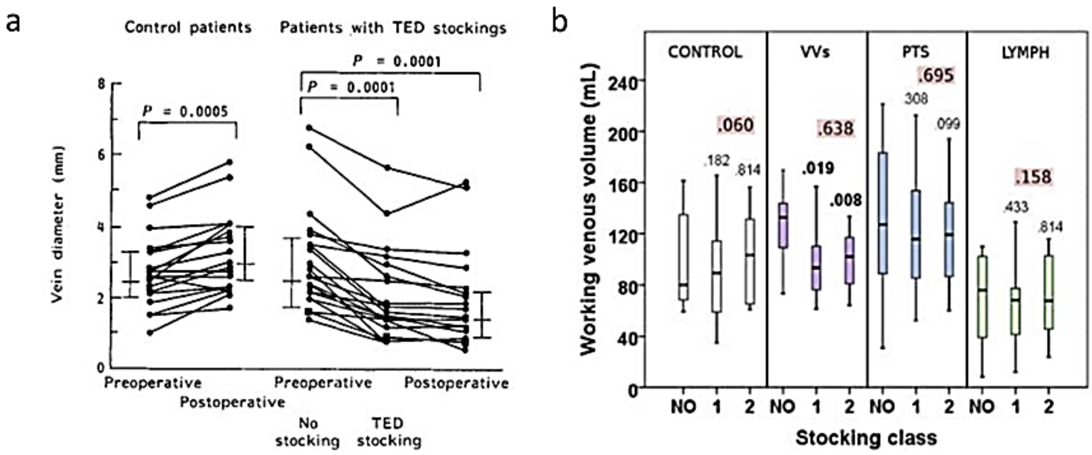

Figure 2.11 (a) Variations in venous diameters exerted by the ECS (Smith, et al. 1991); and (b) variations of the working venous volumes effected by the ECS (Lattimer, et al. 2016).

2.5 Interactive Analysis between the Lower Limbs and ECSs

The interaction between the ECSs and soft tissues mainly includes the interface pressure between the ECS and lower limb, and the stress transmission from the skin to the venous wall exerted by the ECS. Among them, the magnitudes and distributions of the interface pressure applied by ECSs as well as the effects of tissue stress by ECSs on the venous hemodynamics are important to realize precautionary and therapeutic function (Liu, et al. 2006; Lattimer, et al. 2016). To determine the interface pressure between the lower limb and the ECS, three main methods are commonly applied, including using Laplace’s Law and the modified Laplace’s Law to predict interface pressure (approximately by 10-35% errors) based on the measured ECS’s tension and curvature of the lower limb; using pressure sensors to measure the interface pressure directly; and using 3D FEM to numerically simulate the interface pressure.

Cheng et al. predicted the interface pressure between the lower limb and ECSs by applying Laplace’s Law through assuming the lower limb to be a cylinder of the known radius (Cheng, et al. 1984). It can be found that the interface pressure is affected by the ECS’s tension and the curvature of the lower limb. In order to characterize the tension properties of the ECS, the relationship between the tension and tensile strain has been analyzed and constructed (Chen, et al. 2013). Leung et al. proposed a modified Laplace’s Law to predict interface pressure between the compression garments and soft tissues (Leung, et al. 2010). Barhoumi et al. also proposed (Barhoumi, et al. 2020) a modified Laplace’s Law to predict interface pressure and built the quantitative relationship among the stockings’ tension, circumference, applied force, and stress (Fig. 2.12). Compared with Laplace’s law, the modified Laplace’s law showed more details (variations) derived based on the original Laplace’s law, including the relationship of deformation and strain of the ECS materials, leg size, and interface pressure. However, the existing Laplace’s law and the modified laws do not fully reflect the geometric and biomechanical properties of the applied body as well as the variations of body surface curvatures, which may influence the accuracy of the calculated pressure exerted by compression garments.

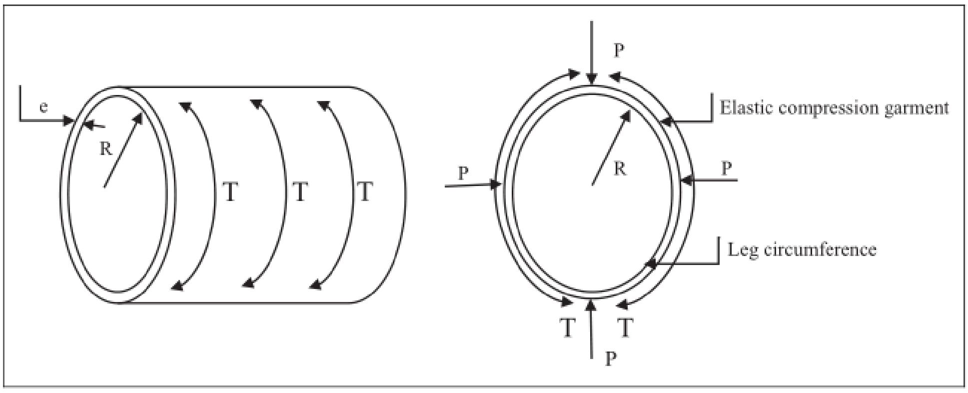

Figure 2.12 An example of interface pressure applied by the ECS on a leg model (Barhoumi, et al. 2020).

The interface pressure exerted by the ECSs can be measured and recorded by inserting a pressure sensor in the form of a fluid or air-filled balloon (Momota, et al. 1993; Harries, et al. 1989) between the ECSs and the applied body. Flaud et al. comparatively evaluated the three measuring pressure sensors (i.e., Salzmann, Talley, and Kikuhime) (Flaud, et al. 2010). It can be found that the three sensors showed an improved accuracy in measuring in situ interface pressure, but some limitations still exist. Eren et al. further optimized the measurement device to measure the interface pressure. For example, they developed Kikuhime device to improve precision (Eren, et al. 2018) through adopting a point-to-point measurement method.

It was noted that the application of both Laplace‘s law and sensor measurement methods in pressure assessment remain exist limitations. For example, the internal mechanical behavior as well as the stress transmission cannot be obtained. Furthermore, the venous hemodynamic response induced by the ECS fabrics cannot be characterized.

To address the above limitations, FE modeling can be used to visualize and predict the interface pressure between the ECS fabrics and lower limb as well as the stress transmission from the skin to the bones and veins. When the two objects contact, the reaction forces oppose the geometrical interpenetration while the friction forces prevent the relative sliding. For the normal contact of 3D bodies, there are two cases for the contact condition (Li, et al. 2006), i.e., non-penetration and a small penetration allowed. The penetration equation between the two bodies can be expressed as

$$\begin{aligned} g_N &= (x^2 - x^1)*n^1;\ if\,(x^2 - x^1)*n^1 < 0; \\ g_N &= 0; Otherwise \end{aligned} \tag{2.2}$$

At the contact boundary, the point x^1 in b^1 comes in contact with the point x^2 in b^2 , and n^1 denotes the normal of the contact surface at point x^1 (Fig. 2.13).

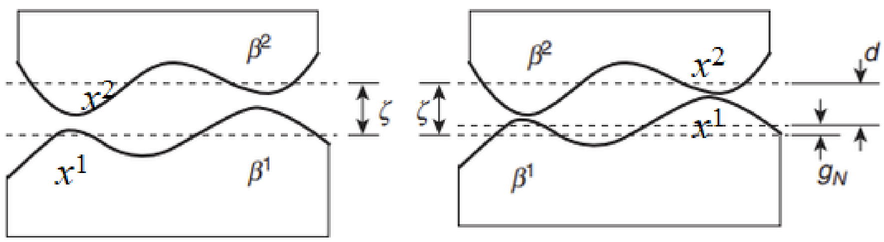

Figure 2.13 Physical contact of the two bodies (Li, et al. 2006).

Based on the contact analysis, Liu et al. further analyzed the interface pressure magnitudes and distributions in the longitudinal directions and the dynamic mechanical interactions between human leg-stocking during wear by using 3D FEM (Liu, et al. 2006). Dan et al. also built the 3D FEM to predict the relationship between the pressure and displacement at the top part of a man's sock (Dan, et al. 2011). The pressure-displacement curves fitted to the quadratic equations. Rohan et al. investigated the stress distribution in and around a venous wall to determine the biomechanical response of varicose veins by using compression sock treatment through development of 2D FEM (Rohan, et al. 2013). It can be seen that the ECS fabrics are effective in narrowing leg veins. Zhang et al. investigated the interface pressure effected by ECS compression with different shapes for design optimization using FEM code (Matlab software) (Zhang, et al. 2019), and the results showed that the pressure values are affected by the processing parameters on the structure parameters as well as design parameters.

2.6 Parameter Optimization of the ECS-leg System

The parameter optimization is a method to bring the design results closer to the target value by adjusting the related parameters, which is widely applied in the mechanics, economic, mathematics, and architecture (Aleti, et al. 2012; Khan, et al. 2021; Zhang, et al. 2023; Wang, et al. 2008).

Wei et al. applied the optimization method to achieve the target stress of lower rocker arm by adjusting lower racker mass (Wei, et al. 2021). In the ECS-leg system, parameter optimization method is widely applied to determine the parameters related with ECS and leg geometry and mechanical properties to achieve target pressure level. Lin et al. developed an optimization method to achieve a special pressure and Von-Mises stress value with consideration of hyperelastic coefficient, thickness, and strain of the ECS fabrics (Lin, et al. 2011). Jamshaid et al. used parameter optimization method to reach the better wearing comfort level of the ECS fabrics by changing the ECS stretch, thickness, and Areal density (Jamshaid, et al. 2022). The optimization can be also applied in other compression garments, Liang et al. provided a nonlinear

FEM to simulate the female breast with the optimization of the fabric properties of the sports bra (Liang, et al 2020).

However, few studies have systematically analyzed which parameters influenced the pressure values sensitively and the corresponding parameter ranges for achieving the specific pressure level have not been reported. Therefore, a parameter optimization model would be built in Chapter 8 to determine the sensitive parameters and the quantified ranges for achieving the target pressure levels.

2.7 Summary of Literature Review

2.7.1 Systematic Review

In general, numerical simulation provides a tool to enhance our understanding of the interaction mechanisms between the human body and compression fabrics. Existing studies has been solved follow problems, for example, (i) sensor measurement methods and Laplace’s law methods can obtain the interface pressures through direct experimental tests and formula calculation; (ii) ECS fabrics can be regarded as an isotropic or a 2D orthotropic elastic model, and the corresponding mechanical properties can be determined by KES and Instron system; (iii) the existing zero dimension (0D), one dimension (1D) or two dimension (2D) flow model can calculate the local venous velocities, and (iv) the existing optimization method can assist to determine related parameters to achieve target pressure values.

2.7.2 Problem Statement

However, some limitations still exist in the aforementioned studies, for example, (i) Laplace's law and sensor measurement methods cannot reflect the mechanical transmission of ECSs from the skin surface to the deeper soft tissues; (ii) ECS fabrics that were regarded as an isotropic or a 2D orthotropic elastic model cannot reveal the actual interactive mechanism within a 3D scale (i.e., along fabric course, wale, and thickness directions) when being applied on the body under stretching; (iii) the existing 0D, 1D or 2D flow model cannot three dimensionally display the venous hemodynamic response under the action of ECSs; and (v) the existing optimization method cannot balance the pressure function and wearing comfort, thus, cannot assess the ECS fabrics function comprehensively; and (vi) the existing optimization method did not conduct the parameter sensitivity analysis to determine the parameters that most sensitively influenced the pressure magnitudes.

To address the aforementioned problems, a new method to determine mechanical properties of ECS fabrics in a 3D scale was constructed in this study to reveal the actual interactive mechanism in the FE ECS-leg system in Chapter 3; a new FE model to reflect the mechanical transmission effects of the ECSs from the skin surface to the deeper tissue structures were developed in Chapters 4 and 5; the new FSI models to investigate the venous hemodynamic responses under the action of ECSs with different material and pressure levels were proposed in Chapter 6; a comfort assessment method based on subjective surveys to optimize the pressure function and wearing comfort was applied in Chapter 7; and a sensitive analysis integrated with an optimization method to determine the critical design parameters that sensitively influenced pressure performances as well as their corresponding ranges were developed in Chapter 8 for achieving the pressure levels with balanced wearing comfort for target end users.

CHAPTER 3 NEW ANALYTICAL MODELLING TO DESIGN ECS MATERIAL PROPERTIES

3.1 Introduction

The critical mechanical properties of the ECS fabrics to characterize tension, shearing, compression, bending, and recovery properties (Mosti, et al. 2010; Silva, et al. 2014) are the important physical-mechanical parameters for FE modelling to numerically simulate and analyze mechanical behaviors and interaction responses between the ECS fabrics and the lower limbs. In the previous studies, the methods of determining ECS materials properties were complex and cannot holistically reflect fabric properties, especially along the thickness directions.

To address these issues, this Chapter introduces a systematic approach for determining the elastic moduli of ECS fabrics on a 2D and 3D scales to exhibit the effects of the designed material properties on pressure performances of ECSs. This approach entailed the integration of orthotropic theoretical analysis, model development, and experimental testing and validation. This new analytical model was derived to determine the elastic moduli of ECS fabrics along the three dimensions (wale, course, and thickness directions). By applying the 2D and 3D elastic moduli derived for ECS fabric samples, respectively, through a developed FE model, we simulated the interface pressure values (magnitude and distribution) exerted by the ECS fabrics and verified the simulation results through comparisons with experimentally measured pressure values. The results indicated that the proposed approach can more realistically determine the 3D mechanical properties of ECS fabrics and improve the FEM simulation precision for ECS analysis, thus promoting pressure dose design, selection, and control of ECSs for improved compression therapy. These determined mechanical properties of ECS fabrics in a 3D scale would be further input to the FE modeling in Chapter 5 for simulating the effects of elastic fabrics on the interface pressure performances of ECSs.

3.2 Methods

3.2.1 Fundamental Studies of Mechanical Properties of Elastic Fabrics

The ECS fabrics can be assumed as an orthotropic material with differential mechanical properties along course and wale directions. RAL-GZ 387/1 standard shows the requested elongations (strain ranges) of the ECS fabrics are between 15% and 120%. To detect the linear properties of the ECS fabrics, Figure 3.1 shows that the average linear regression coefficients (R^2) of the ECS fabrics in the course and wale directions were approximately 0.998 and 0.982, respectively. The goodness-of-fit values obtained for the tested ECS fabric samples were greater than 0.97. Through practical testing, it was found that the stretched ECS fabrics presented linear properties within these tensile range. Thus, the mechanical properties of ECS fabrics can be determined based on Hooke's Law, which is a principle to describe a linear relationship between stress and strain under a specific deformation including uniaxial tension, compression, shear, or bending. It can be expressed as follows,

$$[\varepsilon]=[S][\sigma] \tag{3.1}$$

where σ and ε are the stress and the strain, and S is the compliance matrix, which is related with the mechanical properties respectively. Among them, the stress and strain can be measured by the Instron and KES system under the aforementioned deformation (uniaxial tension, compression, shear, or bending). Thus, the analytical model to determine the relationship among the stress, strain, and mechanical properties of the ECS fabrics were constructed in the follow Chapters.

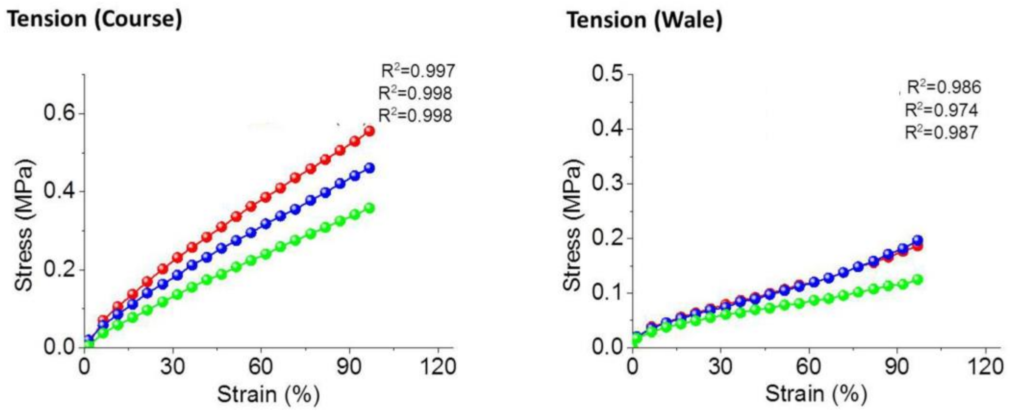

Figure 3.1 The linear regression coefficient (R^2) of the studied ECS fabrics.

3.2.2 New 2D Analytical Modelling for Determining ECS Fabric Properties

The ECS fabrics are commonly assumed as an orthotropic lamina as the mechanical properties along their course and wale directions are different (Fig 3.1). The relationship between the stress and strain can be expressed based on the generalized Hooke's law as below:

$$\begin{bmatrix} \varepsilon_x \\ \varepsilon_y \\ \gamma_{xy} \end{bmatrix} = \begin{bmatrix} S_{11} & S_{12} & S_{16} \\ S_{21} & S_{22} & S_{26} \\ S_{61} & S_{62} & S_{66} \end{bmatrix} \begin{bmatrix} \sigma_x \\ \sigma_y \\ \tau_{xy} \end{bmatrix} \tag{3.2}$$

where $[S_{ij}]$ is the orthotropic compliance matrix (OCM) of the ECS fabrics, ε_i and γ_{ij} are the normal strain and shear strain, respectively, and σ_i and τ_{ij} are the normal stress and shear stress, respectively. The OCM of the ECS fabrics indicates the relationship between stress and strain (Silva, et al 2014), which can be determined based on the orthogonal elastic moduli of the ECS fabrics. It can be expressed as below,

$$\begin{bmatrix} \varepsilon_x \\ \varepsilon_y \\ \gamma_{xy} \end{bmatrix} = \begin{bmatrix} \frac{1}{E_x} & -\frac{v_{yx}}{E_y} & 0 \\ -\frac{v_{xy}}{E_x} & \frac{1}{E_y} & 0 \\ 0 & 0 & \frac{1}{G_{xy}} \end{bmatrix} \begin{bmatrix} \sigma_x \\ \sigma_y \\ \tau_{xy} \end{bmatrix}$$

(3.3)

where *E*, *v*, and *G* are the Young's modulus, Poisson's ratio, and shear modulus of the elastic fabrics, respectively. The *x* and *y* are the two principal stress directions of the elastic fabric, corresponding to fabric course and wale directions, respectively.

The *E* of ECS fabric is a mechanical property that measures its tensile stiffness, which can be determined by using a uniaxial tension testing to obtain fabric stress-strain curves along both course and wale directions. In the uniaxial tensile testing, $\sigma_y = 0$ when the ECS fabrics are stretched along the course direction (*x*), then the OCM of the ECS fabrics can be presented as below,

$$E_x = \frac{\sigma_x}{\varepsilon_x} \tag{3.4}$$

where σ_x and ε_x denotes the tensile stress and tensile strain of the ECS fabric along its course direction, respectively. Correspondingly, when the ECS fabrics are stretched along wale direction (*y*), the OCM of the ECS fabrics can be presented as below,

$$E_y = \frac{\sigma_y}{\varepsilon_y} \tag{3.5}$$

where σ_y and ε_y are the tensile stress and strain along the fabric wale direction, respectively.

The v is also a key parameter reflecting mechanical property of ECS fabrics, which describes the deformation (expansion or contraction) of the fabric along a specific direction. The uniaxial tension testing was applied to determine v of the studied ECS fabric. Based on the OCM of the ECS, Poisson's ratios can be determined as follows,

$$v_{xy} = -\frac{\varepsilon_y E_x}{\sigma_x} \tag{3.6}$$

The G of the ECS fabric is a measure of elastic shear stiffness and is defined as the ratio of shear stress to shear strain. A shear testing was applied to measure shear stress and shear strain within a plane. The OCM of the ECS fabric can be presented as below,

$$G_{xy} = \frac{\tau_{xy}}{\gamma_{xy}} \tag{3.7}$$

where τ_{xy} is shear stress in the plane and γ_{xy} is shear strain in the corresponding plane, respectively.

3.2.3 New Methods for Determining 3D ECS Fabric Properties

The E, v, and G along the course and wale direction of the ECS fabrics have been determined based on our developed 2D analytical model, which can be applied to input into the FE model to numerically simulate the mechanical performances in the ECS-leg system. However, it cannot reflect the mechanical properties along the thickness direction, thus, an analytical model based on 3D generalized Hooke's law were developed to determine the mechanical properties in a 3D scale in this Chapter.

The essential elastic moduli of ECS fabrics (i.e., E, v, and G) predominantly govern the degree of fabric deformation and resultant biomechanical effects exerted on the lower limb. It facilitates the maintenance of linear elasticity in stretching, the application of appropriate tension, recovery after repeated uses, and donning and doffing in practical uses.

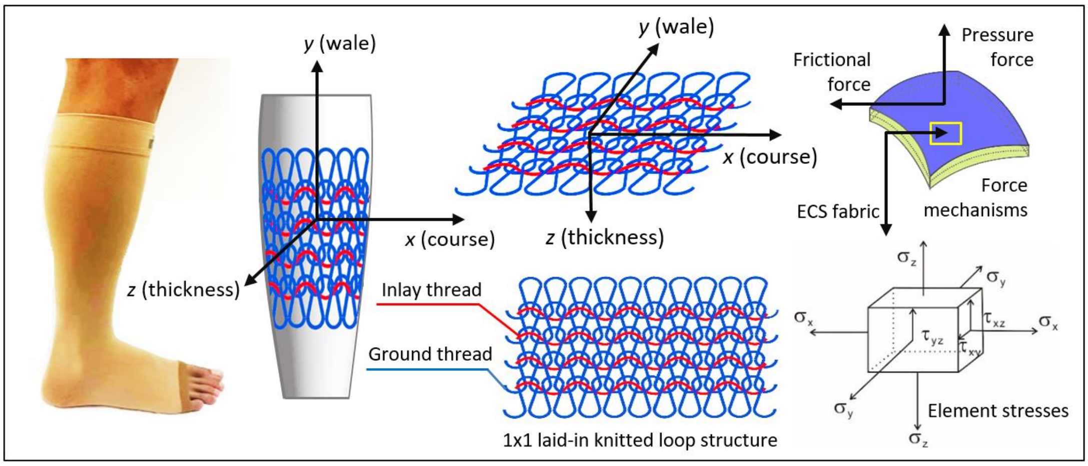

Figure 3.2 The determined course, wale, and thickness directions of the ECS fabric with laid-in knitted loop structure in this study.

Hooke's law describes the linear relationship between the stress and strain of materials under a specific deformation condition (e.g., uniaxial tension, compression, shear, or bending; Figs. 3.2 and 3.3). It can be applied to analyze the mechanical parameters (E, v, and G) of ECS fabrics and their variations under deformation when applied to the lower limbs. Eq. 3.8 presents the generalized Hooke's law in a 3D scale.

$$\begin{bmatrix} \varepsilon_x \\ \varepsilon_y \\ \varepsilon_z \\ \gamma_{xy} \\ \gamma_{xz} \\ \gamma_{yz} \end{bmatrix} = \begin{bmatrix} S_{11} & S_{12} & S_{13} & S_{14} & S_{15} & S_{16} \\ S_{21} & S_{22} & S_{23} & S_{24} & S_{25} & S_{26} \\ S_{31} & S_{32} & S_{33} & S_{34} & S_{35} & S_{36} \\ S_{41} & S_{42} & S_{43} & S_{44} & S_{45} & S_{46} \\ S_{51} & S_{52} & S_{53} & S_{54} & S_{55} & S_{56} \\ S_{61} & S_{62} & S_{63} & S_{64} & S_{65} & S_{66} \end{bmatrix} \begin{bmatrix} \sigma_x \\ \sigma_y \\ \sigma_z \\ \tau_{xy} \\ \tau_{xz} \\ \tau_{yz} \end{bmatrix} \tag{3.8}$$

where $[S_{ij}]$ is the OCM of the ECS fabrics; ε_i and γ_{ij} are the normal strain and shear strain, respectively; and σ_i and τ_{ij} are the normal stress and shear stress, respectively. The OCM indicates the relationship between stress and strain (Silva, et al 2014), which can be determined by the orthogonal elastic moduli of ECS fabrics, as expressed in the following equation:

$$\begin{bmatrix} \varepsilon_x \\ \varepsilon_y \\ \varepsilon_z \\ \gamma_{xy} \\ \gamma_{xz} \\ \gamma_{yz} \end{bmatrix} = \begin{bmatrix} \frac{1}{E_x} & -\frac{v_{yx}}{E_y} & -\frac{v_{zx}}{E_z} & 0 & 0 & 0 \\ -\frac{v_{xy}}{E_x} & \frac{1}{E_y} & -\frac{v_{zy}}{E_z} & 0 & 0 & 0 \\ -\frac{v_{xz}}{E_x} & -\frac{v_{yz}}{E_y} & \frac{1}{E_z} & 0 & 0 & 0 \\ 0 & 0 & 0 & \frac{1}{G_{xy}} & 0 & 0 \\ 0 & 0 & 0 & 0 & \frac{1}{G_{xz}} & 0 \\ 0 & 0 & 0 & 0 & 0 & \frac{1}{G_{yz}} \end{bmatrix} \begin{bmatrix} \sigma_x \\ \sigma_y \\ \sigma_z \\ \tau_{xy} \\ \tau_{xz} \\ \tau_{yz} \end{bmatrix} \tag{3.9}$$

Here, x, y, and z are the three principal stress directions (Fig. 3.2) that indicate the corresponding course, wale, and thickness directions of the knitted ECS fabric under examination, respectively. The orthogonal relationship between E and v along the three coordinate directions can be expressed as follows:

$$-\frac{v_{xy}}{E_y} = -\frac{v_{yx}}{E_x}; -\frac{v_{xz}}{E_z} = -\frac{v_{zx}}{E_x}; -\frac{v_{yz}}{E_z} = -\frac{v_{zy}}{E_y} \tag{3.10}$$

Thus, the three dimensional E (E_x , E_y, and E_z), v (v_{xz}, v_{yz}, and v_{xy}), and G (G_{xy} , G_{xz} , and G_{yz}) values of ECS fabrics can be determined based on the stress and strain properties of the ECS fabrics.

E_x, E_y, and E_z indicate the 3D tensile stiffnesses of an ECS fabric, which can be determined using stress–strain curves along the course, wale, and thickness directions of the fabric through uniaxial tensile testing and compression tests (Fig. 3.3 a-b). In a uniaxial tensile test, the tensile stress along the wale direction σ_y is equal to zero, and the compressive stress along the thickness direction σ_z is equal to zero when the ECS fabric is stretched along the course direction x. Thus, the OCM of the ECS fabric can be presented as follows:

$$E_x = \frac{\sigma_x}{\varepsilon_x} \tag{3.11}$$

where σ_x and ε_x denote the tensile stress and tensile strain, respectively, of the ECS fabric along the course direction. When the ECS fabric is stretched along the wale direction y or compressed along the thickness direction z, the OCMs of ECS fabric can be written as follows,

$$E_y = \frac{\sigma_y}{\varepsilon_y}; E_z = \frac{\sigma_z}{\varepsilon_z} \tag{3.12}$$

where ε_y and ε_z are the tensile strain along the wale direction and compressive strain along the thickness direction, respectively. In addition, v is a crucial mechanical parameter that describes the ECS fabric expansion or contraction deformation along the direction perpendicular to the loading (compression or stretching) direction (Silva, et al. 2014). v_{xy}, v_{xz}, and v_{yz} along the wale, course, and thickness directions can be determined by using uniaxial tensile tests. The OCMs for v_{xy}, v_{xz}, and v_{yz} are presented as follows:

$$v_{xy} = -\frac{\varepsilon_y E_x}{\sigma_x}; v_{xz} = -\frac{\varepsilon_z E_x}{\sigma_x}; v_{yz} = -\frac{\varepsilon_z E_y}{\sigma_y} \tag{3.13}$$

G indicates the elastic shear stiffness, which can be defined as the ratio of shear stress to shear strain (Silva, et al. 2014). A shear test can be used to measure the shear stress and shear strain within a plane (Fig. 3.3). The OCM for G in a 3D plane can be expressed as follows:

$$G_{xy} = \frac{\tau_{xy}}{\gamma_{xy}}; G_{xz} = \frac{\tau_{xz}}{\gamma_{xz}}; G_{yz} = \frac{\tau_{yz}}{\gamma_{yz}} \tag{3.14}$$

where G_{xy}, G_{xz}, and G_{yz} represent the shear stress along the course–wale (x–y), course–thickness (x–z), and wale–thickness (y–z) planes, respectively, G_{xy}, G_{xz}, and G_{yz} represent the shear strains in these planes, respectively. In practical tests, directly measuring τ_{xz}, τ_{yz}, γ_{xz}, and γ_{yz} in the x–z and y–z planes are difficult because ECS fabrics are usually thin (< 1.2mm) and few instruments are available for direct testing.

Therefore, an analytical model based on bending measurements was developed in the present study to facilitate the derivation of G_{xz} and G_{yz} in the x–z and y–z planes, respectively.

In the bending test of the proposed model, an ECS fabric is regarded as a cantilever beam structure in which one end is supported but the other end extends horizontally (Silva, et al. 2014). The bending load is caused by the fabric's own weights, and its deflection (i.e., the bending deformation along the loading direction) can be measured as illustrated in Fig. 3.3, where h and b_x denote the original thickness and edge width, respectively, of the ECS fabric, and l denotes the edge length of the deformed ECS fabric during bending.

The relationship among G_{yz} and G_{xz}, bending loading, and bending deformation along the z direction can be derived using the Airy stress function (Van, et al. 2007). The Airy stress function is a semi-inverse method for determining the loading conditions for plane stress or plane strain problems based on the mechanical equilibrium equation (Sitharam, et al. 2021). It can be expressed for isotropic elastic materials as follows:

$$\frac{\partial^4 U}{\partial y^4} + \frac{\partial^4 U}{\partial z^2 \partial y^2} + \frac{\partial^4 U}{\partial z^4} = 0 \tag{3.15}$$

The orthotropic Airy stress function can be derived on the basis of the isotropic Airy stress function as follows:

$$S_{33}\frac{\partial^4 U}{\partial y^4}+\left(2S_{23}+S_{66}\right)\frac{\partial^4 U}{\partial z^2\partial y^2}+S_{22}\frac{\partial^4 U}{\partial z^4}=0 \tag{3.16}$$

where S_{33}, S_{23}, S_{22}, and S_{66} are the coefficients corresponding to the compliance matrix (Eq. 3.9); U is the orthotropic Airy stress function.

In this cantilever beam bending test in the proposed model, the bending stress σ_z of the ECS fabric is generated by its bending loading q (self-weight), which is a constant. σ_z is a function of z. U can be further determined by applying Eq. 3.17 through the use of Eq. 3.16:

$$U=\frac{y^2}{2}f(z)+yf_1(z)+f_2(z) \tag{3.17}$$

Eq. 3.17 can be substituted into Eq. 3.16 as follows:

$$\frac{1}{2E_y}\frac{\mathrm{d}^4 f(z)}{\mathrm{dz}^4}y^2+\frac{1}{E_y}\frac{\mathrm{d}^4 f_1(z)}{\mathrm{dz}^4}y+\frac{1}{E_y}\frac{\mathrm{d}^4 f_2(z)}{\mathrm{dz}^4}+\left(\frac{1}{G_{yz}}-\frac{2v_{yz}}{E_y}\right)\frac{\mathrm{d}^2 f(z)}{\mathrm{dz}^2}=0 \tag{3.18}$$

According to Eq. 3.18, all items must be zero to satisfy the Airy stress function, which is expressed as follows,

$$\frac{\mathrm{d}^4 f(z)}{\mathrm{dz}^4}=0;\frac{\mathrm{d}^4 f_1(z)}{\mathrm{dz}^4}=0;\left(\frac{1}{G_{yz}}-\frac{2v_{yz}}{E_y}\right)\frac{\mathrm{d}^2 f(z)}{\mathrm{dz}^2}=0 \tag{3.19}$$

Consequently, Eq. 3.19 can be derived as follows:

$$\begin{aligned}&f(z)=Ay^3+By^2+Cy+D;\\&f_1(z)=Ey^3+Fy^2+Gy;\\&f_2(z)=Hy^5+Iy^4+Jy^3+Ky^2\end{aligned} \tag{3.20}$$

where A to K are the undetermined coefficients. Thus, the determined U can be derived as follows:

$$U=\frac{y^2}{2}(Az^3+Bz^2+Cz+D)+y(Ez^2+Fz^2+Gz)+Hz^5+Iz^4+Jz^3+Kz^2 \tag{3.21}$$

On the basis of the Airy stress function, the relationship between the normal stress, shear stress, and stress function of the ECS fabric during bending can be derived as follows:

$$
\begin{aligned}
\sigma_y &= \frac{\partial^2 U}{\partial z^2} = \frac{y^2}{2}(6Az+2B) + y(6Ez+2F) + 20Hz^3 + 12Iz^2 + 6Jz + 2K; \\
\sigma_z &= \frac{\partial^2 U}{\partial y^2} = 2(z^3 + Bz^2 + Cz + D); \\
\tau_{yz} &= -\frac{\partial^2 U}{\partial z \partial y} = -y(6Az^2 + 4Bx + 2C) - (3Ez + 2Fz + G)
\end{aligned}
\tag{3.22}
$$

The boundary conditions of the ECS fabric under bending deformation can be expressed as follows:

$$
(\sigma_z)_{z=-\frac{h}{2}} = -q; (\tau_{yz})_{z=-\frac{h}{2}} = 0; (\sigma_z)_{z=\frac{h}{2}} = 0; (\tau_{yz})_{z=\frac{h}{2}} = 0; (\tau_{yz})_{y=0} = 0; \int_{-\frac{h}{2}}^{\frac{h}{2}} (\sigma_y)_{y=0} \mathrm{d}z = 0; \int_{-\frac{h}{2}}^{\frac{h}{2}} z(\sigma_y)_{y=0} \mathrm{d}z = 0
\tag{3.23}
$$

Furthermore, the stress components of the ECS fabric can be derived using Eq. 3.23:

$$
\begin{aligned}
\sigma_y &= -\frac{qy^2 z}{2I} - \frac{q(2v_{yz} - \frac{E_y}{G_{yz}})}{2I}\left(\frac{1}{3}z^3 - \frac{h^2}{20}z\right); \\
\sigma_z &= -\frac{q}{b_y 2}\left(1 - \frac{3z}{h} + \frac{4z^3}{h^3}\right); \\
\tau_{yz} &= \frac{q}{2I}\left(z^2 - \frac{h^2}{4}\right)y
\end{aligned}
\tag{3.24}
$$

where σ_y and σ_z represents the normal stresses along the wale and thickness directions of the ECS fabric, respectively. τ_{yz} represents the shear stress in the y–z plane; and I represents the inertia moment. On the basis of Eq. 3.9, the normal strain and shear strain can be derived as follows:

$$
\begin{aligned}
\varepsilon_y &= -\frac{qy^2 z}{2E_y I} - \frac{q(2v_{yz} - \frac{E_y}{G_{yz}})}{2E_y I}(\frac{1}{3}z^3 - \frac{h^2}{20}z) + \frac{qv_{zy}}{2b_y E_z}(1 - \frac{3z}{h} + \frac{4z^3}{h^3});\\
\varepsilon_z &= -\frac{q}{2b_y E_z}(1 - \frac{3z}{h} + \frac{4z^3}{h^3}) + \frac{qv_{yz}y^2 z}{2E_y I} - \frac{v_{yz}q(2v_{yz} - \frac{E_y}{G_{yz}})}{2E_y I}(\frac{1}{3}z^3 - \frac{h^2}{20}z);\\
\gamma_{yz} &= \frac{q}{2G_{yz}I}(z^2 - \frac{h^2}{4})y
\end{aligned}
\tag{3.25}
$$

where ε_y and ε_z are normal strains along the wale and thickness directions, respectively, and γ_{yz} is the shear strain in the *y*–*z* plane. Consequently, the bending deformation of the ECS fabric along the *y* and *z* directions can be expressed as follows:

$$
\begin{aligned}
v &= -\frac{qy^3 z}{6E_y I} - \frac{qP}{2E_y I}(\frac{1}{3}z^3 - \frac{h^2 z}{20})y + \frac{qv_{zy}}{2b_y E_z}(1 - \frac{3z}{h} + \frac{4z^3}{h^3})y + ff(z);\\
w &= -\frac{q}{2b_y E_z}(z - \frac{3z^2}{2h} + \frac{z^4}{h^3}) + \frac{qv_{yz}y^2 z^2}{4E_y I} - \frac{v_{yz}q(2v_{yz} - \frac{E_y}{G_{yz}})}{2E_y I}(\frac{1}{12}z^4 - \frac{h^2 z^2}{40}) + \varphi(y)
\end{aligned}
\tag{3.26}
$$

where *v* and *w* denote the bending deformation (displacement) along the *y* and *z* directions, respectively; correspondingly, *ff*(*z*) and *φ*(*y*) denote the undetermined function to satisfy the relationship between the strain and deformation.

According to Eqs. 3.25 and 3.26, the following relationship can be derived:

$$
\frac{d\varphi(y)}{dy} + \frac{qv_{yz}yz^2}{2E_y I} - \frac{qy^3}{6E_y I} - \frac{q(2v_{yz} - \frac{E_y}{G_{yz}})}{2E_y I}(z^2 - \frac{h^2}{20})y + \frac{qv_{zy}}{2E_z}(\frac{3}{b_y h} + \frac{z^2}{I})y + \frac{dff(z)}{dz} = \frac{q}{2G_{yz}I}(z^2 - \frac{h^2}{4})y
\tag{3.27}
$$

The boundary condition of the bending deformation of the ECS fabric can be expressed as follows:

$$
(v)_{y=l,z=0} = 0; (w)_{y=l,z=0} = 0; (\frac{\partial w}{\partial y})_{y=l,z=0} = 0 \tag{3.28}
$$

On the basis of Eq. 3.28, the separation-of-variables method can be applied to determine the relationship between the fabric bending deformation along the *z* direction w_y, q, and G_{yz}, as indicated in the following expression:

$$w_y = \frac{qL^4}{8E_yI_y} - \frac{q(2v_{yz} - \frac{E_y}{G_{yz}})L^2h^2}{80E_yI_y} - \frac{3qv_{yz}L^2}{4b_yE_yh} - \frac{qh^2L^2}{16G_{yz}I_y} \tag{3.29}$$

Similarly, the relationship between w_x, q, and G_{xz} can be expressed as follows:

$$w_x = \frac{qL^4}{8E_xI_x} - \frac{q(2v_{xz} - \frac{E_x}{G_{xz}})L^2h^2}{80E_xI_x} - \frac{3qv_{xz}L^2}{4b_xE_xh} - \frac{qh^2L^2}{16G_{xz}I_x} \tag{3.30}$$

On the basis of Eqs. 3.29 and 3.30, G in x–z and y–z planes of the ECS fabric can be determined as follows:

$$\begin{aligned} G_{xz} &= -\frac{qh^2L^2}{20I_x(w_x - \frac{qL^4}{8E_xI_x} + \frac{3qv_{xz}L^2}{4E_xb_xh} + \frac{qv_{xz}L^2h^2}{40E_xI_x})} \\ G_{yz} &= -\frac{qh^2L^2}{20I_y(w_y - \frac{qL^4}{8E_yI_y} + \frac{3qv_{xz}L^2}{4E_xb_yh} + \frac{qv_{yz}L^2h^2}{40E_yI_y})} \end{aligned} \tag{3.31}$$

Based on the developed analytical model, the relationships among the mechanical properties (E, v, and G), stress, strain, and deformation of the ECS fabrics have been determined. Based on the determined relationships, the values of E, v, and G can be further obtained with the aid of experimental testing (Fig. 3.3) as shown in Chapter 3.2.3, in detail.

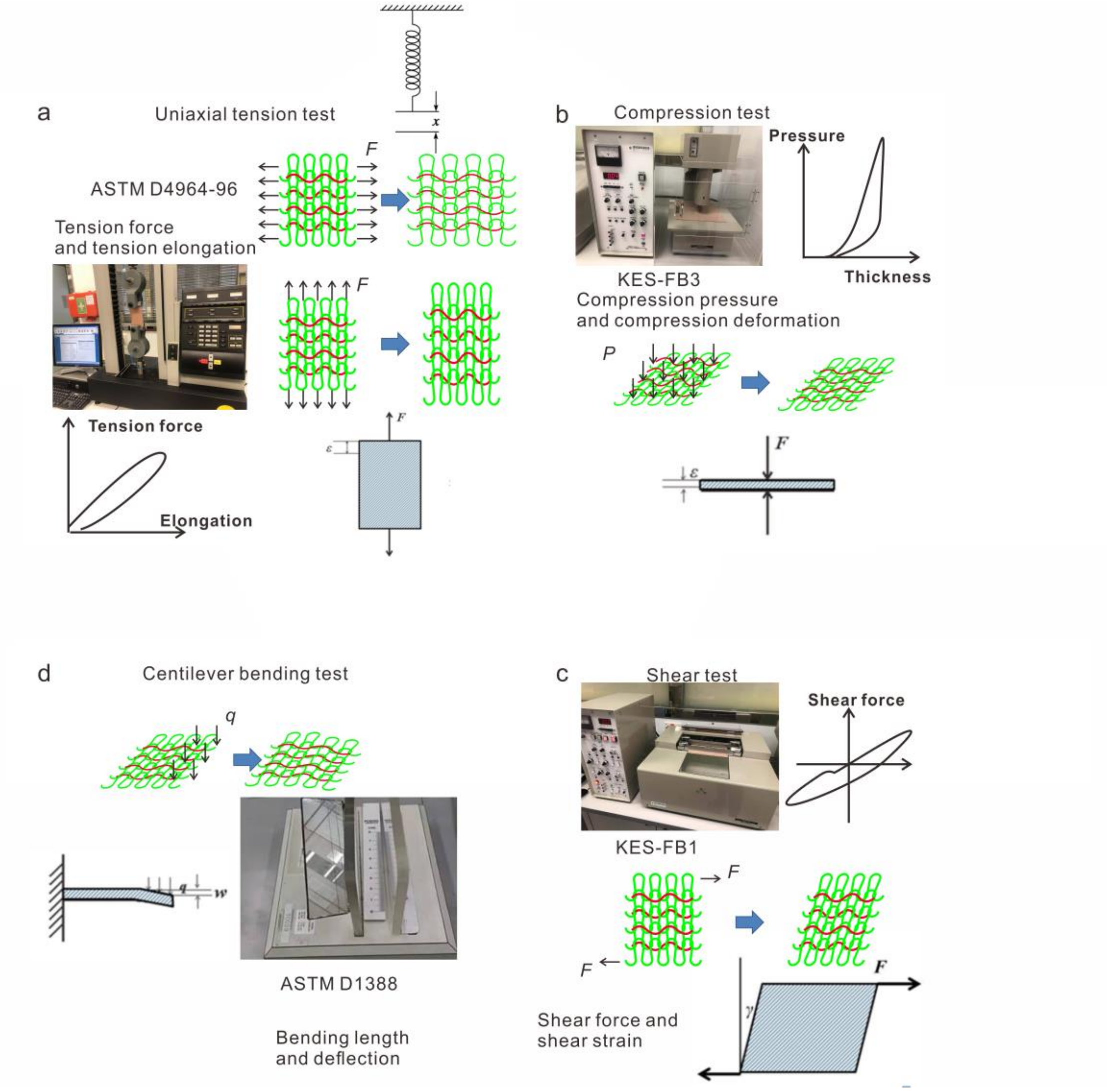

Figure 3.3 Applied experimental testing system for determination of mechanical properties of ECS fabrics, including (a) uniaxial Instron 4411 tension testing for E_x, E_y, v_{xy}, v_{xz}, and v_{yz}; (b) compression testing (KES-FB3) for Ez , (c) shearing testing (KES-FB1) for G_{xy} ; and (d) cantilever beam bending (shirley stiffness) testing for Gxz and Gyz.

3.2.4 Experimental Investigation of ECS Properties

Preparation of ECS Fabric Samples

Nine samples of tailor-made knitted tubular ECS fabrics that were footless and composed of interloped ground and inlay yarns were prepared and equipped with 1×1 laid-in loop structures (Fig. 3.2) (Liu, et al. 2016) to provide pressure gradients at the ankle, calf, and knee portions (e.g., Class-I: 70-100% at the brachial, 50-80% at the calf, Class-II: 70-100% at the brachial, 50-80% at the calf, and Class-III: 70-100% at the brachial, 50-70% at the calf corresponding with pressure values at the ankle). Polyamide double-covered Lycra yarns with a linear density of 40D/40D/40D were used as the ground threads that were knitted into loops to provide substrate fabric thickness, and polyamide-double covered Lycra yarns with a linear density of 240D/40D/40D were used as the inlay threads that were laid into the substrate structure without knitting into the knitted loops during the same knitting cycle, as to regulate the fabric tension and pressure doses. The geometric structures of laid-in knitted loops were stretched, compressed, and bent under the actions of the mechanical forces (Fig.3.2). Table 3.1 presents the physical characteristics of the prepared ECS fabric samples. Sample codes S1/S2/S3, S4/S5/S6, and S7/S8/S9 indicate the knee, calf, and ankle segments of the corresponding A, B, and C groups of the studied ECS fabrics, respectively. Prior to testing, all samples were placed in an environmentally controlled laboratory (relative humidity: 65% ± 2%, temperature 21±1°C) for 48 h to reach equilibrium.

Table 3.1 Physical characteristics of the prepared knitted tubular ECS fabric samples.

Group	**Section**	**Sample code**	**Course stitch densities (courses/inch)**	**Wale stitch densities (wale/inch)**	**Thickness (mm)**	**Mass density (g/m^2)**
A	Knee	S1	44	37	0.75	319
	Calf	S2	48	40	0.76	365
	Ankle	S3	55	46	0.72	413
B	Knee	S4	43	36	0.70	286
	Calf	S5	46	38	0.74	308
	Ankle	S6	50	39	0.77	370
	Knee	S7	54	42	0.77	436

C	Calf	S8	59	45	0.75	372
	Ankle	S9	72	58	0.76	330

Experimental Tests of ECS Fabric Samples

The microstructural and tensile and shearing deformation of the ECS fabrics are illustrated in Fig. 3.3. ECS fabric samples measuring 100 mm (length) × 75 mm (width) per piece were prepared for tensile tests using an Instron 4411 system (Norwood, MA, USA; Fig. 3.3). The tensile tests were performed to produce stress–strain curves along the course (x) and wale (y) directions of the prepared ECS fabrics at a standard tensile rate of 10 mm/s; these tests were conducted in accordance with the ASTM D4964-96 standard. On the basis of the derived stress–strain curves, E_x and E_y were calculated using Eqs. 3.11 and 3.12. To determine E_z along the thickness direction, a Vernier caliper was used for thickness measurement. Stress–strain curves reflecting the relationship between compressive pressure and compressive thickness were obtained using the KES-FB3 testing system (Kawabata evaluation system, Kyoto, Japan); thus, E_z could be determined using Eq. 3.12 (Fig. 3.3).

To determine v for the tested ECS fabric samples on a 3D scale, the contraction of the fabrics during transverse deformation under uniaxial tension was measured using the Vernier caliper that was put to align with the thickness of the tested fabrics. On the basis of the measured contraction and stretching, v_{xy}, v_{xz}, and v_{yz} were calculated using Eq. 3.13. Shear stress–strain curves were obtained for the ECS fabrics by testing the fabric samples with a size of 200 mm × 200 mm per piece on a pure shear test (KES-FB1) at an 8° shear angle (Fig. 3.3c). Subsequently, G_{xy} was calculated using Eq. 3.14. To determine G_{xz} and G_{yz}, the weights (kg) of ECS fabric samples measuring 200 mm

× 25 mm were measured using a BP211D electronic balance (Sartorius, Germany), and their *w* values (mm) were determined using a Shirley Stiffness tester (Testex, China) in accordance with the ASTM-D 1388-2014 standard (Fig. 3.3). Thus, G_{xz} and G_{yz} of the studied ECS fabrics were obtained by applying Eq. 3.31.

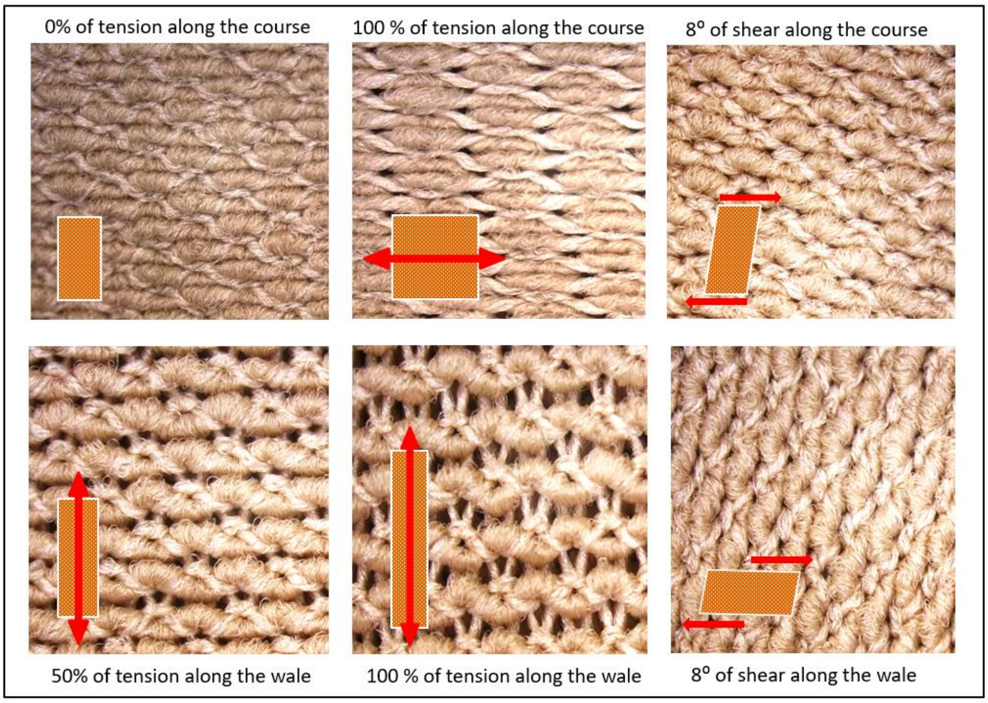

Figure 3.4 Microstructures of laid-in knitted ECS fabrics under different mechanical deformation in testing.

3.2.5 FE Modelling an ECS-Rigid Leg (Rleg) System

Contact Analysis

To numerically analyze the interface pressure exerted by the ECS fabrics on the basis of their 2D and 3D mechanical properties, this study modeled a new FE ECS-Rleg system where the geometric FE leg models were constructed based on the three fabricated wooden leg models (WL-I, WL-II, WL-III) especially for Asian user bodies.

The shaped wooden leg models have rigid surface, round cross-sections, and three different sizes as shown in Table 3.2 and Fig. 3.5. The geometric FE ECS models were constructed based on the actual dimensions of the ECS fabric samples referred to our group developed size chart (Fig. 3.5a) by using ANSYS Workbench Design Modeler software (v19.2, ANSYS, Pennsylvania, Pittsburgh, USA). The 2D (E_x, E_y, v_{xy}, and G_{xy}) and 3D (E_x, E_y, E_z, v_{xy}, v_{xz}, v_{yz}, G_{xy}, G_{xz}, and G_{yz}) material mechanical properties were used as input parameters in the developed FE ECS models. The LS-Dyna explicit dynamic solver was used in Ansys for FE model through applying central difference method (Gravouil, et al. 2009) to discrete dynamic equation with less than 1% errors (Figueroa, et al. 2012). The FE leg models were constructed under the assumption that the wooden leg was isotropic elastic materials with E and v values of 500 MPa and 0.4, respectively (Alves, et al. 2013).

Meshing Construction

The FE ECS and FE leg models were meshed using linear quadrilateral elements and tetrahedrons elements with approximately 30,000 and 50,000 nodes, respectively (Fig. 3.5). To examine the meshing independence of the developed FE model, different meshing sizes (4,6, and 8 mm per element) were applied to the FE leg model (WL-II) using the FE ECS of Group C. The results indicated that the meshing size of 6 mm per element produced the best meshing quality with a value of 0.842, thus this meshing size was adopted to simulate interface pressure induced by ECSs. The constructed FE ECS and leg models were imported into ANSYS workbench LS-Dyna for FE analysis under a 4-core, 16 GB RAM, 512 GB SSD hardware computing system .

Boundary Conditions

The frictional nonlinear contact has been applied in the developed FE model based on the Augmented Lagrange equation, where the sliding resistance is proportional to the coefficient of the friction, and the free separation between the ECS and the wooden leg models was unimpeded. The boundary conditions of ECS deformation were determined based on an approximately 340-mm longitudinal displacement of the ECS fabric samples, in accordance with practical usage conditions (Fig. 3.5). The upper and bottom surfaces of the wooden leg model was fixed with the zero displacements of all nodes at x, y, and z directions in the boundary. The top edge of ECS can dynamically slide freely from the distal to the proximal leg model longitudinally. The center of the cross-sectional leg and ECS models were coincident to ensure ECS to slide exactly along the leg for achieving an alignment. The circumference of the ECS can deform freely with tubular fabric stretching with variation of leg volume. The total degree of freedoms (DOFs) of the built FE ECS-leg model was approximately 275000, where the DOFs of every node were six. The boundary conditions restricted the six DOFs of the upper and bottom surfaces of the FE leg model and the one DOF along the longitudinal direction of the FE ECS model for every node. Both 2D and 3D material mechanical parameters were applied to simulate the interface pressures by ECS fabrics.

Table 3.2 Geometric characteristics of the developed FE-Rleg and ECS models in the FEM

	Circumference (cm)				Height (cm)		
ECS samples	C1	C2	C3	C4	H1	H2	H3
Group A	17.6	18.9	16.2	14.8	5.0	14.0	5.0
Group B	21.7	23.7	19.7	16.7	6.0	12.0	6.0
Group C	23.9	26.4	19.6	16.3	5.0	13.0	6.0
Leg models	C1	C2	C3	C4	H1	H2	H3
WL-I	29.6	31.9	26.0	18.0	9.0	9.0	9.0
WL-II	34.0	35.9	29.4	20.3	9.0	9.0	9.0
WL-III	37.8	39.3	32.8	22.5	9.0	9.0	9.0

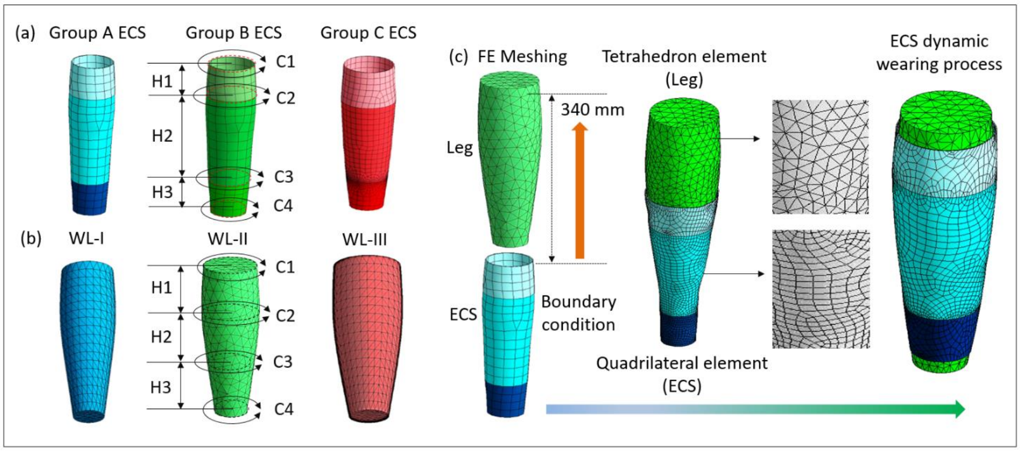

Figure 3.5 The developed geometric models of (a) FE ECSs and (b) FE Rlegs, and (c) the meshing and boundary conditions applied in the FEM.

3.2.6 Validation of the FE ECS-Rleg Modelling

To verify the simulated pressure values, an air-filled pneumatic pressure-sensing system was applied to directly detect the interface pressure between the wooden leg models and the ECS fabrics by placing the flexible pressure sensor probe with a diameter of 5 cm and a thickness of 0.2mm (PicoPress, Microlab Elettronica Sas, Italy; pressure range: 0-189 mmHg; deviation within ± 1mmHg) (Liu, et al. 2019) at 36 typical sites around the 4 directions (anterior, media, lateral, and posterior) and 3 height levels (ankle, calf, and knee) of the three tested wooden leg models (WL-I, WL-II, WL-III), sequentially. The average pressure value detected by the pressure sensor probe over the circular area on the wooden leg model was recorded. Similarly, in the Ansys numerical simulation, the interface pressure was also defined as the average pressure value obtained over the same circular area with a diameter of 5 cm on the FE leg model surface. The testing positions at the FE leg model and the corresponding wooden leg model were identical to ensure a consistent study condition between the simulated and the measured interface pressure. The deviations between the simulated and the measured pressure values were compared to verify the effectiveness of the 3D material mechanical properties in ECS pressure prediction (Fig. 3.6).

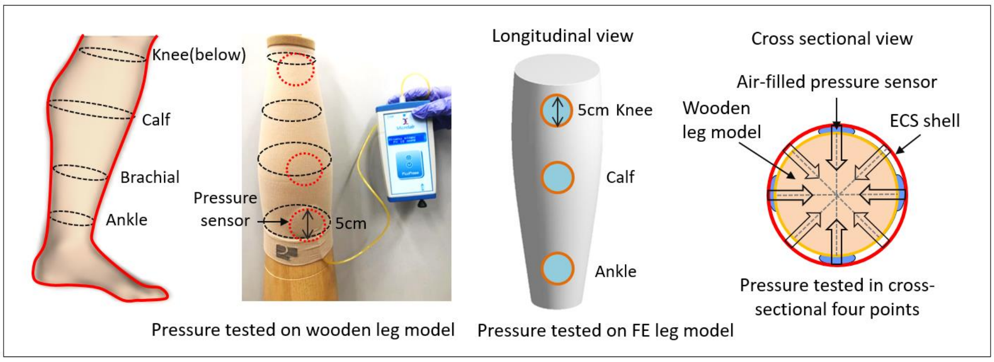

Figure 3.6 Experimental setting of pressure validation testing.

Fig. 3.7 presents the study flowchart, including orthotropic theoretical analysis, analytic model development, FEM, and experimental testing and validation. The constructed analytical models integrated with the experimental tests were used to establish the relationships between material elastic moduli, strain, and force loading behaviors of ECS fabrics. Mechanical properties of ECS fabrics and contacted bodies and geometric models of the contacted bodies are the input parameters for FEM. Interface pressure effects caused by using 2D and 3D mechanical properties of ECS fabrics were comparatively studied in the deviation ratios analysis.

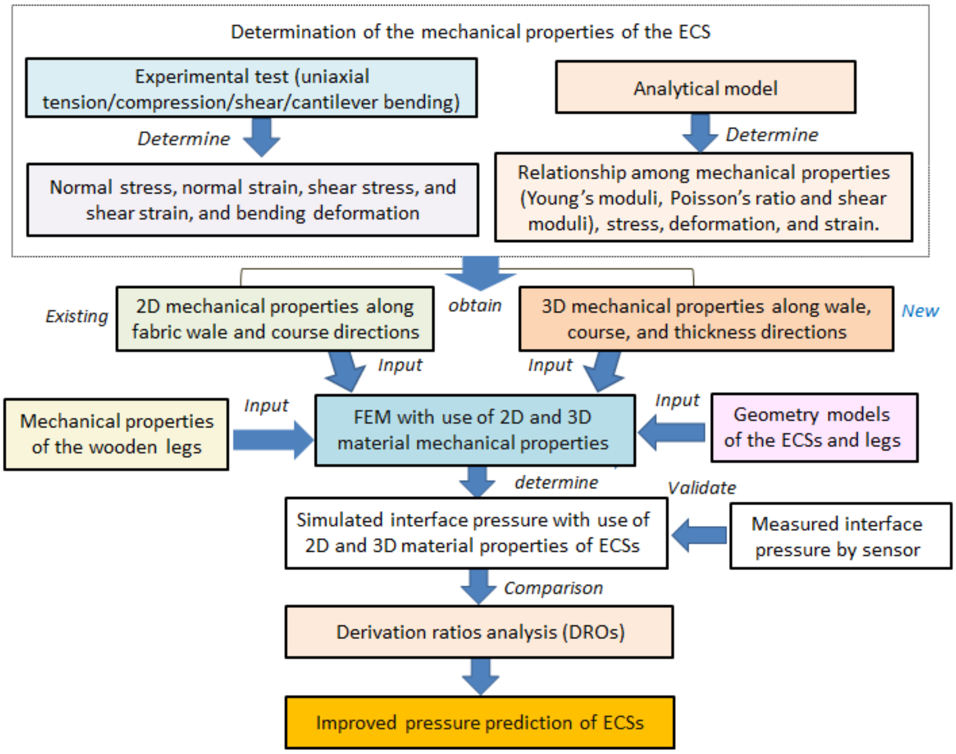

Figure 3.7 Framework of Chapter 3.

3.3 Results and Discussion

3.3.1 Determined 2D and 3D Mechanical Properties of ECS Fabrics

Table 3.3 presents the 2D and 3D mechanical properties of the ECS fabric samples. Fig. 3.8 illustrates the corresponding stress–strain curves along with linear regression coefficients. The goodness-of-fit values obtained for the tested ECS fabric samples were > 0.95 (R^2 > 0.95) at stretching ratios of 0%–100%. Overall, the derived E_x values were greater than the E_y and E_z values, implying that the ECS fabrics produced shorter stretches along the course direction to exert greater squeezing forces in order to deliver higher interface pressure levels to the leg models. The derived v_{xy}, v_{xz}, and v_{yz} values for the studied ECS fabrics were approximately 0.25. Overall, the derived

G_{xy} values were greater than the derived G_{yz} and G_{xz} values, indicating that the ECS fabrics could produce larger shear deformation levels under the same shear stress in the *x*–*y* plane than in *x*–*z* and *y*–*z* planes.

Table 3.3 The determined mechanical properties of the studied ECS fabrics in 2D and 3D scales.

Group	**Sections**	**Sample Code**	E_x **(MPa)**	E_y **(MPa)**	E_z **(MPa)**	v_{xy}	v_{xz}	v_{yz}	G_{xy} **(MPa)**	G_{xz} **(MPa)**	G_{yz} **(MPa)**
	Knee	S1	0.24	0.20	0.08	0.26	0.24	0.26	0.11	0.05	0.04
A	Calf	S2	0.35	0.30	0.09	0.25	0.24	0.25	0.14	0.06	0.04
	Ankle	S3	0.45	0.35	0.10	0.23	0.23	0.22	0.17	0.08	0.05
	Knee	S4	0.40	0.14	0.05	0.25	0.27	0.27	0.12	0.02	0.01
B	Calf	S5	0.43	0.18	0.06	0.25	0.29	0.24	0.12	0.03	0.01
	Ankle	S6	0.48	0.27	0.05	0.26	0.26	0.26	0.15	0.05	0.02
	Knee	S7	0.35	0.14	0.03	0.24	0.29	0.30	0.11	0.03	0.01
C	Calf	S8	0.49	0.22	0.04	0.25	0.24	0.25	0.13	0.03	0.02
	Ankle	S9	0.60	0.22	0.04	0.25	0.25	0.27	0.21	0.05	0.02

* All above listed columns are the determined 3D mechanical properties those were applied to the FEM of ECS fabrics. The shaded columns are the determined 2D mechanical properties those were applied to the FEM of ECS fabrics.

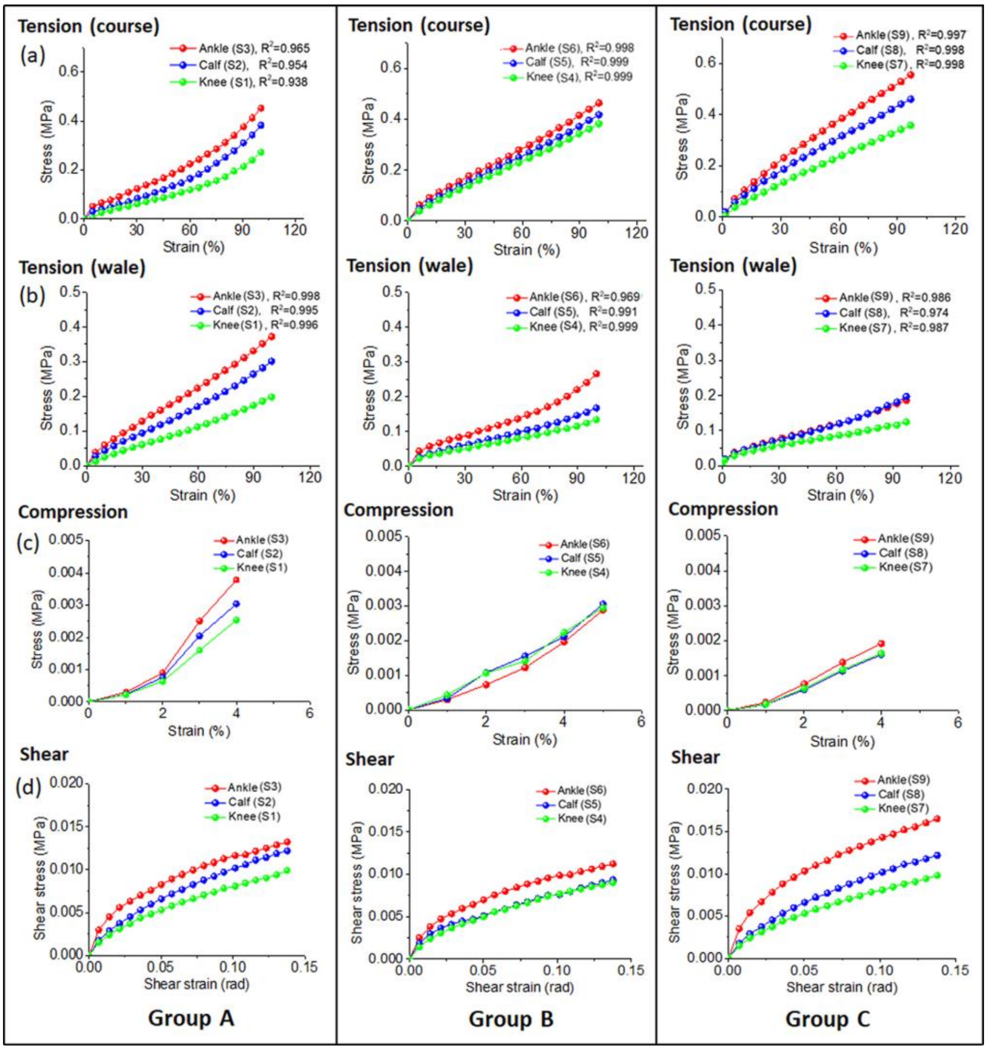

Figure 3.8 The determined stress-strain curves of the studied ECS fabrics by experimental tests in terms of (a) tension in course direction, (b) tension in wale direction, (c) compression at thickness direction, and (d) shearing at course-wale plane.

3.3.2 Simulated Interface Pressure by ECSs with 2D and 3D Properties

Figure 3.9 displays the simulated (using 2D and 3D material mechanical properties) interface pressure values between the ECS fabrics and wooden leg models for all three studied groups of ECS fabrics. In general, the gradient profiles of the simulated pressure values along the leg models decrease gradually. Specifically, the highest pressure was exerted at the ankle, decreasing gradually toward the knee; this profile is consistent with the basic design principle for ECSs in medical treatment. Both 2D and

3D material properties could be used to reveal the pressure gradient profiles of the studied ECS fabrics. Overall, the pressure values simulated for the ECS fabrics with the 2D material mechanical properties were greater than those simulated for the ECS fabrics with the 3D material mechanical properties by approximately 9.2%. For example, the simulated interface pressure between the WL-I leg model and the Group C ECS fabrics with the 2D material mechanical properties was 25.6 mmHg at the ankle, 20.2 mmHg at the calf, and 14.7 mmHg at the knee, and that obtained for the ECS fabrics with the 3D material mechanical properties were 22.3 mmHg at the ankle, 16.0 mmHg at the calf, and 9.3 mmHg at the knee. These ECS fabrics could thus be assigned to the Class-II pressure category (medium) for treatment of moderate venous disorders such as varicose veins and leg swelling in application (Jungbeck, et al. 1997; Liu, et al. 2018). To further verify the effectiveness of the use of 2D and 3D material mechanical properties in pressure performance prediction, a series of experiments were conducted to compare the simulated and the experimental data as described in Chapter 3.3.3.

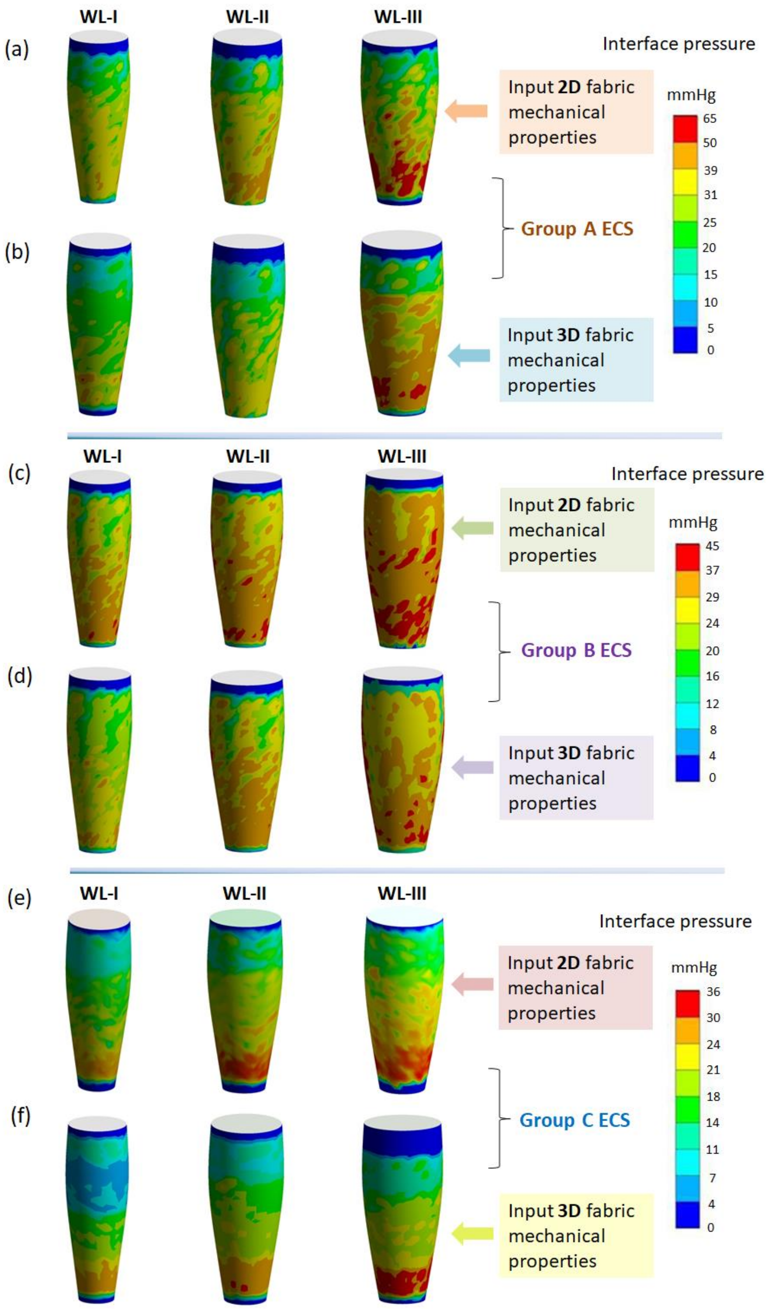

Figure 3.9 The simulated interface pressure profiles applied by the different groups of the studied ECSs when their 2D and 3D material mechanical properties were applied, respectively.

Table 3.4 shows the comparison results of meshing independence examination among different meshing sizes (4, 6, and 8 mm per element) tested in the developed FEM. All three mesh densities of the FE models produced the similar levels of the simulated interface pressure, indicating that these meshing densities are high enough to enable meshing-numerical solutions. Relatively, our applied meshing size of 6 mm per element presented the highest meshing quality value of 0.842, that is, the developed FEM can effectively reflect pressure profiles exerted by the studied ECSs.

Table 3.4 Results of meshing independence examination.

Meshing size	Element number	Meshing quality	Interface pressure (mmHg)		
			Ankle	Calf	Knee
8 mm	18207	0.836	28.4±4.0	20.9±1.6	12.0±4.2
6 mm	46507	0.842	27.0±2.8	20.0±1.3	11.1±3.4
4 mm	95150	0.836	27.2±2.6	19.9±1.5	11.0±3.5

3.3.3 Validated the Built FE ECS-Rleg Models

Figure 3.10 illustrates the comparison between the pressure values simulated using the 2D or 3D material mechanical properties with the experimental pressure values. The results indicated that the pressure values simulated for the ECS fabrics with the 3D material mechanical properties were in closer agreements with the experimental pressure values in general, especially for the Group C of ECS samples applied to the WL-I, WL-II, and WL-III leg models.

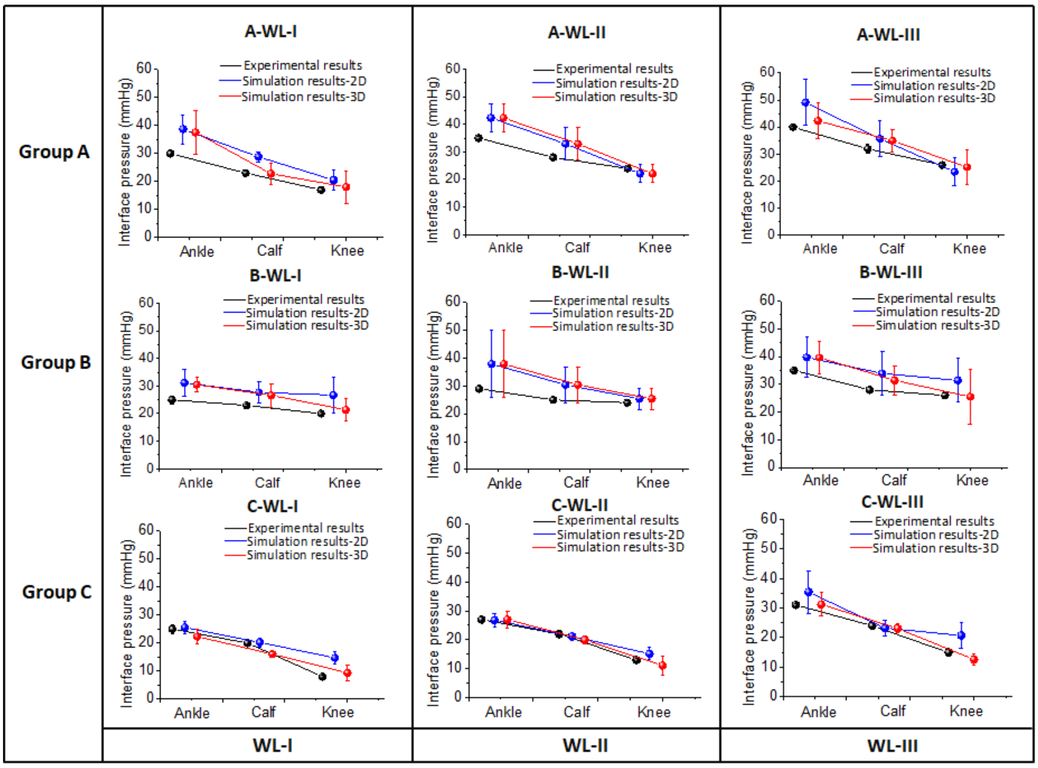

Figure 3.10 Comparison between the simulated and measured interface pressures when ECSs materials (groups A, B, and C) were applied with 2D and 3D mechanical properties to the different sized wooden leg models.

Table 3.5 presents the differences between the simulated and measured interface pressure values. When the ECS fabrics with 2D material mechanical properties were applied to the WL-I, WL-II, and WL-III models, the DROs between the simulated and measured pressure values were approximately 17.2%, 21.2%, and 16.7%, respectively, while the corresponding DROs were reduced to 9.4%, 11.9%, and 9.4% when ECSs fabrics with 3D mechanical properties were applied to the same groups of leg models. That is, the average DROs between the simulated and measured pressure values decreased from approximately 18.2% for the ECS fabrics with the 2D material mechanical properties to 10.4% for the ECS fabrics with the 3D material mechanical properties (Fig.3.11). Equivalently, the simulation precision increased by approximately 44.6%.

Table 3.5 Details on DROs of the simulated and the measured pressure values by using 2D and 3D material mechanical properties of ECS fabrics, respectively.

ECSs		**Simulated pressures by ECSs with use of 2D or 3D material mechanical properties, respectively**				**Measured interface pressure exerted by ECSs**
		2D		**3D**		**Experimental test**
		Simulated pressure (mmHg) (pressure gradient %)*	DROs (%)	Simulated pressure (mmHg)	DROs (%)	Measured pressure (mmHg) (pressure gradient %)*
Group A-WL-I	**Ankle**	38.7±5.2 (100%)	29.0	37.5±7.7 (100%)	25.0	30±0.7 (100%)
	Calf	28.8±1.8 (74.5%)	25.2	22.8±3.8 (60.8%)	0.9	23±0.5 (77%)
	Knee	20.5±3.6 (53.0%)	20.6	18.0±5.9 (48.0%)	5.9	17±0.7 (57%)
Group A-WL-II	**Ankle**	42.3±5.2 (100%)	20.9	42.3±5.0 (100%)	20.9	35±0.5 (100%)
	Calf	32.9±5.9 (77.8%)	17.5	30.2±4.2 (71.4%)	7.9	28±0.7 (80%)
	Knee	22.1±3.3 (52.2%)	7.9	25.2±4.2 (59.6%)	5.0	24±0.5 (69%)
Group A-WL-III	**Ankle**	49.1±8.5 (100%)	22.8	42.8±6.6 (100%)	7.0	40±0.4 (100%)
	Calf	35.7±6.6 (72.7%)	11.6	35.0±4.1 (81.8%)	9.4	32±1.6 (80%)
	Knee	23.5±5.1 (47.9%)	9.6	25.2±6.4 (58.9%)	3.1	26±0.6 (65%)
Group B-WL-I	**Ankle**	31.1±4.8 (100%)	24.4	30.5±2.6 (100%)	22.0	25±1.4 (100%)
	Calf	27.7±3.9 (89.1%)	20.4	26.6±4.2 (87.2%)	15.7	23±0.4 (92%)
	Knee	26.7±6.4 (85.9%)	33.5	21.4±4.2 (70.2%)	7.0	20±0.8 (80%)
Group B-WL-II	**Ankle**	37.9±12.1 (100%)	30.7	33.9±4.6 (100%)	16.9	29±0.9 (100%)
	Calf	30.4±6.4 (80.2%)	21.6	29.6±4.7 (87.3%)	18.4	25±0.7 (86%)
	Knee	25.4±3.9 (67.0%)	5.8	24.1±5.6 (71.1%)	0.4	24±0.5 (83%)
Group B-WL-III	**Ankle**	39.7±7.2 (100%)	13.4	39.6±5.7 (100%)	13.1	35±0.5 (100%)

	Calf	33.9±7.9 (85.4%)	21.1	31.4±5.2 (79.3%)	12.1	28±0.8 (80%)
	Knee	31.4±7.9 (79.1%)	20.8	25.5±9.9 (64.4%)	1.9	26±0.7 (74%)
Group C-WL-I	**Ankle**	25.6±2.2 (100%)	2.4	22.3±2.4 (100%)	10.8	25±1.6 (100%)
	Calf	20.2±1.6 (78.9%)	1.0	16.0±1.0 (71.7%)	20.0	20±1.0 (80%)
	Knee	14.7±2.1 (57.4%)	83.8	9.3±2.9 (41.7%)	16.3	8±0.5 (32%)
Group C-WL-II	**Ankle**	26.8±2.2 (100%)	0.7	27.0±2.8 (100%)	0	27±1.0 (100%)
	Calf	21.2±0.9 (81.3%)	3.6	20.0±1.3 (74.1%)	9.1	22±0.9 (82%)
	Knee	15.2±2.1 (56.7%)	16.9	11.1±3.4 (41.1%)	14.6	13±0.4 (48%)
Group C-WL-III	**Ankle**	35.4±7.2 (100%)	14.2	31.2±3.9 (100%)	0.6	31±0.5 (100%)
	Calf	23.2±3.6 (65.5%)	3.3	23.1±1.5 (74.0%)	3.8	24±1.0 (77%)
	Knee	20.7±4.3 (58.5%)	38.0	13.6±2.0 (43.6%)	9.3	15±0.8 (48%)

* Pressure gradient (%) = pressure value divided by pressure value at the ankle region.

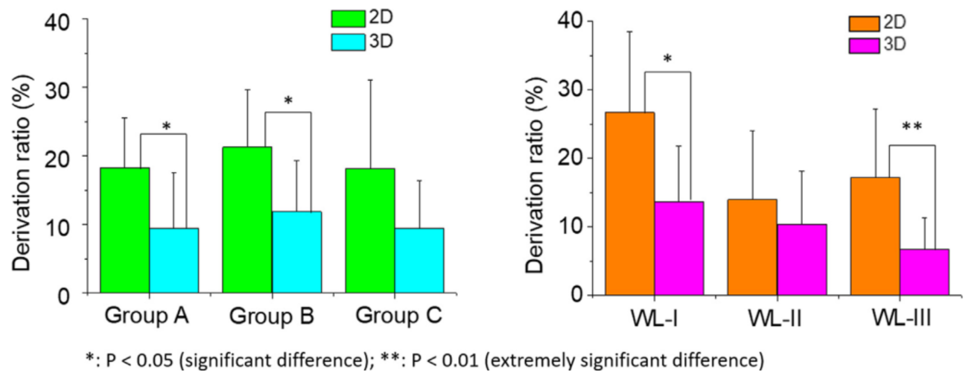

Figure 3.11 Comparison on the DROs (%) between the use of 2D and 3D material mechanical properties when being applied with three different groups of ECS samples on three different sizes of leg models.

The ECS–leg interaction system is in a 3D stress state if the fabric stresses along the wale, course, and thickness directions are all nonzero. Previous research assumed that ECS fabric are orthotropic laminas in a plane stress state (Zhou, et al. 2010), without considering material mechanical properties along the thickness directions, which could lead to overestimations or underestimations in the predicted pressure values. The results of the present study reveal that the use of ECS fabrics with 3D material mechanical properties could more realistically predict actual conditions, thus leading to FEM-based pressure simulation results to be more consistent with actual pressure values. To further analyse the effects of changing the material mechanical properties on pressure prediction performance, we used wooden leg models with a round cross section and a rigid surface; this enabled us to focus on the material properties and their variations in the simulations while ignoring other factors influencing pressure values, such as irregular leg surface curvatures and heterogeneous tissue stiffness. In Chapter 5, we would include more complex contact conditions such as biologic leg models with uneven surfaces and varying tissue properties to estimate the effects of modeled ECS material properties on the corresponding pressure prediction performance.

E, *v*, and *G* are elastic moduli that are commonly used to indicate the mechanical properties of compression fabrics in FEM through integrating 2D orthotropic analysis theories and Instron or Kawabata biaxial tensile and shearing testing. In one of our previous studies (Liu, et al. 2006), the measured *E* values of 1×1 laid-in knitted ECS fabrics along the course direction were 0.278, 0.214, and 0.150 MPa at the ankle, calf, and knee, respectively, and along the wale direction, the values were 0.197, 0.150, and 0.103 MPa at the ankle, calf, and knee, respectively. Its results indicated that with use of these 2D material properties of ECS fabric in the FEM, the DROs between the simulated and measured interface pressure values at the ankle, calf, and knee presented approximately 44.0%, 16.5%, and 20.4%, respectively. Through optimization, our recent FE study (Ye, et al. 2020) using the similar structured knitted ECS fabrics with 2D mechanical properties reduced these DROs to approximately 15.5%, 15.2%, and 18.1% at the ankle, calf, and knee, respectively. However, these error ranges remain above 15%. In contrast to methods as aforementioned, this new approach proposed herein applies mechanical properties derived along the thickness direction (E_z, v_{xz}, v_{yz}, G_{xz}, and G_{yz}) in addition to those derived along the wale and course directions (E_x, E_y, v_{xy}, and G_{xy}) for pressure simulation through FEM, which reduced the DROs to be 10.4% generally, implying that the use of material thickness properties can affect the simulated normal pressure magnitudes exerted by ECS fabrics on the applied contacted body (leg models).

3.4 Summary

This Chapter developed a new approach for determining the mechanical properties of ECS fabrics in 2D and 3D stress planes based on the developed analytical model. Through the integrated Airy stress function and cantilever beam bending testing, the shear properties of ECS fabrics in the course–thickness and wale–thickness planes were determined. On the basis of orthotropic theory, FEM, and experimental testing, nine critical mechanical properties were obtained, including three-dimensional Young's moduli, Poisson's ratios, and shear moduli along the wale, course, and thickness directions of ECS fabrics, and their effects on pressure magnitudes (dose) and distributions were simulated. The contribution of this chapter is the provision of an operable pressure prediction method, which can facilitate the design of ECSs with favorable mechanical properties and the determination of the elastic moduli of compression materials; this can thus enhance the understanding of the mechanisms underlying the interactions between elastic compression textiles and the applied bodies. The developed methods would be applied to determine the mechanical properties of the ECS fabrics in the follow Chapters, and provided a guidance to optimize the mechanical properties of the ECS fabrics in the FE ECS-leg system.

CHAPTGER 4 GEOMETRIC MODELLING OF SUBJECT-SPECIFIC LOWER LIMBS AND ECSs

4.1 Introduction

In Chapter 3, the FE ECS-Rleg model has been constructed. However, FE-Rleg model cannot reflect the internal biomechanical behaviors of the lower limb (e.g., tissue stress transmission and venous hemodynamics) exerted by the ECS fabrics. To detect the internal mechanical performances, the subject-specific ECS-leg models were constructed in this Chapter. The determined mechanical properties of the ECS fabrics in Chapter 3 provided the mechanical parameters to determine the mechanical behaviors of the ECS fabrics in the 3D FE ECS-leg models in Chapter 4.

The reverse engineering technology was used to reconstruct the lower limb (Liu, et al. 2006) with the process of reconstruction the geometry model based on the extracted geometry properties via MRI images (Geng, et al. 2021). However, among the existing studies, few studies detected the differences of the tissue stresses induced by the ECS fabrics among multi-subjects by using FE methods.

Thus, in this chapter, three subject-specific lower limb geometry models with corresponding ECS fabrics geometry models were reconstructed based on MRI images via the reverse engineering technology and the constructed geometry models. The outcomes were further input to the FE simulation in following Chapters for numerical simulation of the mechanical performances in the ECS-leg system.

4.2 Methods

4.2.1 Geometric Modelling the Designed ECSs

The geometry models of the ECS samples were constructed based on the actual tailor-made ECS tubular dimension by using Ansys workbench design modeler (v19.2, ANSYS, Pennsylvania, Pittsburgh, USA) as shown in Fig. 4.2. The purposes were to analyze the interactions among lower limbs and resultant skin pressure, tissue stress, and their mechanical transmission behaviors within lower limb tissues. Moderate or higher pressure levels (20-40mmHg) provided a moderate or greater pressure dosages for the prevention or treatment of CVI or the reduction of postoperative pain in the primary varicose treatment, and lower pressure levels provided the lower pressure dosage (10-18 mmHg) for the relief of the leg fatigue, tiredness, and heaviness (Elderman, et al. 2014).

In this study, two classes ECSs were applied (Class-I and Class-III) to provide both higher and lower pressures. Six tailor-made footless ECS samples knitted by 1x1 laid-in loop structures with various physical and mechanical properties were fabricated by different yarn combinations and machinery settings to regulate the fabric dimensions and pressure dose. The ECS samples were prepared in S (small) size to XXXL (plus large) size for each studied class level through the adjustment of combinations of ground yarns and inlay yarn materials with different specifications. Polyamide double-covered Lycra yarns with the linear density of 40D/40D/40D were used as the ground threads to provide the substrate fabric thickness and basic dimensional stability. Polyamide-double covered Lycra yarns with the linear densities of 210D/40D/40D and 420D/40D/40D were used as the inlay threads to regulate fabric mechanical tensile properties for achieving lower (Class-I) and higher (Class-III) pressure levels (Shi, et al. 2023), respectively. Through adjusting circumferential dimensions, fabric tension and loop densities of the ankle, calf, and knee segments of the ECS tubulars, the developed ECSs were proposed to produce gradient interface pressures at lower limb surface where the higher pressure was exerted at ankle and gradually decreased up to the knee, to fulfill gradient compression design principle according to RAL-GZ 387/1 standard.

4.2.2 Geometric Modelling of Subject-Specific Lower Limbs

MRI Imaging Collection of Lower Limbs

MRI is a medical imaging technique, which has been applied to form digital images of the anatomy and the physiological processes of the body based on a strong magnetic field via power magnets (McRobbie, et al. 2007). MRI is usually applied in the clinics or hospitals for the medical diagnosis, such as detection and diagnosis of heart disease, cerebrovascular accidents and vascular disease, detective and diagnosis of organ disease in the chest and abdominal cavity, and diagnosis and evaluation, tracking tumor conditions and functional obstacles. The MRI is a safety technology compared with CT scanning, as no radiation occurred during the MRI (Watson, et al. 2015).

To detect the mechanical mechanisms among different human groups, three subjects have been recruited to attend the MRI scanning. A series of MRI slices were extracted from the right lower limbs from these three healthy subjects with different ages and genders, including two female subjects (subject 1, aged 40 and subject 2, 55 years old), and one male subject (subject 3, 50 years old) (Table 4.1). An increment of 1.0 mm using a 0.2 T Artoscan MRI system (Esaote S.p.A., Genova, Italy). The imaging protocol was a spinecho sequence chosen to provide clear anatomical delineation (time of repetition (TR) = 4390 ms, echo time (TE) = 80 ms). Before MRI scanning, every subject was invited to measure the lower limb circumference to determine the proper ECS sizes and sign the safety consent form to ensure the subjects without metal materials in the body such as pacemaker and denture and without pregnancy period. Every subject lied on the MRI scanning bed and moved into the scanner. The duration of the whole scanning for each subject was approximately one hour. The MRI scanning process was divided into three steps, i.e., step-1 was scanning the lower limb from the knee to below ankle regions, step-2 was scanning the below knee with wearing the Class-I ECS fabrics, and step-3 was scanning the below knee with wearing the Class-III ECS fabrics. After the MRI scanning, three subjects rested for half an hour and were asked whether appeared the uncomfortable feeling during the scanning to promise that every subject did not feel uncomfortable before leaving.

Table 4.1 Characteristics of the studied three subjects.

Subject	Age	Height (cm)	Weight (kg)	BMI (kg/m^2)	Leg girth/length (cm)			
					B (Ankle)	B1 (Brachial)	C (Calf)	D (Knee)
1	40	160	55	21.5	16.8/7	20.6/13	29.9/6	27/4
2	55	160	55	21.5	19.4/6	25.8/12	32.8/5	29.7/5
3	50	170	75	26.0	22.7/8	32.0/16	39.1/6	34.5/5

Reconstruction of Lower Limbs Geometric Models

The 3D geometric models of the subjects' lower limbs were reconstructed using Mimics software (v20.0, Materialise, Hungary) based on the extracted multiple cross-sectional MRI slices in the masks (Fig. 4.1). The biocomponents (skin, soft tissue, and bones) of each lower limb were segmented through the custom thresholds' settings and were reconstructed to form 3D leg geometric models for each studied subject, which were further imported to the 3-matic software (v20.0, Materialise, Hungary) and Ansys workbench space claim (v.19.2, ANSYS, Pennsylvania, Pittsburgh, USA) to eliminate the stitch, gap, and missing faces, and repair gaps between faces to obtain the optimized 3D leg geometric models for FE analysis in Chapter 5 (Fig. 5.2).

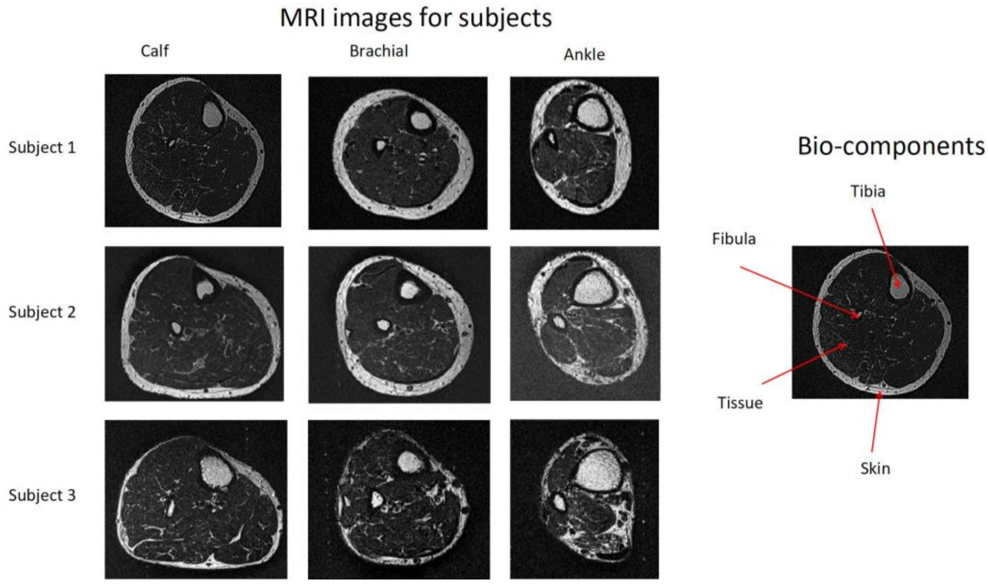

Figure 4.1 The collected MRI images in different heights for three subject

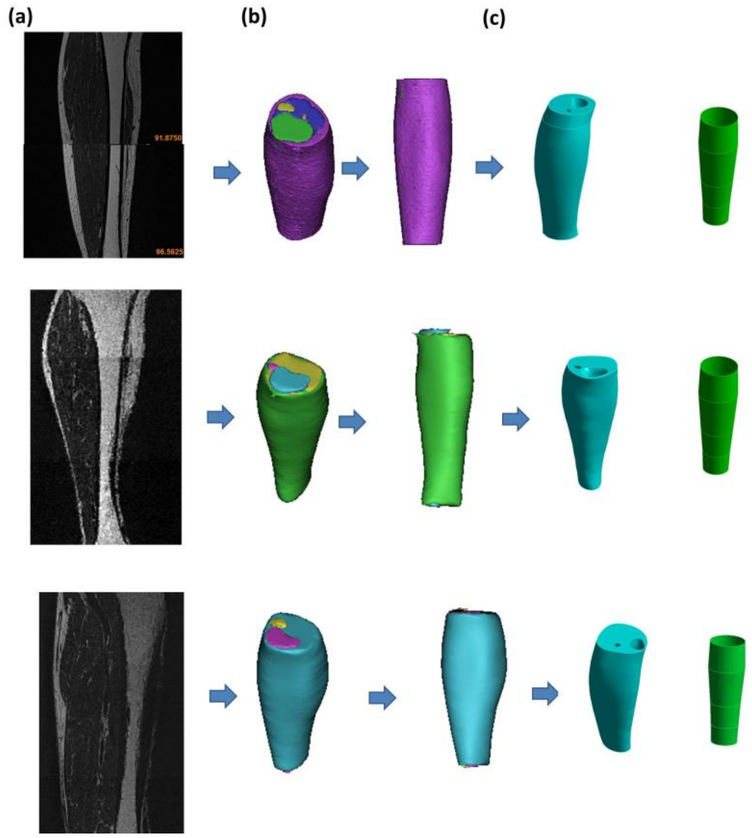

Figure 4.2 (a) longitudinal views and the developed geometric models for (b) lower limbs and (c) footless ECS tubes.

The geometric structures of the peroneal veins, small saphenous veins, and great saphenous veins of the lower limbs were reconstructed from the axial images via MRI scanning (Fig.4.1). The axial MRI images were corresponding with the cross-sectional plane, which can be extracted the bio-components of the lower limb. The spatial position of the veins was based on the MRI images, and the cross-sections of the veins were processed via Matlab software ginput function with smooth treatment as a circle since the fewer pixels induced irregular vein surface to determine the coordinate. The 3D venous geometry model was reconstructed by using Ansys workbench design modeler via sweep function based on the regular cross-section of the veins.

The Geometric Properties of the Reconstructed Lower Limbs and ECSs

The height of the reconstruction lower leg geometry models was approximately 30 cm. The circumferences of the subject 1's right lower limb were approximate 21.8 cm, 29.1 cm, 34.7 cm, and 31.4 cm at the ankle, brachial, calf, and knee sections, respectively. The circumferences of the subject 2's right lower limb were about 19.4 cm, 25.8 cm, 32.8 cm, and 29.7 cm at the ankle, brachial, calf, and knee sections, respectively. And, the circumferences of the subject 3's lower limb were about 25.1 cm, 31.0 cm, 38.9 cm, and 34.6 cm at the ankle, brachial, calf, and knee sections, respectively. Our designed ECS fabrics widths were measured by the Vernier calipers. It can be seen that our designed ECS circumferences were 15.8 cm, 17.1 cm, and 22.1 cm at ankle, brachial, and calf for S size, respectively. For the XXL size, the ECS circumferences were 19.0 cm, 21.1 cm, and 26.6 cm at ankle, brachial, and calf, respectively (Table 4.2). Based on our empirical experience in the previous large-scale wear trials, ECSs with a M size were applied on the subjects 1 and 2, and ECSs with an XXL size were applied on subject 3 in the FE ECS-leg modeling in the next Chapter 5 to estimate their pressure performances.

Table 4.2 Our designed sizes for ECS samples.

Circumference (cm)	S	M	L	XL	XXL	Length (cm)
Ankle	15.8	16.6	17.4	18.2	19	6
Brachial	17.1	17.6	19.2	20.2	21.1	5
Calf	22.1	23.3	24.4	25.5	26.6	8

4.3 Summary

In this chapter, the geometry models of the ECS samples were constructed by using Ansys workbench design modeler (CAD system) for the three studied subjects. The geometry models of the lower limbs with biocomponents (skin, muscle, fibula, tibia, deep veins, and superficial veins) were reconstructed by using reverse engineering technology based on MRI images. The constructed subject-specific ECS-leg geometry models were further input to Ansys workbench environment for numerical simulation of the biomechanical behaviors (interface pressure, deformation, stress transmission, and venous velocity, etc) of ECSs and soft tissues when ECS interacted with the lower limbs in Chapters 5 and 6.

CHAPTER 5 FINITE ELEMENT SIMULATION OF SUBJECT-SPECIFIC LOWER LIMBS AND THE DESIGNED ECSs

5.1 Introduction

ECS, as one type of unique compression textiles, has higher requirements for pressure control (i.e., pressure level and gradient distribution) along the lower limb in CVI treatment (Liu, et al. 2017; Lattimer, et al. 2016). Appropriate pressure doses delivered by ECS not only influence pressure exerted on the lower limb tissue surface but also the stress transmission efficiency within soft tissue system, even venous hemodynamics. To comprehend the pressure dose design and pressure transmission features by ECSs, this study proposed a new approach to characterize and visualize biomechanical performance of ECSs with distinct pressure levels and gradient distributions when they were applied to different targeted subjects' lower bodies. Mixed FEM and experimental measurements have been performed to build a systematical study framework which integrates materials and pressure testing, tissue stress simulation, pressure-curvatures analysis, and experimental validation. The outcomes further facilitate the understanding of biomechanical function of compression textiles, thus building a new prospective on compression textile materials design for various end users in physiotherapy.

5.2 Methods

In Chapter 3, a FE ECS-Rleg model has been constructed and simulated, however, the FE-Rleg model cannot reflect the biomechanical behaviors in the ECS-leg system, since the mechanical properties and geometry properties are different between the rigid leg models and soft biologic legs, and the cross sections of the rigid leg models are regular circles, while the cross sections of soft legs are commonly irregular. To determine the interaction mechanisms between the ECS fabrics and the biologic lower limbs, in this Chapter, the FE ECS-leg model were constructed based on the reconstructed subject-special geometric models in Chapter 4. Class-I-ECS provided the lower pressure level for the relief of the leg fatigue, tiredness, and heaviness. Correspondingly, Class-III ECSs provided a higher-pressure dosage for treatment of more serious symptoms of CVI (pain and non-reversible skin changes). Thus, Class-I and Class-III ECS fabrics were simulated and analyzed in our studies to examine the effects of different pressure magnitudes on the soft tissues of the biologic lower limbs.

5.2.1 Contact Analysis

Laplace's law is commonly used to analyze relationships between the elastic material and its produced interface pressure at the applied body (Basford, et al. 2002), which can be expressed as follow,

$$P = \frac{T}{R} \tag{5.1}$$

where P is the interface pressure produced between the ECS fabric and the lower limb, T is the tension force of the ECS fabric, and R denotes the radius of the applied body (lower limb). The recent optimized Laplace's law (Eq. 5.2) involves more physical-mechanical properties of ECS fabric such as Young's modulus (E), ECS fabric strain (ε) and thickness (h) to further reflect effects of elastic fabric layer on interface pressure magnitudes as below,

$$P = \frac{E\varepsilon h}{R} \tag{5.2}$$

However, the irregular leg shape around its cross-section, uneven tissue stiffnesses, and heterogeneous biostructures of the applied lower limb remain ignored. To address these limitations, the FEM built in this study proposed to present the interaction between the lower limb and ECS three dimensionally with consideration of more ECS fabric properties (Young's modulus, Poisson's ratio, shear modulus, thickness, and mass densities), lower limb biostructures (skin, soft tissue, bones), tissue stiffnesses, and cross-sectional curvatures.

The frictional contact interface where Augmented Lagrange equation (ALE) (Eq. 5.3) was adopted to refine the contact condition of the two interacted bodies (the lower limb and the ECS) to prevent the penetration of the ECS fabric layer to the lower limb tissues. The Eq. 5.3 is presented as follows,

$$F_{normal} = k_{normal} x_{normal} + \lambda_1 \tag{5.3}$$

where F_{normal}, k_{normal} and x_{normal} are the contact force, contact stiffness, and contact displacement along normal direction, respectively, and λ_1 is the Lagrange factor. Sliding resistance is proportional to the coefficient of friction. Free separation between the ECS fabric layer and the lower limb is unimpeded.

5.2.2 Meshing Construction

The mesh was applied to discretize the constructed geometry model for further FE simulation. Thus, the built geometry models of ECSs and leg components in Chapter 4 were further imported to Ansys workbench software (v19.2, ANSYS, Pennsylvania, Pittsburgh, USA) for meshing and setting of boundary conditions. The explicit LS-Dyna solver was applied to analyze interaction between the ECS fabrics and lower limb based on the dynamic equation (Eq. 5.4) via central difference method (Gravouil, et al. 2009),

$$M\ddot{u}^n = P^n - F^n + H^n$$

(5.4)

where M is the diagonal mass matrix, $\ddot{u}^n$ is the nodal acceleration component, P is the load, F is the stress component, and H is the damped hourglass, where the damped hourglass was applied to reduce hourglass energy in the explicit dynamic model (hourglass energy means zero energy mode of deformation that produce no stress) to achieve the simulation accuracy.

To examine meshing independence of the selected meshing sizes in the built FE model, three different meshing sizes of 7 mm, 6 mm, 5 mm, 4 mm, and 3 mm for ECS fabrics and the meshing sizes of 8 mm, 7 mm, 6 mm, 5 mm, and 4 mm for soft tissues were applied, respectively, in subject 1’s ECS-leg system, thus keeping meshing quantity between skin surface and ECS fabrics are similar. The comparison meshing quality were shown in Table 5.1.

The results indicated that the meshing independent has been highly achieved by the determined meshing quality and corresponding simulated pressure values for predicting interactive mechanical behaviors between ECS and lower limb. FE ECS model with meshing size of 5 mm and FE lower limb model with meshing size of 6 mm achieved the best meshing quality of 0.838 and 0.839 for the Class-I FE ECS-leg system and Class-III FE ECS-leg system, respectively. Therefore, these meshing sizes have been applied in the FEM of ECS-lower limb system for achieving a preferable simulation effect where similar meshing account (i.e., element number) of the slave (ECS model) and the master (lower limb model) were applied.

Table 5.1 The meshing quality under difference meshing size.

Meshing size	**Class I ECS-Leg model Element number**	**Meshing quality**	**Class III ECS-Leg model Element number**	**Meshing quality**
7 mm (ECS model), 8 mm (leg model)	88635 (approximately 1200 at the contact surface)	0.837	88623 (approximately 1200 at the contact surface)	0.837
6 mm (ECS model), 7mm (leg model)	110302 (approximately 1400 at the contact surface)	0.837	110388 (approximately 1400 at the contact surface)	0.837
5 mm (ECS model), 6 mm (leg model)	**123337** (approximately **1900** at the contact surface)	**0.838**	**123377** (approximately **1900** at the contact surface)	**0.839**
4 mm (ECS model), 5 mm (leg model)	235256 (approximately 2700 at the contact surface)	0.837	235212 (approximately 2700 at the contact surface)	0.837
3 mm (ECS model), 4 mm (leg model)	330207 (approximately 3900 at the contact surface)	0.835	330281 (approximately 3900 at the contact surface)	0.835

The constructed 3D lower limb tissue model and ECS shell model were meshed by using tetrahedrons elements and hexahedron elements, respectively. The produced nodes and elements were approximately 30,000 and 120,000 in total for the built FE models, respectively.

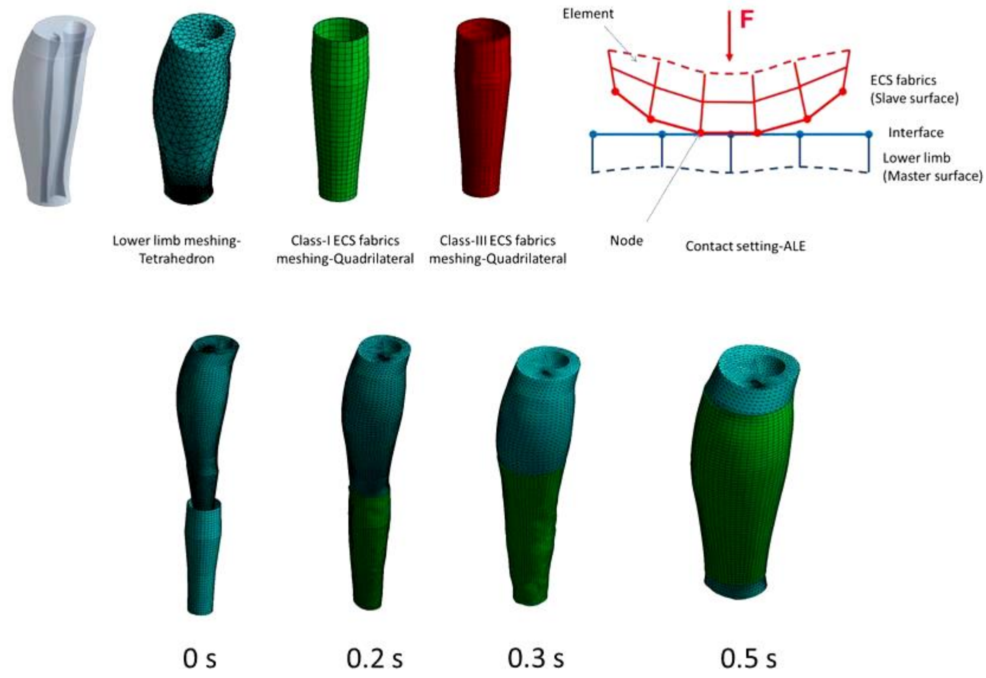

Figure 5.1 The meshing, contact condition, and wearing process applied in the built FEM of ECS-lower limb system.

5.2.3 Boundary Conditions

The tibia and fibula bones were fixed in the FE leg model while FE ECS tubular can freely move longitudinally along the lower limb from the ankle to the knee with a 340-mm displacement loading (Fig. 6.2) in accordance with wearing practice. The total degree of freedoms (DOF) of the proposed FE lower limb-ECS model was approximately 650,000 with six DOFs for every node. The boundary conditions restricted the six DOFs for the bones (tibia and fibula), and one DOF was set for the FE ECS model along its longitudinal direction for every node.

5.2.4 Determination of Mechanical Properties for ECS and Lower Limb Tissues

ECS Fabric Properties

In Chapter 3, an analytical model was proposed based on Hooke’s Law, which indicated the relationship among the stress, strain, and the elastic moduli (E, v, and G) of the ECS fabrics in a 3D scale. Based on our newly proposed analytical model and the ECS designed method in Chapter 3, ECS fabrics were assumed as a homogeneous, orthotropic, and linear elastic materials in the built FEM, where fabric Young's modulus (E), Poisson's ratios (v), shear modulus (G) were determined by using Instron 4411 uniaxial tension testing based on ASTM-D4964 standard and Kawabata (KES-FB3) pure shear testing assessment system, respectively, under a standard ISO13934-1:1999 testing condition (temperature of 20 ± 2°C, relative humidity of 65 ± 4%). The tension velocity and stretching ratio of the uniaxial tension testing was set at 100 mm/min and 120%, respectively, by using ECS fabric samples with a size of 7.5 × 7.5 mm^2. Shear angle set in shear testing was 8° by using fabric samples with a size of 200 × 200 mm^2. The thickness of the fabric was tested by using a Vernier caliper and mass densities of the fabric were determined by using an electronic balance (BP211D, Sartorius, Germany). The determined mechanical properties of ECS fabrics were listed in Table 5.2,

Table 5.2 The determined mechanical and physical properties of the studied ECS fabrics.

Pressure classification	Segment	E_x (MPa)	E_y (MPa)	**E_z (MPa)**	v	G_{xy} (MPa)	**G_{xz} (MPa)**	**G_{yz} (MPa)**	Mass densities (kg/m^3)	Thickness (mm)
Class-I Lower pressure level	Ankle (B)	0.47	0.33	**0.11**	0.19	0.13	**0.07**	**0.06**	357	0.68
	Brachial (B1)	0.44	0.22	**0.1**	0.20	0.11	**0.06**	**0.05**	325	0.70
	Calf (C)	0.33	0.18	**0.1**	0.20	0.10	**0.05**	**0.05**	302	0.69
	Knee (D)	0.22	0.13	**0.08**	0.21	0.09	**0.05**	**0.04**	253	0.69
Class-III Higher pressure level	Ankle (B)	0.75	0.50	**0.13**	0.16	0.13	**0.08**	**0.07**	409	0.66
	Brachial (B1)	0.74	0.39	**0.11**	0.24	0.13	**0.07**	**0.06**	375	0.69
	Calf (C)	0.73	0.35	**0.1**	0.22	0.12	**0.07**	**0.05**	348	0.70
	Knee	0.71	0.31	**0.1**	0.2	0.10	**0.06**	**0.05**	289	0.70

(D)		2		

*All above listed columns are the determined 3D mechanical properties those were applied to the FEM of ECS fabrics. The shaded columns are the determined 2D mechanical properties those were applied to the FEM of ECS fabrics.

Lower Limb Tissue Properties

(1) The referred tissue properties based on the available reference

In our developed FE ECS-leg model, the muscle stiffness was regarded as the major soft tissue stiffness to input into the FE ECS-leg model. Soft tissues of the lower limb was assumed as homogeneous, isotropic, incompressible material (Pierrat, et al 2018), which can be governed by a Neo-Hookean non-linear strain energy density function as shown in Eq. 5.5,

$$W = C_1(\bar{I}_1 - 3) + \frac{1}{D_1}(J-3)^2 \tag{5.5}$$

where W denotes the strain energy density, and the parameters C_1 and D_1 are the constitutive parameters of the Neo-Hookean model, which the values are approximately 5000 Pa and 1.4×10 $^{-7}$ Pa^{-1}, respectively (Liu, et al. 2020). I_1 is the first invariant of the Cauchy-Green deformation tensor and J is the volume ratio. C_1 and D_1 can be expressed under a linear elastic condition as follows,

$$C_1 = \frac{\mu}{2}; D_1 = \frac{\lambda}{2}$$

(5.6)

where μ and λ are shear modulus and bulk modulus, respectively. The endowed properties of ECS fabric layer and lower limb in FEM contributes to generating a more realistic simulation environment compared with the FE ECS-Rleg model in Chapter 3, thus analyzing the biomechanical transmission behaviors of skin pressure produced by ECS to lower limb tissues, thus exploring mechanisms of action of ECSs in compression therapy. The referred bio-tissue properties would be input into subject 1 ECS-leg model to detect the mechanisms in the ECS-leg system.

(2) The determined tissue properties based on our experimental tests

The muscle stiffness exists difference in different age groups, Hortobagyi et al. measured that the muscle stiffness was approximately 37.7 kPa for the older people, and 22.4 kPa for the younger people (Hortobagyi, et al. 2000). To further reduce the DROs of the simulated interface pressure in the ECS, the real tissue properties for subjects were determined by using a shear wave elastography (SWE) technology.

The SWE technology used the probe to emit safe ultrasound pulses (>20 kHz), causing tissue vibration at different positions and generating transverse SWE. The relationship between tissue stiffness and shear wave velocity can be expressed as

$$E=3\rho c^2 \tag{5.7}$$

where E is the Young's modulus of muscle group, ρ is density of the muscle group, and c is the shear wave velocity of the muscle group (Eby, et al. 2013). The relationship among the C_1, D_1, E, and v can be referred as Eq. 5.5 and Eq. 5.6, the value of v can be assumed as 0.5, as the muscle can be seen as incompressible material.

Correspondingly, three subjects were also invited to attend the SWE testing to determine the soft tissue stiffness at the ankle and calf sections along the anterior, posterior, medial, and lateral direction. During the measurement, the tip of the probe contacted the skin surface by using the coupling gel, and all of the subjects were required to place a stand posture. The average soft tissue stiffnesses of five different positions within a 4 mm diameter circle were recorded as the soft tissue stiffness for every direction around the lower limb (Fig. 5.2). Thus, the anterior, posterior, medial, and lateral direction of the soft tissue stiffnesses could be determined.

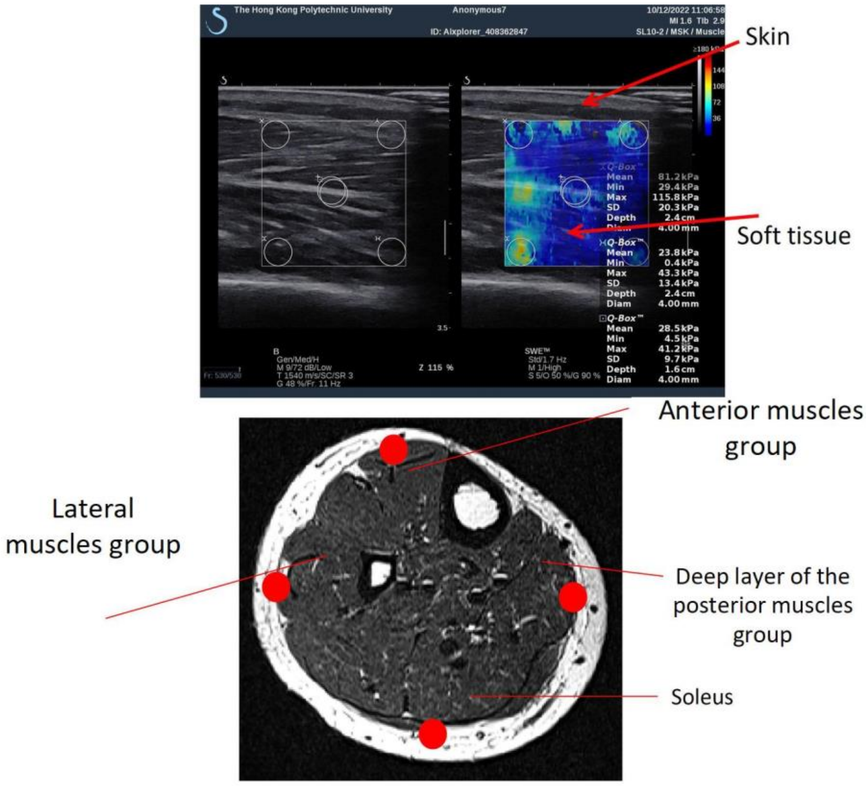

Figure 5.2 The SWE test on the determination of muscle stiffness and muscle distribution.

The determined mechanical properties of the soft tissues for all three subjects are shown in Table 5.3 (Fig. 5.2).

Table 5.3 The shear wave results of the tested soft tissues of the three studied subjects (kPa).

	Anterior	Posterior	Medial	Lateral
Subject 1	2.9±1.4	3.0±0.9	4.1±1.0	2.8±1.1
Subject 2	4.5±2.3	5.2±1.6	7.2±1.4	4.4±1.7
Subject 3	5.0±2.0	6.0±1.8	3.7±2.4	2.6±0.7

Anterior: Anterior muscles group
Posterior: Soleus
Medial: Deep layer of the posterior muscles group
Lateral: Lateral muscles group

It can be seen that the muscle stiffnesses at the anterior and lateral leg are generally less than those at the posterior and medial sections, and the muscle stiffness among the four directions around the lower limb are uneven. In this Chapter, to more realistically simulate interface pressure, the uneven tissue properties of these four different muscle groups for subject 2 were further input to FE model to attempt to reduce the DROs of the interface pressure simulation.

5.2.5 Validation of the Built FE ECS-leg System

Experimental measurements on interface pressure between ECS and lower limb were conducted by using an air-filled pneumatic pressure-sensing system (PicoPress, Microlab Elettronica Sas, Italy; pressure range: 0-189 mmHg; deviation within ± 1mmHg; sensing probe: 5 mm in a diameter and 0.2 mm in a thickness) (Liu, et al. 2019). The pressure testing was performed on the subject who attended the MRI scanning for FE leg model construction. The testing performed at twelve typical sites around the four directions (anterior, media, lateral, and posterior) and along the three height levels (ankle, calf, and knee) of the simulated subject’s lower limb. The simulated and experimental lower limb from the same subject was consistent in morphologies to maintain a comparable measurement status. The deviations, correlation analysis, and RMSE between the simulated and tested interface (skin) pressure were analyzed to verify the built subject-specific FE leg-ECS models, thus laying a foundation for biomechanical transmission analysis of ECS pressure when being applied to the user body.

5.3 Results and Discussion

The interface pressure doses delivered by the ECS fabrics are important to reflect the tissue mechanical performances and venous hemodynamics responses in the ECS-leg system. To optimize the simulation interface pressure in the FE ECS-leg system, the FE ECS-leg model has been constructed in this chapter based on our developed FE ECS-Rleg model in Chapter 3 and our reconstructed leg geometry model in Chapter 4. In this chapter, the model using both the referred and determined soft tissue stiffness to numerical simulate the mechanical behaviors in the ECS-leg system. Among them, the referred tissue properties were applied in subject 1 to develop a method to simulate the lower limb mechanical performances exerted by the ECS fabrics for analyzing the transmission mechanism within the tissue and tissue deformation. Follow this, the experimentally determined tissue properties were applied in all three subjects for further numerically simulating the interface pressure for optimizing the built ECS-leg system.

5.3.1 Simulated Skin Pressure Induced by ECSs on Subject-Specific Lower Limbs

First, this study took subject 1 as an example to examine the simulated pressure by Classes I and III ECSs on the lower limb with both referred tissue properties and our experimentally determined tissue properties. The aims were to compare the DROs of the interface pressure between the referred tissue properties and the determined tissue properties, as to find new solution to optimize the built FE ECS-leg system.

Second, this study further applied the experimentally determined tissue properties of subjects 2 and 3 in the built FE system to examine the simulated pressure using Classes I and III ECSs and compared the results.

5.3.1.1 *Simulated Skin Pressure based on the Referred Tissue Properties*

Fig. 5.3 displays the simulated skin pressure for subject 1 applied by Classes I and III ECS samples along and around the lower limb tissues based on the referred tissue properties (C_1 = 5000 Pa and D_1= 1.4×10^{-7}Pa^{-1}). It is observed that the higher pressure distributed at the ankle and gradually decreased up to the knee. The simulated average pressure at the ankle were approximate 23.8 and 35.3 mmHg for Classes I and III ECS samples, respectively; Correspondingly, the simulated average pressure at the brachial were about 21.0 and 31.5 mmHg for Classes I and III ECS samples, respectively, and about 14.4 and 26.2 mmHg at the calf for Classes I and III ECS samples, respectively. The pressure gradient ratios from the ankle (B), brachial (B1), to the calf (C) heights were 100 %, 88.2 %, and 60.5 % for Class-I ECS, and 100 %, 89.2 %, and 74.2 % for Class-III ECS fabrics, respectively. In general, the results showed that both simulated Classes I and III pressure agreed with the therapeutic pressure gradient profiles. The simulated ankle pressure for Class-I sample was slightly higher than the indicated range (18-21mmHg) by RAL-GZ 387/1 standard. This could be resulted from the usage of the referred tissue properties which could not reflect the uneven distributions of the subject-specific tissue stiffness properties, and the ignorance of mesostructures of the ECS knitted loops may also influence the stimulated pressure values.

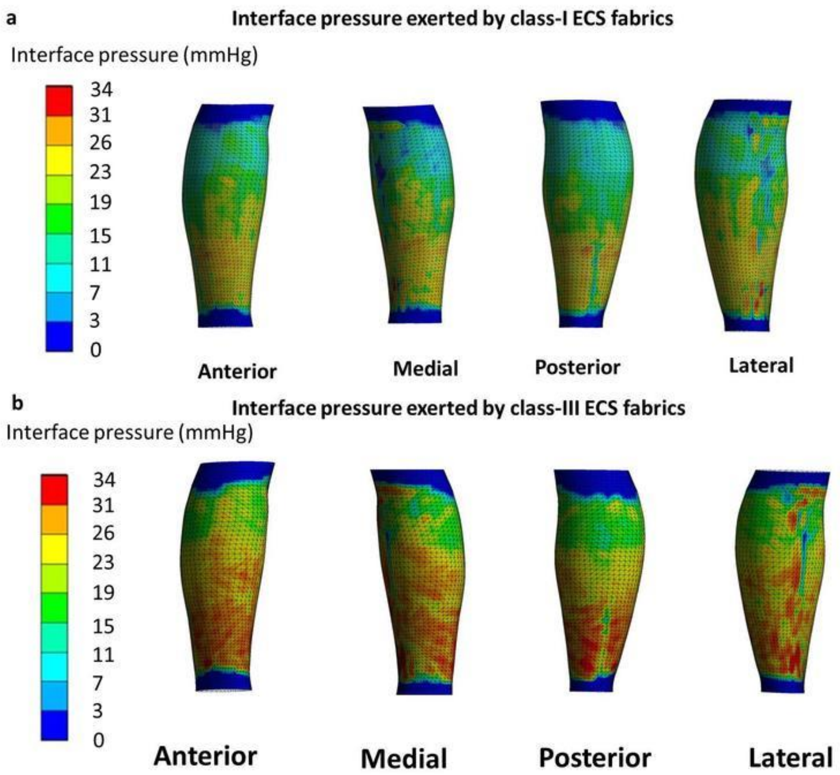

Figure 5.3 The simulated interface pressure exerted by Classes (a) I and (b) III ECSs samples for subject 1.

5.3.1.2 *Simulated Skin Pressure based on the Determined Tissue Properties*

To further optimize the FE ECS-leg system for an improved precision of pressure simulation, the experimentally determined tissue properties were input the built modeling system for the three studied subjects. The subject-specific tissue properties of the lower limbs were determined by applying SWE technology as presented in Section 5.2.4.

Fig. 5.4 displays the simulated skin pressure applied by Classes I and III ECS samples along and around the lower limb tissues for subject 1 based on the determined tissue properties of the subject 1's lower limb. It is observed that the higher pressure distributed at the ankle and gradually decreased up to the knee. The simulated average pressure at the ankle were approximate 22.6 and 34.2 mmHg for Classes I and III ECS samples, respectively; Correspondingly, the simulated average pressure at the brachial were about 20.0 and 30.0 mmHg for Classes I and III ECS samples, respectively, and about 13.7 and 24.7 mmHg at the calf for Classes I and III ECS samples, respectively. The pressure gradient ratios from the ankle (B), brachial (B1), to the calf (C) heights were 100 %, 88.2 %, and 60.6 % for Class-I ECS, and 100 %, 88.0 %, and 72.3 % for Class-III ECS fabrics, respectively. The pressure levels and gradients were all satisfied with RAL-GZ 387/1 standard. The simulated interface pressures by Class-III ECS satisfied with the pressure indicated by RAL-GZ 387/1 standard (Fig. 5.7) (i.e., 100% ankle pressure; 70%-100% of the ankle pressure at the brachial; 50%-70% (Class-I) or 50%-80% (Class-III) of the ankle pressure at the calf). The simulated interface pressure by Class-I ECS were slightly higher than the indicated pressure range by RAL-GZ 387/1 standard. In general, the simulated pressure values produced by the FE model with the input of the experimentally determined subject-specific tissue properties show more agreement with the measured pressure values than the simulated pressure values produced by the FE model with the input of the referred tissue properties.

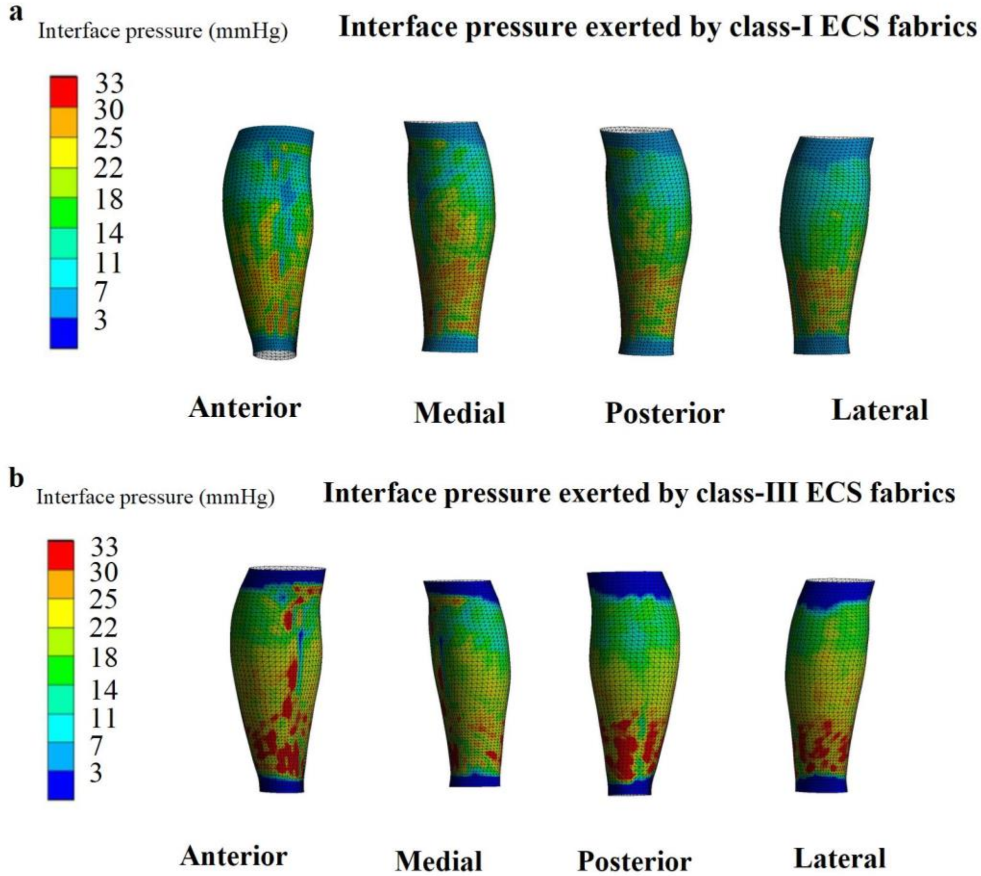

Figure 5.4 The simulated interface pressure exerted by Classes (a) I and (b) III ECSs samples for subject 1.

The simulated pressure profiles for subjects 2 and 3 were similar to subject 1, as shown in Fig.5.5 and Fig.5.6. The simulated interface pressure for subject 2 was approximately 22.7 mmHg, 21.0 mmHg, and 16.6 mmHg at the ankle, brachial, and calf section exerted by Class-I ECS, respectively, and 37.4 mmHg, and 33.3 mmHg, 25.5 mmHg at the ankle, brachial, and calf section exerted by Class-III ECS, respectively. The simulated interface pressure for subject 3 was approximately 25.3 mmHg, 21.1 mmHg, and 16.8 mmHg at the ankle, brachial, and calf section exerted by Class-I ECS, respectively, and 34.9 mmHg, and 25.4 mmHg, 24.5 mmHg at the ankle, brachial, and calf section exerted by Class-III ECS, respectively. In general, the simulated pressure gradient by ECSs with Classes I and III fulfilled the standardized pressure profiles as indicated by RAL-GZ 387/1 (Fig. 5.7) (i.e., 100% ankle pressure; 70%-100% of the ankle pressure at the brachial; 50%-70% (Class-I) or 50%-80% (Class-III) of the ankle pressure at the calf).

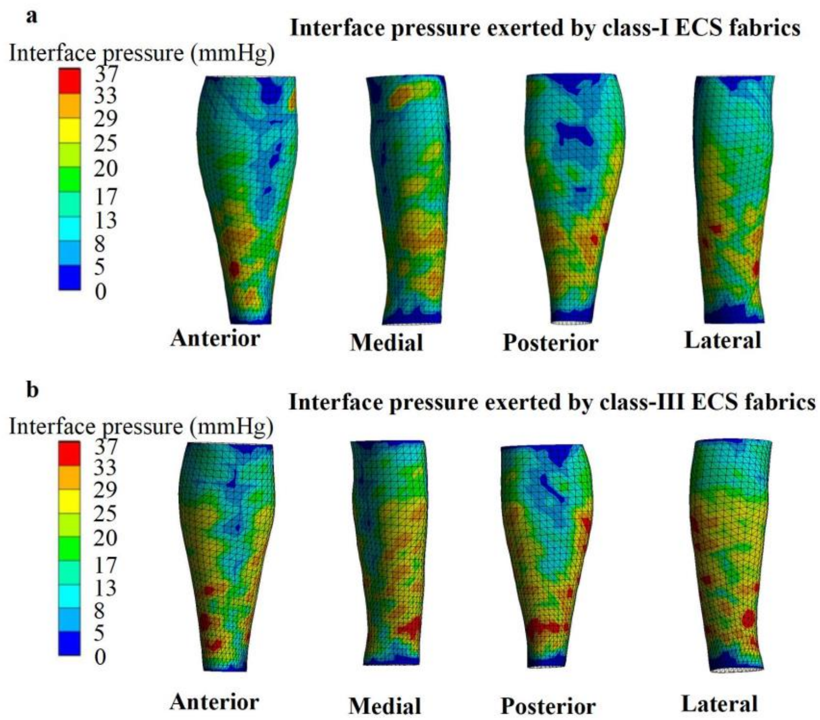

Figure 5.5 The simulated interface pressure exerted by (a) Classes I and (b) III ECSs samples for subject 2.

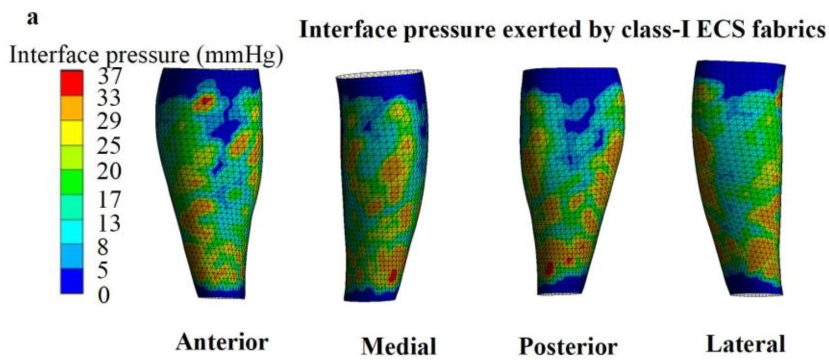

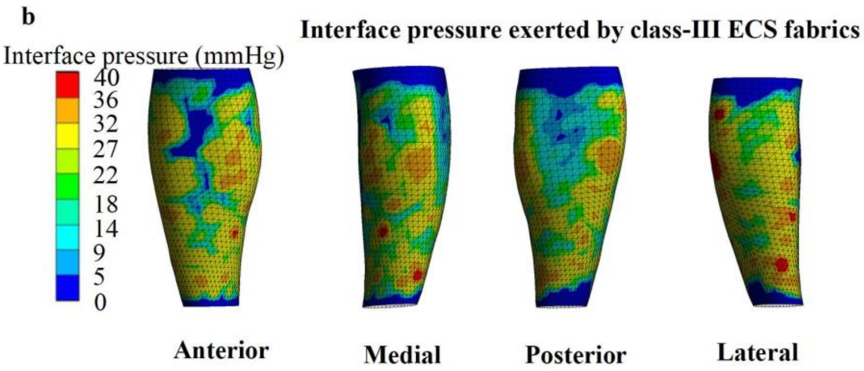

Figure 5.6 The simulated interface pressure exerted by (a) Classes I and (b) III ECSs samples for subject 3.

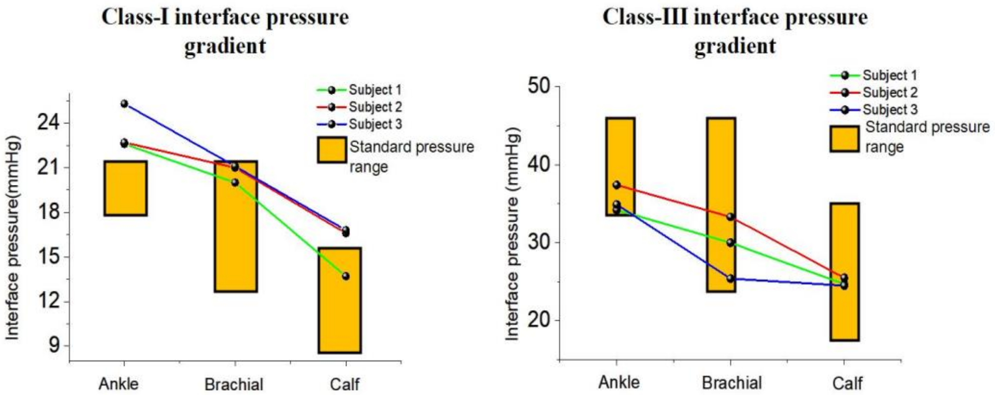

Figure 5.7 Comparison between the simulated and standard pressure levels and gradient pressure distributions of the studied 3 subjects.

5.3.2 Determined Relationships between Skin Pressure and Body Curvatures

Lower limb morphologies and surface curvatures directly influence contact conditions with the ECSs. Fig. 5.8 and Fig 5.9 illustrates the relationship between the surface curvatures of the studied lower limb and the correspondingly produced interface pressure beneath tailor-made ECSs. The greater curvatures of the leg cross-sectional contour present smaller radius of the curvatures. The regions with the greater curvatures produced generally higher interface pressure than that at the regions with smaller curvatures, which was consistent with the Laplace’s Law.

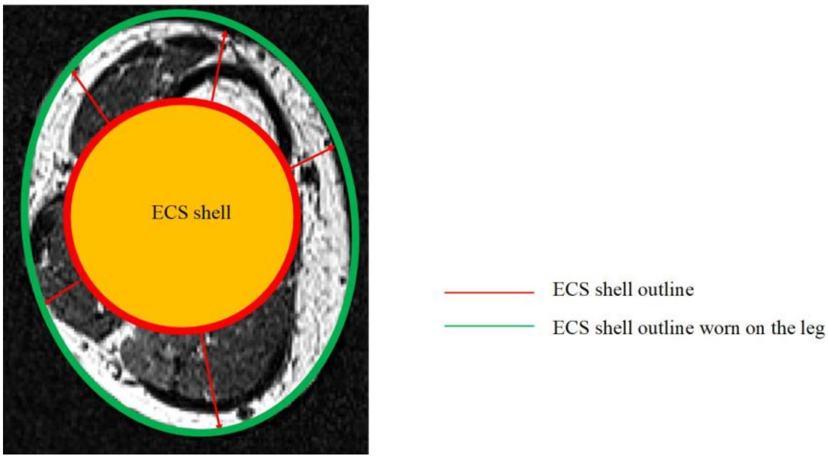

Figure 5.8 The relationship between the deformation of the ECS fabrics and leg curvature.

Meanwhile, the presence of the tibia and fibula bones with higher stiffness also affected the distributions of interface pressure over lower limb soft tissues, thus varying the interface pressure to be nonlinear at some sites around the lower limb.

It was found that the highest interface pressures occurred at the anterior and posterior regions where tibia and soleus bones are located, respectively. These two regions have greater Young's moduli and higher surface curvatures but less tissue deformation and strain when ECS was being applied.

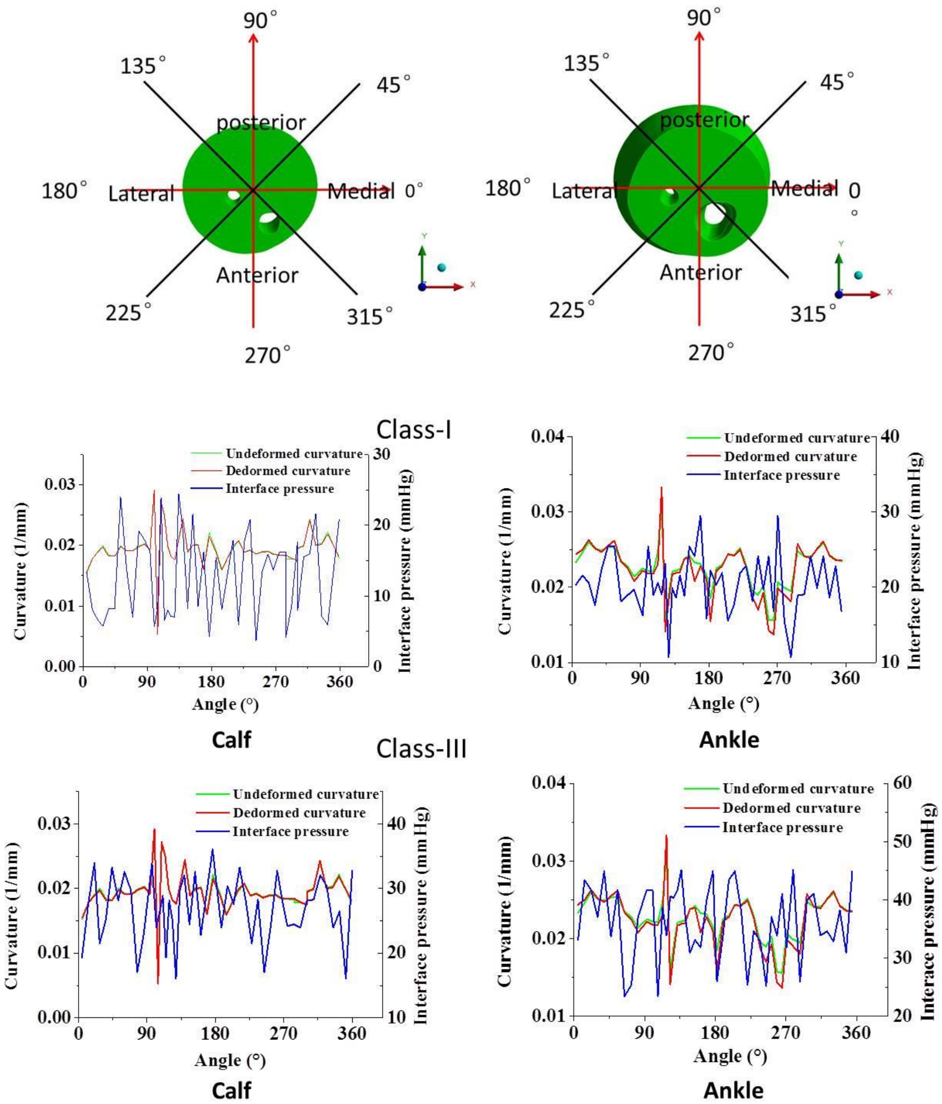

Figure 5.9 The relationship between the leg curvature and skin pressure at ankle and calf regions exerted by (a) Class-I and (b) Class-III ECS fabrics.

5.3.3 Characterized Stress Transmission Behaviors from Skin to Deeper Tissues

Stress transmission behaviors from the skin to the deeper tissues of the lower limb were numerically analyzed through the determined four paths cross-sectionally (Fig. 5.10), including the paths towards the two main superficial veins (small saphenous venous SSV and the greater saphenous venous GSV), and another two paths towards main anatomic bones (tibia and fibula). The paths 1 and 4 from tibia and fibula, respectively, to the peroneal vein (PV) was applied to detect the stress transmission at the bones, which indicated the mechanical responses of the soft tissue near the bones; and the paths 2 and 3 from the SSV and GSV to the PV, respectively, was used to detect the stress transmission at the veins, which indicated the mechanical responses of the soft tissue near the venous system. The stress distribution at the venous wall can be used to indirectly assess the venous hemodynamic responses to the application of ECS.

It was seen that the inner stress distributions were uneven due to heterogeneous tissue structures and stiffnesses. The inner tissue stresses were gradually decayed from the periphery to the center (Table 5.4). For Class-I ECS-leg system, the tissue stress were approximately 2,533 Pa at the posterior ankle (i.e., the starting site of the path 3) and then gradually decreased to approximate 2,451 Pa and 1,528 Pa to the SSV and GSV, respectively, and decreased to 455 Pa near the deep veins (PV), and 450 Pa and 785 Pa near the fibula and tibia, respectively, at the ankle level. The stress variation ratios VROs from the periphery (tissue surface) to the SSV and GSV were -3.2% and -41.6 %, and -82.2 % to deep veins (PV), and -82.2 % and -69.0 % to fibula and tibia, respectively, at the ankle section. Conversely, the tissue stress was approximately 2,100 Pa at the periphery calf (the starting site of the path 4) and gradually reduced to approximate 1,350 Pa near the studied veins while increased to 1,528 Pa and 2,451 Pa till the tibia and the fibula, respectively, at the same calf level. The stress VROs from SSV to PV were approximately -80 % and -55 % at the ankle and brachial section. Similarity, the stress VROs from GSV to PV were approximately -70 % and -55% at the ankle and brachial section, respectively.

The unevenness of inner stress distributions and tissue deformation was largely due to the differential interface pressure on the skin and irregular morphologies of biocomponents and varying thickness of subcutaneous fat within lower limb tissues.

In general, ECS pressure exerted the higher mechanical squeezing forces to the superficial venous walls (GSV and SSV) than those applied to deep venous wall (PV), implying that the designed pressure doses of ECS could be loss or transforming during the delivery process from the peripheral to the central, thus exerting insufficient or varying pressure doses to the targeted veins, which would influence biomechanical function of ECSs in regulating venous calibers and venous hemodynamics in use.

Table 5.4 Stress distributions and variations along specific paths within ankle, calf, and knee cross-sections.

Class	Region	At skin surface		At vein walls (Pa)			At bone surface (Pa)	
				SSV	GSV	PV	Fibula	Tibia
I	Ankle (B)	Skin pressure (Pa)	2,533	2,451	1,479	455	450	785
		VRO (%)	0	**-3.2***	**-41.6**	**-82.0**	**-82.2**	**-69.0**
		Path depth (mm)	0	5	5	35	25	20
	Brachial (B1)	Skin pressure (Pa)	2,102	2,099	2,138	946	2,483	2,258
		VRO (%)	0	**-0.1**	**-1.7**	**-55.0**	18.1	7.4
		Path depth (mm)	0	5	5	45	35	23
	Calf (C)	Skin pressure (Pa)	1,528	1,338	1,400	1,349	2,430	1,681
		VRO (%)	0	**-12.4**	**-8.4**	**-11.7**	59.0	10.0
		Path depth (mm)	0	5	5	55	40	25
III	Ankle (B)	Skin pressure (Pa)	3480	3498	2317	573	1445	1148
		VRO (%)	0	**-0.5**	**-33.4**	**-83.6**	**-58.5**	**-67.0**
		Path depth (mm)	0	5	5	35	25	20
	Brachial (B1)	Skin pressure (Pa)	3190	2914	3202	1304	3480	3266
		VRO (%)	0	**-8.7**	0.4	**-59.2**	9.1	2.3
		Path depth (mm)	0	5	5	45	35	23

	Calf (C)	Skin pressure (Pa)	2543	2209	2480	2223	4047	2910
		VRO (%)	0	**-13.1**	**-2.5**	**-12.6**	59.1	14.4
		Path depth (mm)	0	5	5	55	40	25

* The negative values indicated that the tissue stresses at the special position are less than that at the skin surface, indicating the stress reduced from the skin surface to the internal deeper tissues.

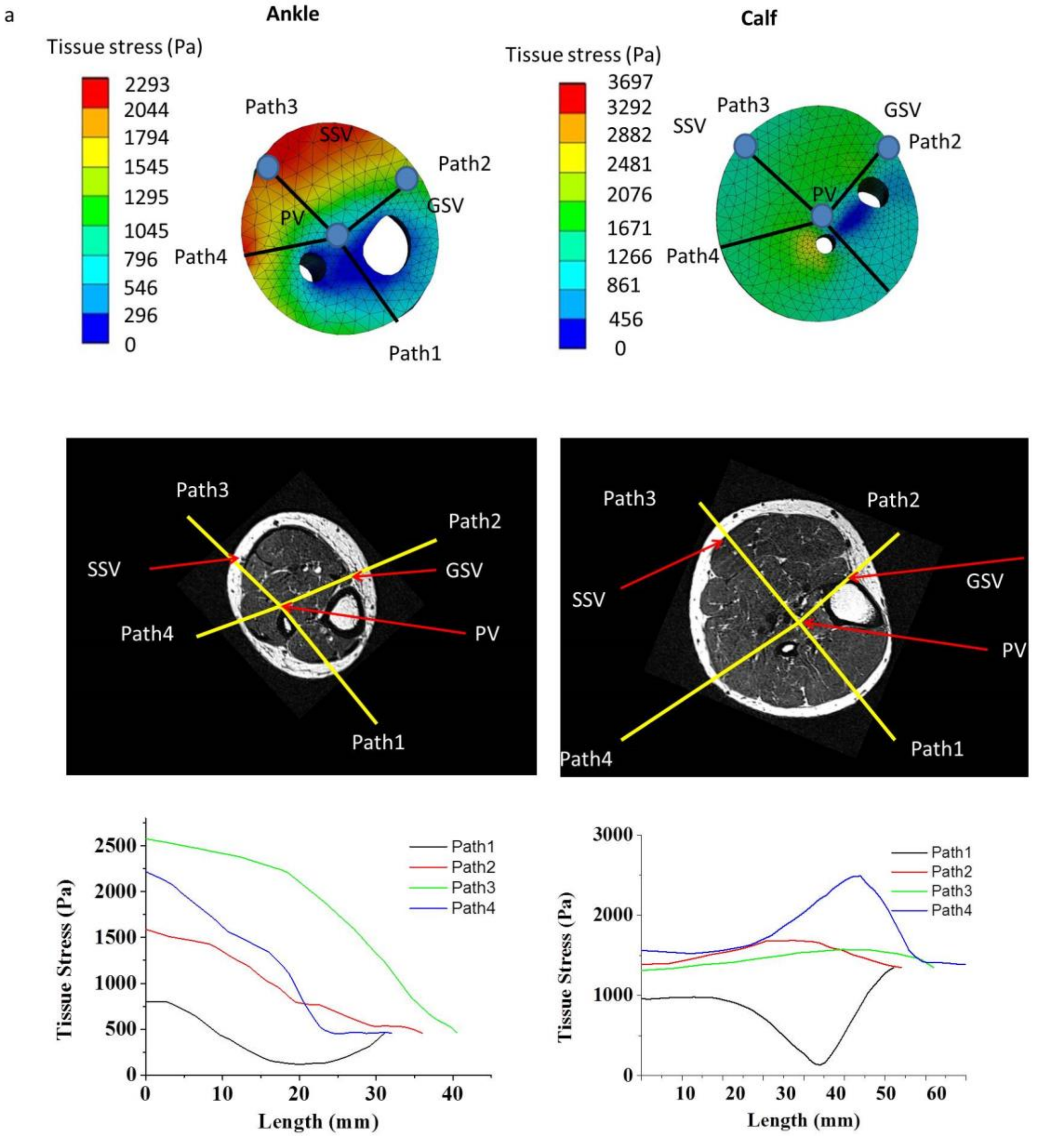

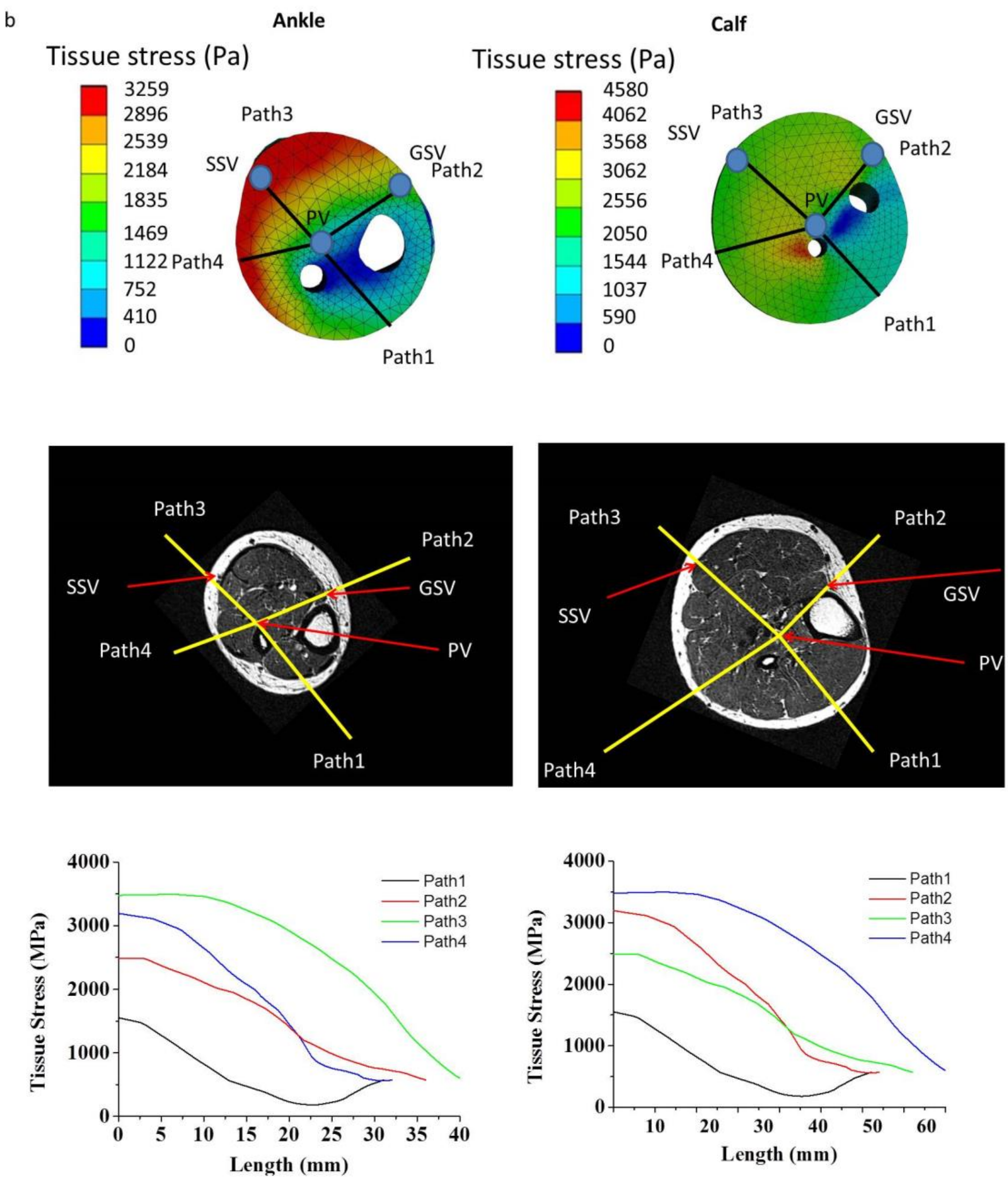

Figure 5.10 Simulated stress transmission profiles exerted by ECSs with (a) lower Class-I and (b) the higher Class-III pressure levels from the periphery to the center lower limb tissues at the ankle and calf regions, respectively.

5.3.4 Simulated Tissue Deformation Induced by ECSs with Different Pressure Levels

The corresponding tissue deformation at the ankle and calf sections exerted by Classes I and III ECS was shown in Fig. 5.11. The tissue deformations gradually decayed from the periphery (e.g., skin surface and superficial venous wall (GSV and SSV) to the center (PV) and no deformation was found around the bones in the cross-section. The simulated maximum tissue deformations were approximately 2.78 mm and 3.53 mm at the posterior ankle exerted by Class I and III ECSs, respectively. Similarity, the simulated maximum tissue deformations were 5.88 mm and 9.66 mm at the posterior calf by Class I and III ECSs, respectively. Along the lower limb, the less tissue deformation was found at ankle and gradually increased to the calf, and the less tissue deformation was found when wearing Class-I ECS fabrics and gradually increased by wearing the Class-III ECS fabrics.

a

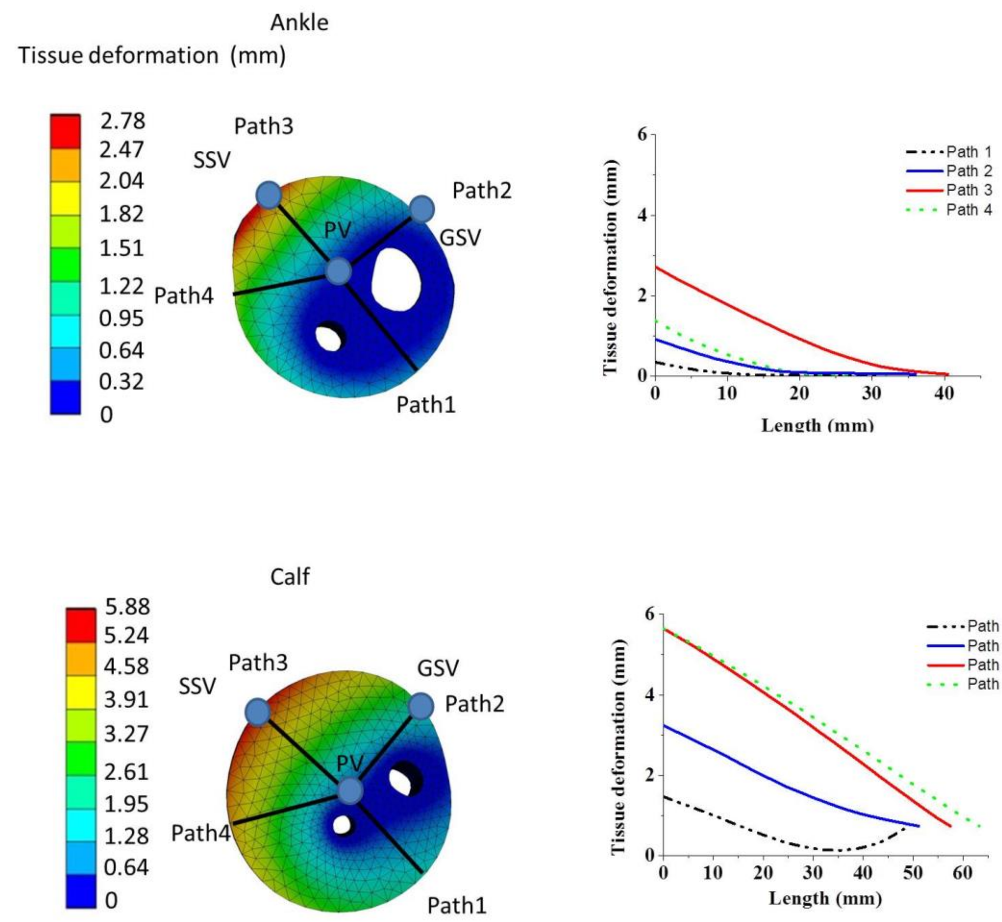

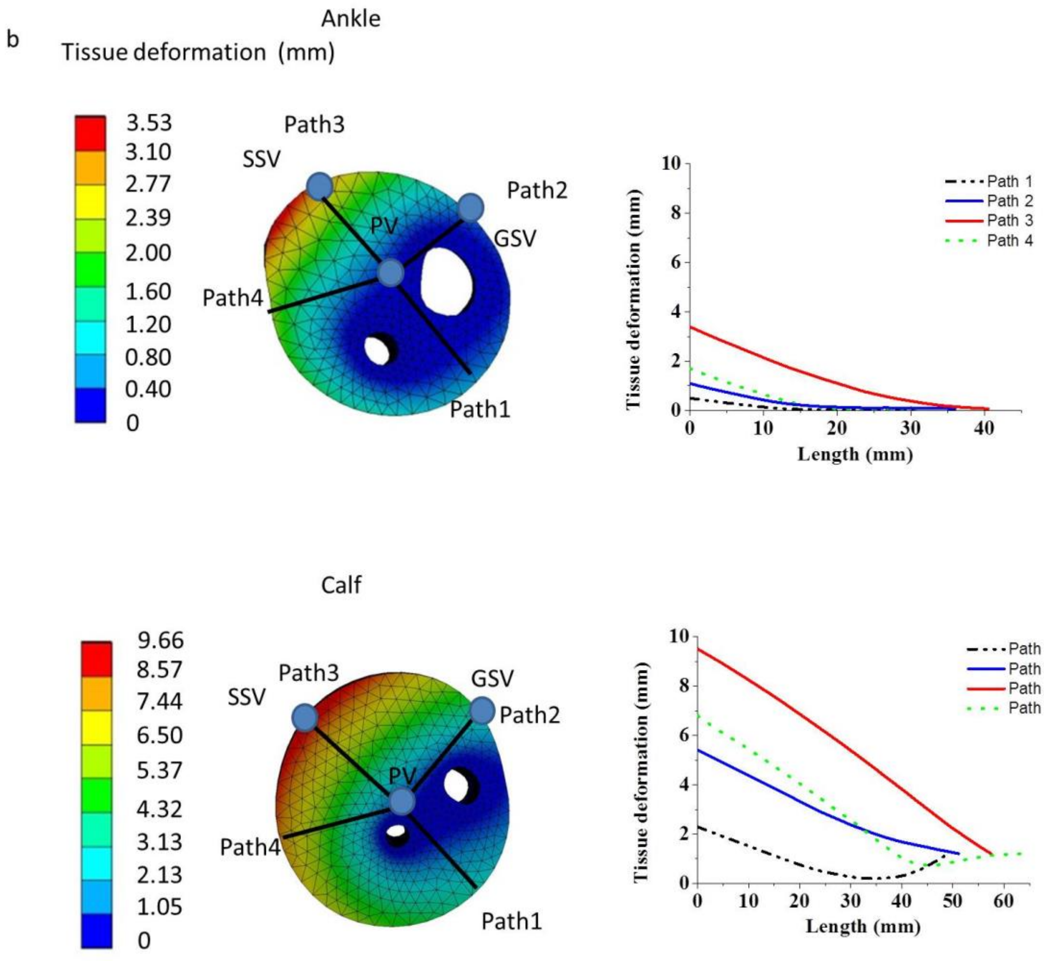

Figure 5.11 Simulated tissue deformation exerted by ECSs with (a) lower pressure Class-I and (b) the higher pressure Class-III along four determined paths at the ankle and calf, respectively.

5.3.5 Optimized Skin Pressure Simulation by a Refined Subject-Specific Model

In Chapter 5.3.6, it can be seen that the highest DROs between the stimulated and the measured pressure values based on the determined tissue properties occurred in the FE ECS-leg model of subject 2, as the average DROs among three subjects were 7.5% (subject 1), 16.6% (subject 2), and 11.4% (subject 3), respectively.

To further reduce the DROs between the simulated and the measured pressure values, a refined subject-specific FE ECS-leg model was developed in this section for subject

2. The muscle groups of the lower limb were divided into the four different parts with the input of the uneven tissue stiffnesses by applying the aforementioned SWE technology (Section 5.2.4). The four parts included anterior muscles group (anterior section), soleus (medial and posterior section), deep layer of the posterior muscle group (medial and posterior section), and lateral muscles group (lateral section) based on anatomic structures of the lower limb (Fig. 5.12). The refined geometry model of the lower limb of subject 2 with the determined tissue properties was input to Ansys workbench for numerically analyzing the interface pressure induced by the ECSs.

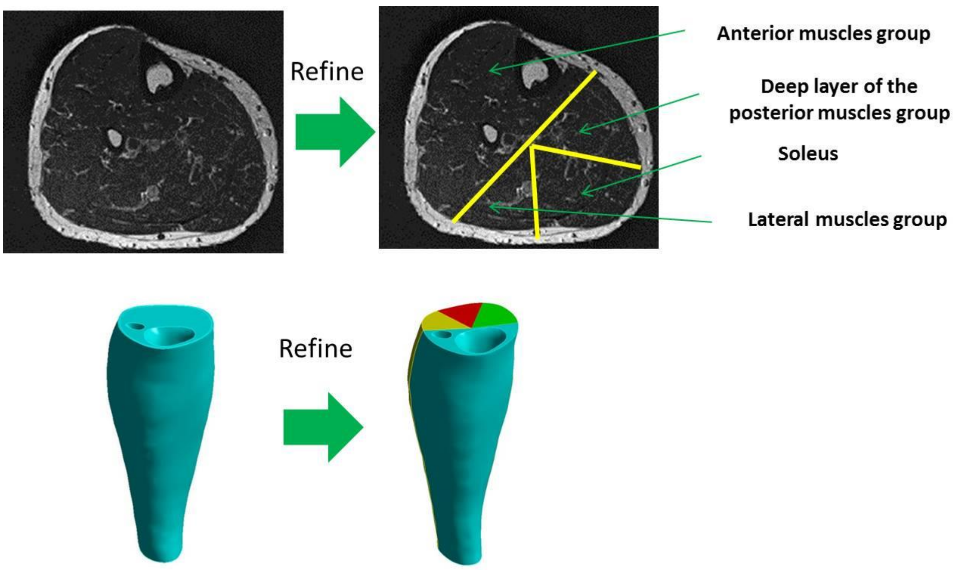

Figure 5.12 The refined subject-specific geometry leg model with the divided four parts with input of uneven muscle stiffnesses for tissues.

Fig.5.13 indicated the simulated skin pressure applied by Classes I and III ECS samples along and around the lower limb tissues based on muscle group tested. It is observed that the higher pressure distributed at the ankle and gradually decreased up to the knee. The simulated average pressure at the ankle were approximate 24.9 and 34.5 mmHg for Classes I and III ECSs, respectively; Correspondingly, the simulated average pressure at the brachial were about 18.7 and 23.6 mmHg for Classes I and III

ECSs, respectively, and about 13.8 and 21.6 mmHg at the calf for Classes I and III ECSs, respectively. The pressure gradient ratios from the ankle (B), brachial (B1), to the calf (C) heights were 100 %, 75.2 %, and 55.3 % for Class-I ECS, and 100 %, 72.0 %, and 62.7 % for Class-III ECS, respectively.

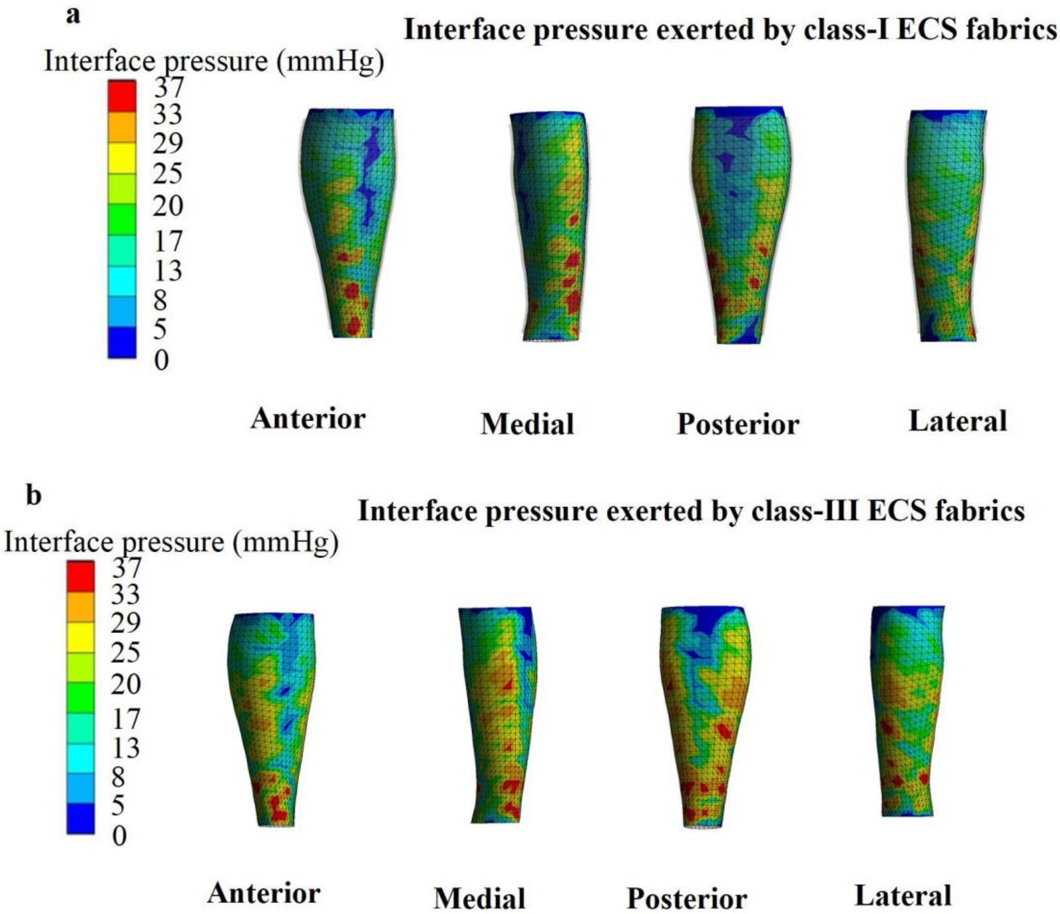

Figure 5.13 The simulated interface pressure exerted by Classes I and III ECSs by using the refined subject-specific model on subject 2 with input of the determined muscle stiffnesses at the four different parts.

5.3.6 Validation of the Built FE ECS-Leg System

To examine whether the refined subject-specific FE ECS-leg model improved the simulation precision, the validation work was conducted using an air-filled pneumatic pressure-sensing system (PicoPress, Microlab Elettronica Sas, Italy; pressure range: 0-

189 mmHg; deviation within ± 1mmHg; sensing probe: 5 mm in a diameter and 0.2 mm in a thickness). The comparison analysis were made under the three conditions, including the comparison between the measured skin pressure and (i) the simulated skin pressure based on the referred tissue properties for subject 1; (ii) the simulated skin pressure based on the experimentally determined tissue properties for Subjects 1, 2, and 3; and (iii) the simulated skin pressure based on the determined subject-specific tissue properties at the refined FE leg model with the four divided muscle groups for subject 2. The details are shown as follows.

Condition (i) — validation by using the referred tissue properties

Table 5.5 presented the comparison between the measured and the simulated interface pressure at the twelve landmarks along the subject 1's lower limb induced by ECSs with Classes I and III by using the referred tissue properties (i.e., hyperelastic coefficient (C_1=5000 Pa, D_1= 1.4×10^{-7} Pa^{-1}). Most of the testing points presented agreement between the simulated and the measured interface pressure, especially for Class-I, which demonstrated the applicability of the developed FEM in pressure assessment. The DROs between the simulated and the measured pressure values were approximately 11.7 %, 12.3 %, and 16.3 % at the ankle, brachial and calf for Class-I ECS, respectively, and 4.7 %, 15.6 %, and 6.1 % at the ankle, brachial and calf for Class-III ECS, respectively. The larger deviations occurred at anterior and posterior ankle.

Table 5.5 Comparison between the simulated and measured interface pressures for Subject 1 with use of the referred tissue properties under application of Class-I and Class-III ECSs.

ECS Classes	Regions	The simulated		The measured		DROs (%)	Average DROs (%)
		Skin pressure (mmHg)	Pressure gradients (%)	Skin pressure (mmHg)	Pressure gradients (%)		
Class-I	Ankle (B)	23.8±4.6	100	21.3±5.8	100	11.7	11.1
	Brachial(B1)	21.0±5.0	88.2	18.7±0.9	87.8	12.3	
	Calf (C)	14.4± 6.2	60.6	17.2±1.8	80.8	16.3	
Class-III	Ankle (B)	35.3±6.4	100	33.7±8.5	100	4.7	
	Brachial (B1)	31.5±4.6	89.2	26.6±2.2	78.9	15.6	
	Calf (C)	26.2±5.1	74.2	24.7±1.7	73.3	6.1	

Condition (ii) — validation by using the experimentally determined tissue properties

The DROs between the simulated and the measured pressure values were approximately 6.1 %, 7.0 %, and 20.3 % at the ankle, brachial and calf for Class-I ECS, respectively, and 1.5 %, 12.8 %, and 0 % at the ankle, brachial and calf for Class-III ECS, respectively, when applied on subject 1 with use of the experimentally determined tissue properties on average.

It was found that the average DROs between the simulated and the measured pressure values reduced from 11.1% to 7.5% for subject 1 (Fig. 5.14). This means that the determined tissue properties reflected more real mechanical performances and deformation in the FE ECS-leg system compared with the referred tissue properties.

Table 5.6 Comparison between the simulated and measured interface pressures based on the experimentally determined tissue properties of three subjects by using Classes I and III ECSs.

Subject No.	ECS Classes	Regions	The simulated		The measured		DROs (%)	Average DROs (%)
			Skin pressure (mmHg)	Pressure gradients (%)	Skin pressure (mmHg)	Pressure gradients (%)		
Subject 1	**Class-I**	**Ankle (B)**	**22.6±4.6**	**100**	**21.3±5.8**	**100**	**6.1**	**7.5**
		Brachial (B1)	**20.0±5.0**	**88.2**	**18.7±0.9**	**87.8**	**7.0**	
		Calf (C)	**13.7± 6.2**	**60.5**	**17.2±1.8**	**80.8**	**20.3**	
	Class-III	**Ankle (B)**	**34.2±6.3**	**100**	**33.7±8.5**	**100**	**1.5**	
		Brachial (B1)	**30.0±4.6**	**88.0**	**26.6±2.2**	**78.9**	**12.8**	
		Calf (C)	**24.7±5.3**	**72.3**	**24.7±1.7**	**73.3**	**0**	
Subject 2	Class-I	Ankle (B)	22.7±6.0	100	18.9±2.8	100	20.1	16.4
		Brachial (B1)	21.0±5.5	92.5	17.4±3.1	92.1	20.7	
		Calf (C)	16.6± 7.4	73.1	15.8±3.3	83.6	5.1	
	Class-III	Ankle (B)	37.4±6.5	100	30.0±3.5	100	24.7	
		Brachial (B1)	33.3±4.7	89.0	27.1±1.7	90.4	22.9	
		Calf (C)	25.5±6.7	68.1	24.1±1.4	80.4	5.8	
Subject 3	Class-I	Ankle (B)	25.3±5.5	100	21.1.1±2.2	100	19.9	11.4
		Brachial (B1)	21.1±6.7	83.4	18.1±3.0	85.8	16.6	
		Calf (C)	16.8± 6.3	66.4	16.2±2.0	76.8	3.7	
	Class-III	Ankle (B)	34.5±6.1	100	32.3±5.3	100	6.8	
		Brachial (B1)	25.4±3.9	71.8	27.4±4.6	82.3	7.3	
		Calf (C)	24.5±5.0	71.0	21.5±4.6	66.6	14.0	

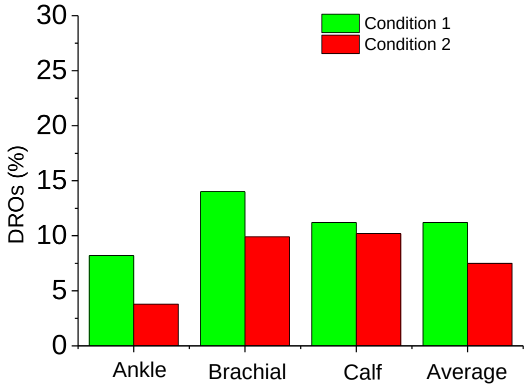

Figure 5.14 The DROs comparison under conditions (i) and (ii) for subject 1.

Condition (iii) — validation using the refined model with determined uneven tissue properties

Based on the results shown in Table 5.6, it was found the DROs for subject 2 is relatively higher. To reduce the DRO values, a refined subject-specific FE-leg model for subject 2 was further proposed and validated. By using the refined model, the results indicated that the DROs between the measured and the simulated skin pressure values reduced to be approximate 31.7 %, 7.5 %, and 12.7 % at the ankle, brachial and calf for Class-I ECS, respectively, and 15.3 %, 13.7 %, and 10.4 % at the ankle, brachial and calf for Class-III ECS, respectively (Table 5.7). That is, the input of the determined uneven tissue properties in the refined FE ECS-leg system improved the simulation precision of the skin pressure by approximate 8.9% (Fig. 5.15). This means that the refined model can reflect the muscle segment stiffnesses to characterize the real mechanical properties in lower limb to reduce DROs in the FE ECS-leg system.

Table 5.7 Comparison between the simulated and measured interface pressures based on the refined FE leg-ECS model for subject 2 with the experimentally determined tissue properties

ECS Classes	Regions	The simulated		The measured		DROs (%)	Average DROs (%)
		Skin pressure (mmHg)	Pressure gradients (%)	Skin pressure (mmHg)	Pressure gradients (%)		
Class-I	Ankle (B)	24.9±4.6	100	18.9±2.8	100	31.7	15.2
	Brachial (B1)	18.7±5.0	75.2	17.4±3.1	92.1	7.5	
	Calf (C)	13.8±6.2	55.3	15.8±3.3	83.6	12.7	
Class-III	Ankle (B)	34.6±6.4	100	30.0±3.5	100	15.3	
	Brachial (B1)	23.6±4.6	72.0	27.1±1.7	90.4	13.7	
	Calf (C)	21.6±5.1	67.2	24.1±1.4	80.4	10.4	

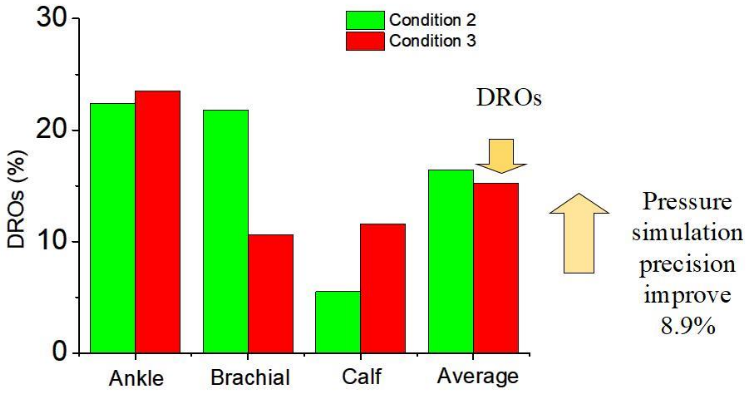

Figure 5.14 The DROs comparison under conditions (ii) and (iii) for subject 2.

In general, the simulated interface pressure under all of three conditions showed the similar tendency and magnitudes with the measured pressure, among them, the DROs ranged from 0 to 31.7 %, which demonstrated the applicability of the developed FEM in pressure assessment.

The main reasons for deviations occurred between the simulated and measured pressures could be resulted from several aspects, (i) the use of 2D mechanical properties of ECS fabrics in pressure simulation cannot reflect the mechanical properties of ECS fabrics along the wale, course, and thickness directions. Therefore, a new method to determine the ECS properties in a 3D scale was proposed in Chapter 3. (ii) the referred tissue properties existed deviation to the tissue properties of the specific subjects' tissue properties to cause the DROs, and (iii) the usage of the average tissue properties would result in the deviations in pressure simulation compared to the usage of the uneven tissue properties along or around the lower limbs. The refined subject-specific model with the experimentally determined uneven tissue properties developed in this Chapter optimized the skin pressure simulation with a reduction of DROs. In addition, in the current FE model, the ECS was assumed to be an orthotropic shell with an ignorance of the micro-structure of knitted loops, and meanwhile the muscle stiffness was used as the major stiffness of FE ECS-leg system, these factors could also influence the contact condition between ECS fabric layer and skin surface.

5.4 Summary

This Chapter developed a mixed numerical and experimental approach to characterize biomechanical performance of the tailor-made ECSs with different pressure levels on lower limb tissue system. Transmission behaviors of ECS pressure on and within lower limb tissues were numerically simulated by the developed FEM.

Both referred tissue properties and experimentally determined tissue properties were applied in this Chapter. The results showed that the DROs between the simulated and the measured pressure values by using the determined tissue properties reduced by 8%. That is, the simulation precision of the optimized FE ECS-leg model was improved by 50%. Moreover, the DROs between the simulated and the measured pressure values by using the refined subject-specific model with the determined unevenness tissue properties further reduced by 0.3%. That is, the simulation precision of the further optimized FE ECS-leg model was improved by more 8.9 %. In general, the proposed new (refined) methods raised the simulation precision by 58.9% (50%+8.9%) in total, which remarkedly contributed to improvements of the accuracy for pressure prediction in ECS design.

In general, the simulated interface pressure induced by ECSs showed agreement with the measured data by using the developed FE ECS-leg system, indicated the applicability of the developed model in pressure analysis and prediction. The irregular lower limb shapes, heterogeneous tissue structures, and uneven tissue stiffnesses varied the distributions and transmission profiles of interface pressure and corresponding internal tissue stresses caused by ECSs.

The simulated pressure levels and gradient proportions were similar among the three studied subjects. The greatest interface pressure beneath ECSs with either Class I or Class III were at the posterior and anterior ankle regions while the less pressure occurred at knee and calf regions, which closely related to the lower limb surface curvature distributions in accordance with Laplace’s Law. The degressive gradient pressure from the ankle to the knee was observed along the lower limbs longitudinally, which satisfied the gradient pressure requirements of RAL-GZ 387/1 standard.

Inner tissue stresses caused by external interface pressure of ECSs gradually decreased from the peripheral to the central soft tissues, implying that tissue stresses gradually lost during the transmission process from the skin, superficial veins to the deeper veins, which could induce insufficient pressure doses delivered by ECSs to deeper venous system, resulting in recrudescence of venous disorders.

This study provides a new approach to enhance the understanding of working mechanisms of ECS and lower limb interactions and pressure transmission, which contribute to constructing the relationships between the interface pressures and venous wall stresses for discussion of the venous hemodynamic responses induced by the

ECS fabrics in the followed Chapter 6.

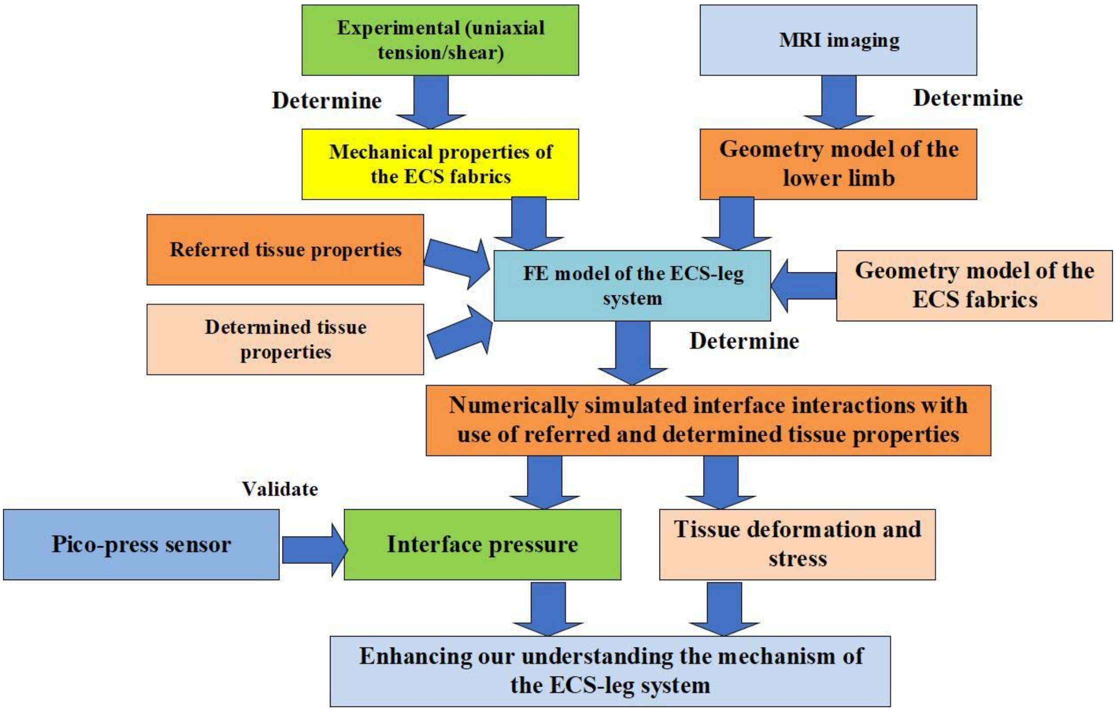

Figure 5.15 Framework of Chapters 4 and 5.

CHAPTER 6 FLUID-SOLID INTERACTION MODELLING THE EFFECTS OF ECSs ON LEG-TISSUE-VEIN SYSTEM

6.1 Introduction

The interface pressure and tissue stress transmission has been numerically analyzed in Chapter 5. The magnitudes and distributions of the stresses induced by ECSs on the venous wall influence the venous hemodynamics. Thus, to fully understand the ECS work mechanisms on the venous system, a numerical model was developed in this Chapter to quantitatively analyze the venous hemodynamic responses towards the application of ECSs with different pressure levels.

The existing studies applied the 0D or 1D model to predict venous hemodynamic properties (Shi, et al 2011) in the blood system, where 0D model provide a concise way to predict the hemodynamic response in the blood system, and 1D model also simplified the network of the blood system compared with the higher dimensional computational fluid dynamics, however, these methods cannot reflect the venous flow hemodynamic responses towards the ECSs in a 3D scale; and very few studies reported the venous hemodynamic properties including flow velocity, wall shear stress and blood pressure in a 3D ECS-leg modelling system. Therefore, in this Chapter, a new fluid-solid interaction model (FSI) was constructed to analyze venous hemodynamic responses induced by the application of ECSs with different pressure profiles, to enhance our understanding of the effects of the ECSs on the deeper venous structures and flow of the lower limbs.

6.2 Methods

6.2.1 FSI Modelling the Effects of ECSs on Leg-Tissue-Venous System

In this section, the fluid analysis and meshing construction of veins and tissues were performed. The geometries and spatial positions of the peroneal vein (PV), the small saphenous vein (SSV), and the great saphenous vein (GSV) of the lower limb were reconstructed. CVI symptoms frequently occurs along these superficial veins (Eberhardt, et al. 2014). Moreover, venous thrombosis is the most frequently occurred at the PVs (Labropoulos, et al. 1999). Thus, the hemodynamic responses of the GSV, SSV, and PVs towards ECSs application were numerically studied in this chapter. The geometric structures of these veins were constructed by smooth treatment as a circle since the fewer pixels involved there would induce irregular vein surfaces, thus influencing the calculation accuracy (Fig. 6.1). Considering the effects of the gender on hemodynamic response in the tissue-veins system, the geometry models of two subjects (female subject 1 and male subject 3) were reconstructed, which were input to the Ansys workbench system coupling for the FSI simulation and analysis.

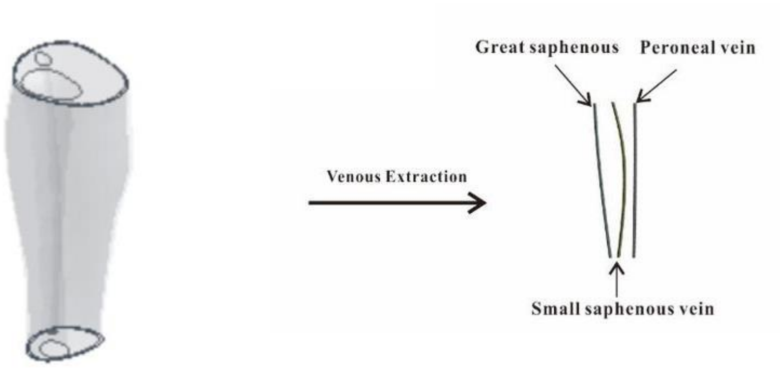

Figure 6.1 Reconstruction of the lower limb and vein structures of subject 3.

The Reynolds number (*Re*) is an important dimensionless quantity in fluid mechanics that is used to predict flow patterns in the different fluid flow situations. It can be defined as below,

$$Re = \frac{\rho v L}{\mu} \tag{6.1}$$

where ρ is the density of veins, and v and μ denote the flow velocity and dynamic viscosity of the veins, respectively. L is the length of the vein. If the *Re* of the vein was less than 2300, the flow of the studied vein can be regarded as laminar flow, which means that the direction of the venous flow parallels to the venous wall. The venous flow moves in a straight line parallel to the venous wall without eddies and swirls. Navier-Stokes equation has been used to analyze venous hemodynamic properties including velocity and pressure (Spurk, et al. 2020). The venous flow can be analyzed through Poiseuille's Law, which is used to analyze the steady flow of an incompressible fluid parallel to the axis of a circular pipe of infinite length. The venous center is moving fastest while the venous wall is stationary with no-slip condition based on Poiseuille Law. Navier-Stokes equation can be simplified as (Eq. 6.2):

$$\frac{dp}{dx} = \mu \frac{d^2 u}{dy^2} \tag{6.2}$$

Based on the venous flow system analysis by using Navier-Stokes equation, the venous flow velocity was 0 at the venous wall, and the maximum venous velocity was at the centre of the venous flow.

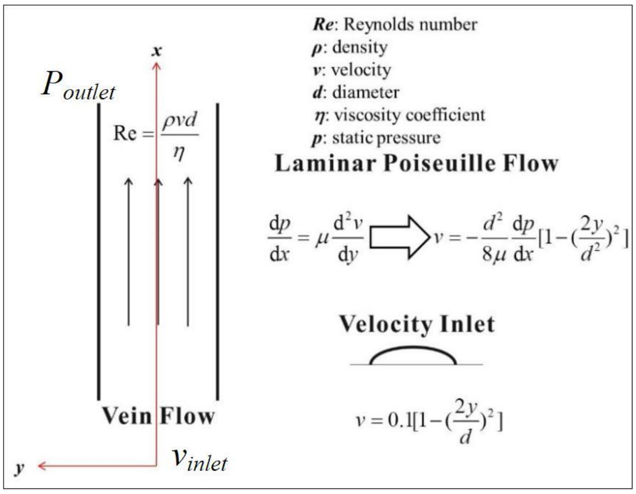

Figure 6.2 Venous flow theory.

The venous models were meshed using the fluent hexagon elements with the boundary layer (Fig. 6.3). The total elements were approximately 75,000 in the vein model. Dynamic mesh was applied in the FSI model at the fluid-solid interaction boundary through smoothing, layering, and remeshing methods.

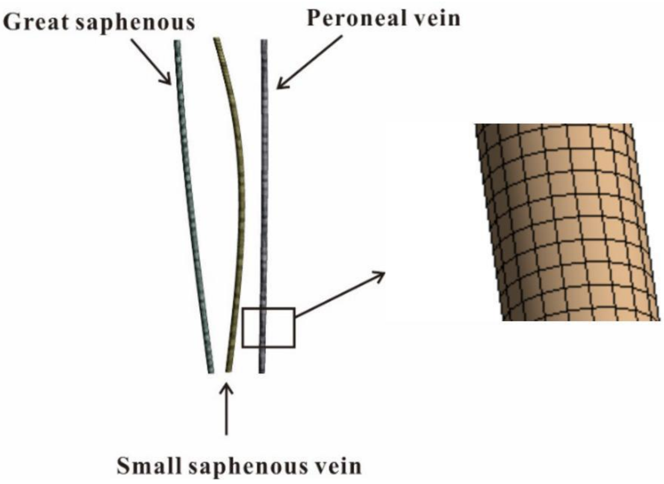

Figure 6.3 Meshing for the studied vein models.

6.2.2 Boundary Conditions of the Veins and Tissues Interaction

The velocity inlet (v_{inlet}) was determined based on Doppler ultrasound test (DUT) (Aixplorer, Aix-en-Provence, France). DUT is medical ultrasonography that employs the Doppler effect to generate the images of the deformation of the tissue and flow of the blood (Gao, et al. 1986). Based on the DUT, the venous flow status can be determined and visualized by computing the frequency shift of a particular sample volume. In this study, the vascular probe was put on the posterior position at the below knee to orientate the popliteal venous (POVs) position. The test was conducted in an environment with a relative humidity of 65% ± 2% and temperature of 21±1°C. The tested average venous velocities were set as the velocity inlet via User Defined Function (UDF) and the venous flow pressure was set as the outlet (P_{outlet}) with a value of 0 Pa, respectively, which means that the venous flow can be regarded as a free outflow (Fig 6.4). The venous flow can be regarded as a sine function, the average value can be estimated as follows,

$$\bar{v} = \frac{\int_0^T v(t)dt}{t} = \frac{\int_0^T v_{\max} \sin\frac{t\pi}{T} dt}{t} = \frac{2v_{\max}}{\pi} \tag{6.3}$$

where T is the cycle time of the vein and v is the venous velocity. Based on the tested venous velocity and the venous flow analysis, the venous velocities are uneven at the cross section and fluctuate during a cycle, where the venous flow velocity was 0 at the venous wall, and the maximum venous velocity was at the centre of the venous flow and the venous flow can be regarded as a sine function during a cycle. Moreover, the average venous flow at the centre (AVF) would be analyzed in this chapter.

Figure 6.4 The tested venous velocity via the Doppler ultrasound test.

In this study, the inlet of POVs velocity was tested by using the DUT. The inlet of the POVs was connected with the outlet of the PV (Butros, et al. 2013), which are equivalent to the PV outlet velocities. In addition, the AVF velocities of the PV are constant (Wei, et al. 1998), thus, the tested AVF velocities of the POVs without ECS fabrics can be regard as the velocity inlet in the FSI tissue-veins system, and the tested AVF velocities of the POVs with ECS fabrics can be applied to validate the simulated velocities with the ECS fabrics at the PVs outlet.

To determine the AVF velocities of POVs, in this study, subjects 1 and 3 were tested on the POPs without wearing ECS when being standing position by using DUT. The determined average venous velocities were shown below.

Table 6.1 The tested AVF velocities of POVs by using DUT assessment.

Subject code	Determined AVF velocities of the POV (cm/s)
1	3.06
3	2.54

And then, the external pressure exerted by ECSs with Classes I and III was applied on the skin based on the simulated pressure in Chapter 5. A coupling system combining the static structure module (leg-tissue system) and fluent module (venous system) with the steady solution were developed in the FSI model. The venous walls were defined as an SFI interface. The time step of the FSI coupling system was set as 5 and the iteration number of fluent was set as 2000 based on the empirical studies.

6.3 Results and Discussion

6.3.1 The Simulated Venous Velocities based on the Built FSI Model

The flow velocities of the studied veins under the pressure applied by ECSs with Classes I and III were simulated for subjects 1 and 3. The simulation results showed that the flow velocities were generally increased with the intervention of the ECSs. By applying Class-I ECS, the AVF velocities of the PV, SSV, and GSV at the P_{outlet}, were 3.15 cm/s, 3.34 cm/s and 3.44 cm/s for subject 1, respectively; and 2.61 cm/s, 2.77 cm/s and 2.87 cm/s for subject 3, respectively. Similarly, the AVF velocities of the PV, SSV, and GSV at the P_{outlet} when applying Class-III ECS were 3.27 cm/s, 3.58 cm/s and 3.7 cm/s for subject 1, respectively; and 2.75 cm/s, 2.97 cm/s and 3.07 cm/s for subject 3, respectively (Fig. 6.5-Fig 6.7).

In general, the central average flow velocities of the SSV and the GSV were higher than those of the PV. Based on Poiseuille Law and Continuity equation, the increase of the external pressure applied on the venous walls can induce the increased v. The pressure exerted on the venous wall was dependent on the soft tissue stress around the venous wall. The higher tissue stresses could induce the increased pressure on the venous wall. The increased pressure squeezes the soft tissues to produce higher stress within the soft tissues.

The results in Chapter 5 indicated that the inner tissue stresses were gradually decayed from the periphery to the center. The higher stresses occurred at the superficial venous walls (GSV and SSV) than those applied to deep venous wall (PV). Correspondingly, the higher venous velocity occurred at GSV and SSV than those applied to PV. It can be seen that in this study, the venous velocities were related with the stresses exerted on the venous wall as well as the interface pressure exerted on the skin, which consistently reflects the simulated pressure function of the ECSs in the previous Chapters.

The venous flow velocities were largely depended upon the tissue stresses and the pressure levels applied by ECSs. The simulation results in Chapters 3 and 5 indicated that the interface pressure were influenced by the mechanical properties and strains of ECS fabrics, and tissue properties of the applied body. The ECSs with greater Young's modulus and higher ECS strain produce higher interface pressures and tissue stresses when being applied at the soft tissues with higher stiffness. In this study, the simulated AVF velocities of the studied veins (SSV, GSV, and PV) under the application of ECSs with Class III were greater by 4% than those by using ECS with Class-I for both two studied subjects, and the simulated AVF velocities of the studied veins with Class-I ECS were greater by 3% than those without using ECSs. The details are shown in Figures 6.7.

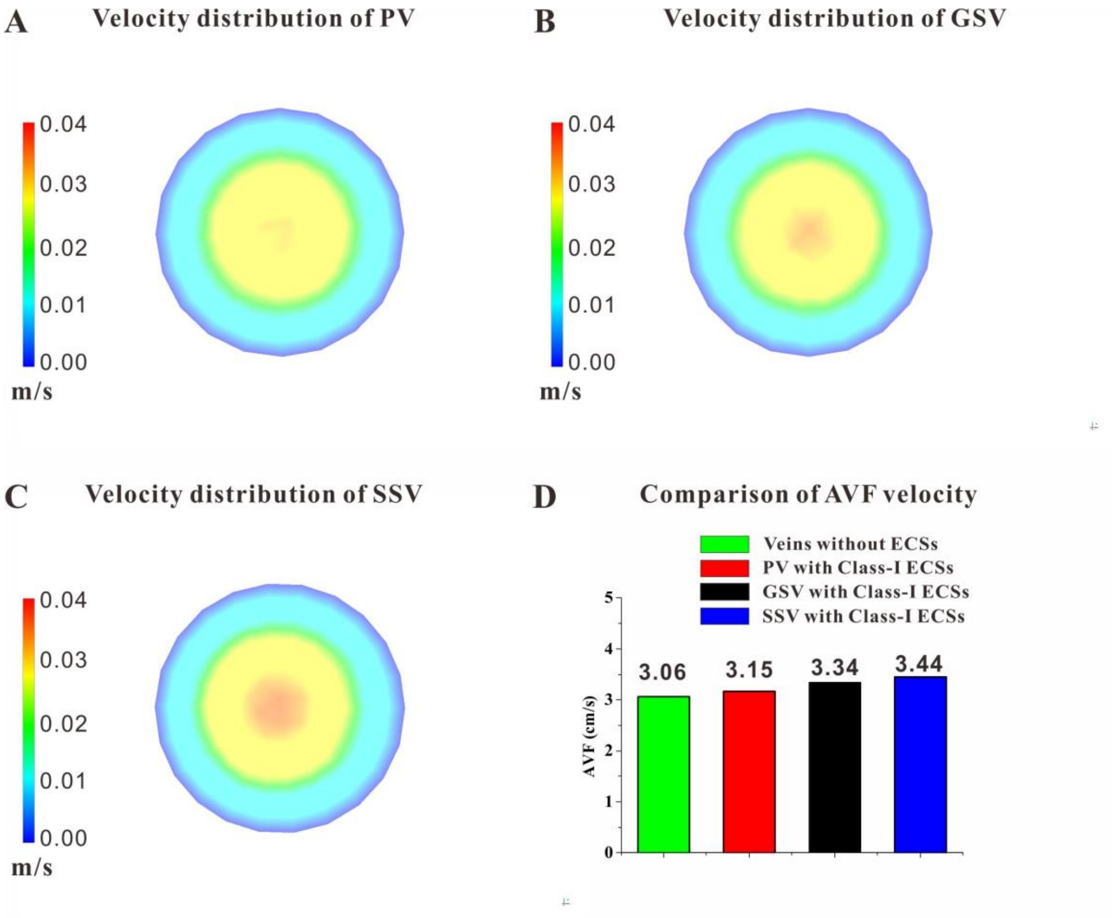

Figure 6.5 The AVF velocities at the pressure outlet for subject 1 (female), including the velocities distribution at (a) the PV, (b) the SSV; (c) the GSV; and (d) comparison AVF velocities among different veins under action of ECSs with Class I.

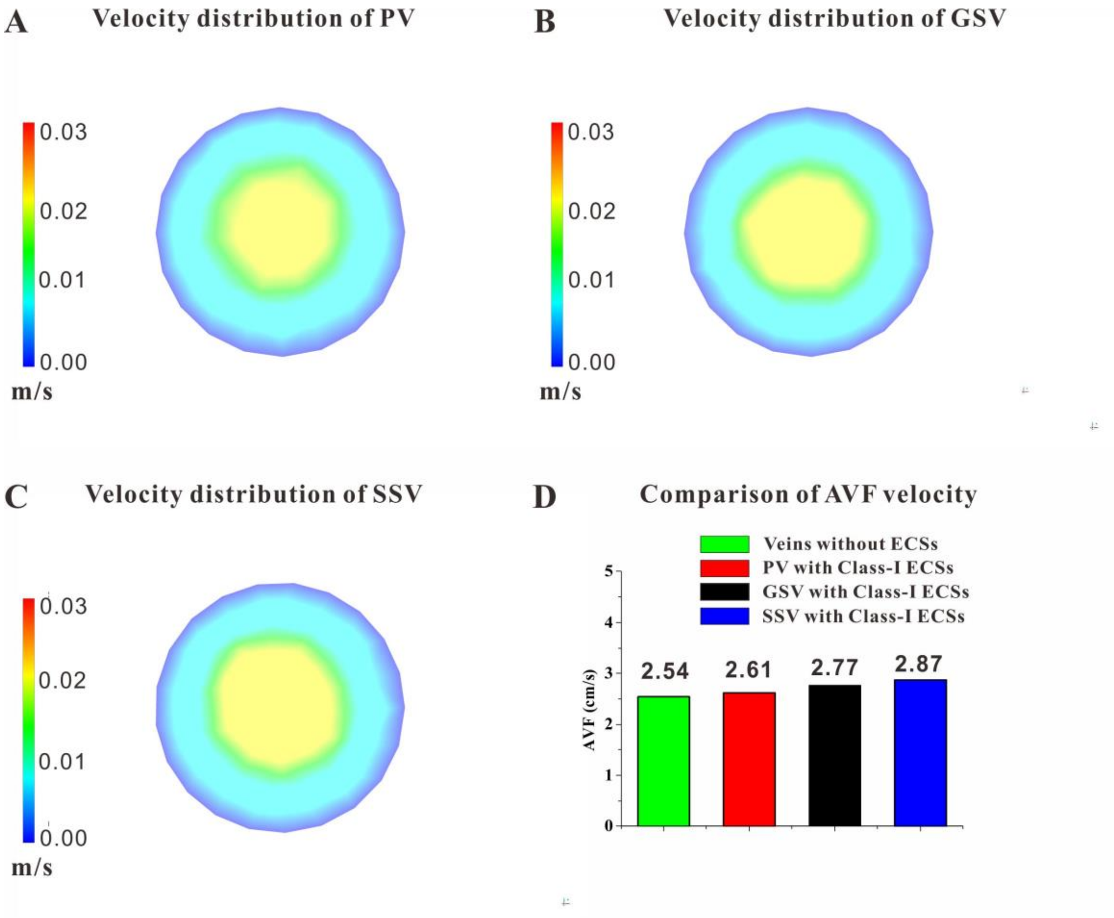

Figure 6.6 The AVF velocities at the pressure outlet for subject 3 (male), including the velocities distribution at (a) the PV, (b) the SSV; (c) the GSV; and (d) comparison AVF velocities among different veins under action of ECSs with Class I.

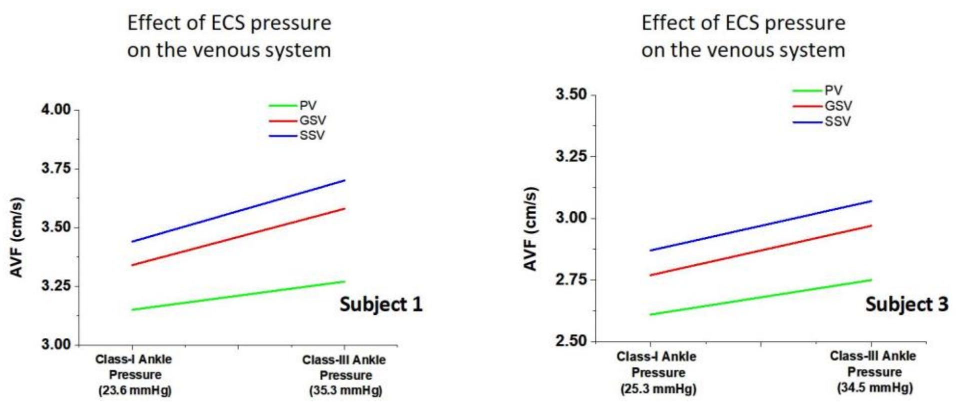

Figure 6.7 The effects of interface pressure by ECSs with different pressure levels on the corresponding AVF velocities of the three studied veins (PV, SSV, and GSV).

6.3.2 Validation of the Built FSI Leg-Tissue-Vein System

Experimental measurements on the venous flow velocities of POVs were conducted by using the Doppler ultrasound tester (Tabata, et al. 2003) when applied the studied ECSs with different mechanical properties and pressure levels onto the lower limbs. The simulated and experimental lower limb from the same subject was consistent in morphologies to maintain a comparable measurement status. The deviations between the simulated and tested venous velocity were analyzed to verify the built subject-specific FSI leg-tissue-vein models (Fig. 6.5-Fig. 6.8), thus understanding the hemodynamic responses of venous system towards ECS pressure when being applied to the user body.

Table 6.2 presented the comparison between the measured and the simulated AVF velocities at the PV outlet beneath ECSs with Classes I and III, respectively. The DROs between the simulated and the measured AVF velocities were approximately 0.96 % and 22.4 % when Class-I ECS and Class-III ECS were applied for subject 1, respectively, and 6.7 % and 2.6 % when Class-I ECS and Class-III ECS were applied for subject 3, respectively. Most of the measured venous velocities presented agreement with the simulated ones, which shows the usability of the developed FSI model to reflect effects of ECSs on the tissue-vein system.

The caused DROs could be resulted from several aspects, (i) the simulated average venous flow velocities cannot fully reflect unstable venous flow in real situation; (ii) the tissue biostructures are more complex in the real situation than the simulated ones where the assumed homogenous soft tissues could not reflect the heterogeneous tissue stiffness and their uneven distributions.

Table 6.2 Comparison between the simulated and measured AVF velocities induced by ECSs with Classes I and III.

Subjects	Without ECS	With ECS (Class-I)		DROs	With ECS (Class-III)		DROs
		Measured	Simulated		Measured	Simulated	
Subject 1	3.06	3.12 (+2.0 %)*	3.15 (+3.0 %)*	0.96 %	3.5 (+14.4 %)*	3.27 (+7.0 %)*	6.6 %
Subject 3	2.54	3.36(+34.0 %)*	2.62 (+3.1%)*	22.4 %	2.67 (+5.1 %)*	2.75 (+7.1 %)*	2.6 %

*compared with the AVF velocities without ECS fabrics.

6.4 Summary

In this Chapter, the venous flow velocities induced by the ECSs with different pressure classes and materials' mechanical properties have been objectively measured and numerically analysed. The simulated results indicated that the AVF velocities slightly increased by 3% and 7% with the usage of Class-I and Class-III ECSs, respectively. And the AVF velocities increased by approximately 4% with the usage of Class-III ECS compared to the status with Class-I ECS. The built FE-FSI coupling models enhanced our understanding of effects of ECSs on interfacial pressure, stress transmission, and correspondingly caused hemodynamic responses. The quantitative analysis showed the relationships among these biomechanical performances of the lower limbs and the physical-mechanical properties of the ECSs. The results contributed to analysis in depth the treatment mechanisms of ECSs in CVI therapy.

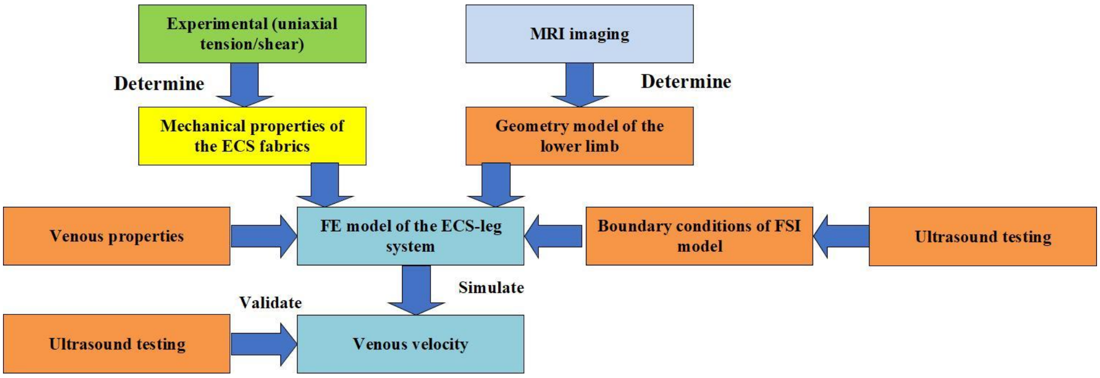

Figure 6.8 Framework of the studies in Chapter 6.

CHAPTER 7 SUBJECTIVE RESPONSES TOWARDS FUNCTIONAL PRESSURE OF ECSs

7.1 Introduction

The comfort characteristics of ECS products are highly important in medical treatment and user compliance (Lin, et al. 2011). Previous studies reported that the frequencies of the noncompliance could be due to ‘uncomfortable’ (49.4%), ‘difficult to put on’ (34.5%), ‘itching feeling’ (21.5%), and ‘unattractive aspects’ (19.8%) (Ayala, et al. 2019). The uncomfortable feeling is the main reason to cause noncompliance of the ECSs where the patients feel stuffy, painful, and sore in practical wear, thus influencing the final therapy effects. Therefore, it is necessary to assess the subject responses towards our developed ECSs pressure function. The frictional force occurring between the ECS and lower limb is a kind of tangent forces, which influence the wearing easiness ECSs; while interface pressure applied by the ECSs is a normal force which more relates to the wearing comfort and treatment effectiveness.

Considering the elderly people commonly suffer from CVI problems more than younger ones (Olsen, et al. 2019), in this Chapter, the wearing comfort of ECSs were assessed by conducting subjective questionnaire surveys through wear trials when nine elderly people being under two different postures (standing and sitting). The interface pressure between the ECSs and the lower limbs were measured using the flexible pressure sensor probe with a diameter of 5 cm and a thickness of 0.2mm

(PicoPress, Microlab Elettronica Sas, Italy; pressure range: 0-189 mmHg; deviation within ± 1mmHg). The results on the subjective comfort and objective pressure testing can build quantitative and qualitative relationships between the mechanical function and user comfort perception in the use of the studied ECSs, thus obtaining a more comprehensive understanding of the ECSs for performance optimization.

7.2 Assessment Methods

7.2.1 Subject Recruitment

The nine elderly subjects (6 females and 3 males with a mean age 62.67 ± 4.23 years) were recruited. Among them, four healthy female subjects, one female subject with heart disease, hypertension, and diabetes, and one female subject with varicose veins; two healthy male subjects, and one male subject with diabetes. All subjects were informed of the objective experimental protocol before signing an informed consent document approved by The Hong Kong Polytechnic University's ethics subcommittee for use on human subjects in research.

The studied ECSs with five difference sizes (S, M, L, XL, and XXL) covering three different pressure classes (I, II, and III) were prepared. Table 7.1 shows the developed ECS size chart for different body dimensions based on our previous related studies on anthropometric survey for Asian users (Liu, et al. 2019). Based on the anthropometric test and Table 7.1, six subjects fitted M size ECS fabrics, one subjects fitted with L size ECS fabrics, and one subject fitted with XXL size ECS fabrics.

Table 7.1 Size chart used in ankle and calf parts.

Leg circumference (cm)	S	M	L	XL	XXL
Ankle	17-19	19-21	20-22	21-23	23-25
Calf	24-27	27-29	28-31	29-32	32-35

7.2.2 Assessment of Subjective Comfort Perception

The prepared questionnaire included three parts. (i) The first part was on basic personal information of the subjects (age, gender, leg circumference, and leg height) and their health situation, (ii) the second part was on the interface pressure measurement in standing and sitting postures, and (iii) the third part was on the survey of comfort characteristics of the subjects when being standing and sitting postures by wearing ECSs with Classes I, II, and III (Fig. 7.1). Before wear trials, all the ECS samples were conditioned in a standard environment with 21± 1°C temperature, 65±2 % relative humidity (ASTM D1776–04) for 24 hours to achieve an equilibrium status prior to use. In the interface pressure measurement, the same testing methods were applied as described in Chapter 5, which conducted by using an air-filled pneumatic pressure-sensing system (PicoPress, Microlab Elettronica Sas, Italy; pressure range: 0-189 mmHg; deviation within ± 1mmHg; sensing probe: 5 mm in a diameter and 0.2 mm in a thickness) (Liu, et al. 2019). Three times at each region of the studied sixteen points (i.e., four directions: anterior, posterior, medial, and lateral; four heights: ankle, brachial, calf, and knee). For the comfort studies, all the subjects were required to keep the standardized standing and sitting postures (Huang, et al. 2017); meanwhile, the subjects were asked to mark their comfort feeling towards these studied regions along and around the lower limbs. In general, every subject estimated the comfort level at a total of 32 regions, including 16 regions in standing and 16 regions in sitting. The experimental process was shown in Fig 7.2.

A Likert-scale is a kind of psychological response scale, which has been widely used in questionnaires and survey research (Lyndon, et al. 2019). In this study, a five-point Likert-scale (5: extremely comfort; 1: extremely discomfort) was applied to determine the perceived comfort level (Fig. 7.1). The experimental data were applied to analyze the pressure comfort function via the statistical methods (correlation coefficient analysis and significant difference analysis).

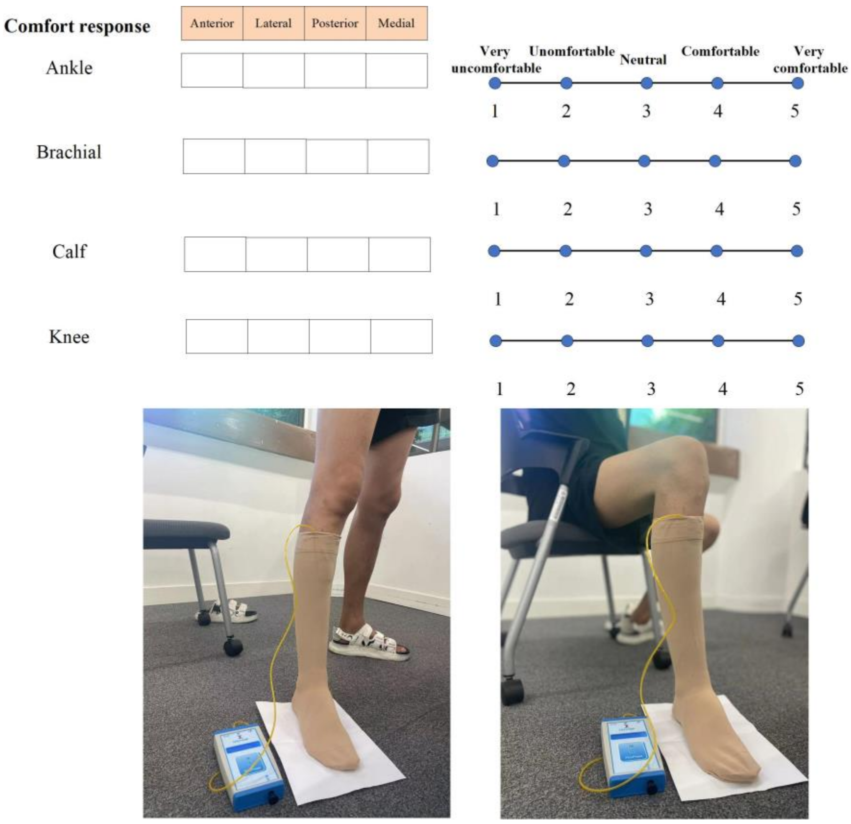

Figure 7.1 Subjective assessment scale on wearing comfort (1): very discomfort; (2): discomfort; (3) neutral (4) comfort; and (5) very comfort).

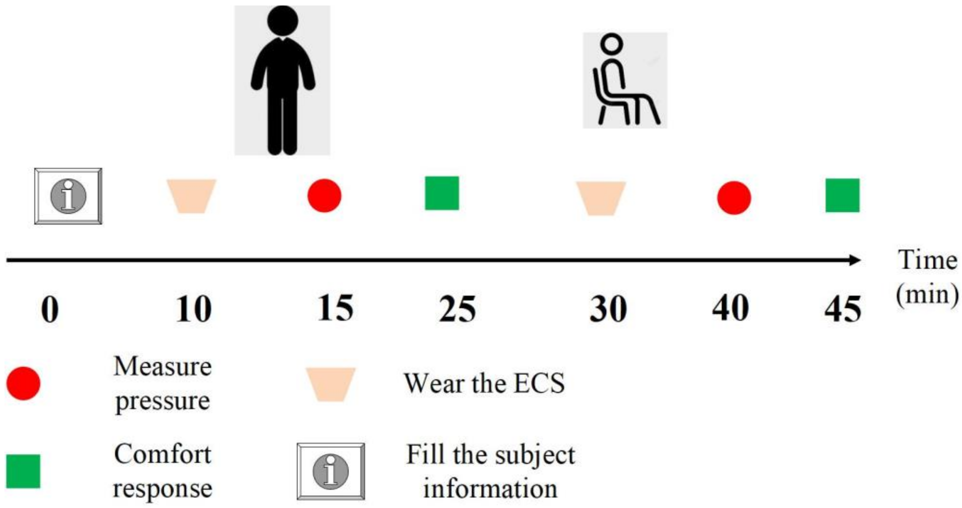

Figure 7.2 Experimental process.

7.3 Results and Discussion

7.3.1. Comfort Assessment under the Applied Compression

Fig.7.3 presents the results on the average comfort evaluation towards 16 testing positions along and around the lower limbs, as well as the corresponding interface pressure values of the studied nine subjects when being worn ECSs with Classes I, II, and III, under sitting and standing positions, respectively.

Class-I

a

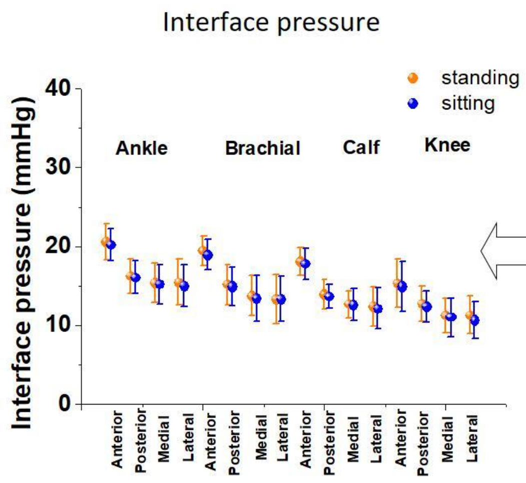
Interface pressure
standing
sitting
Interface pressure (mmHg)
Ankle
Brachial
Calf
Knee
Anterior
Posterior
Medial
Lateral

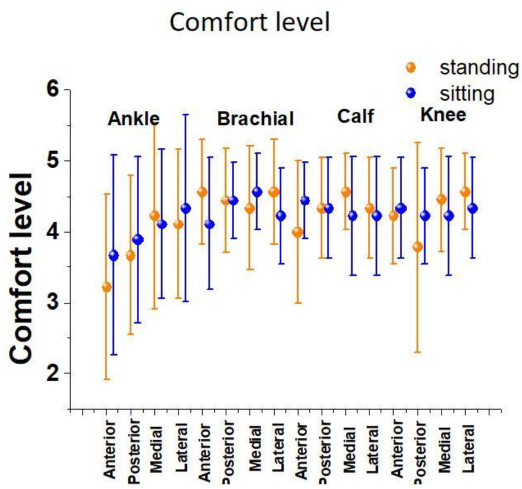
Comfort level
standing
sitting
Comfort level
Ankle
Brachial
Calf
Knee
Anterior
Posterior
Medial
Lateral

b

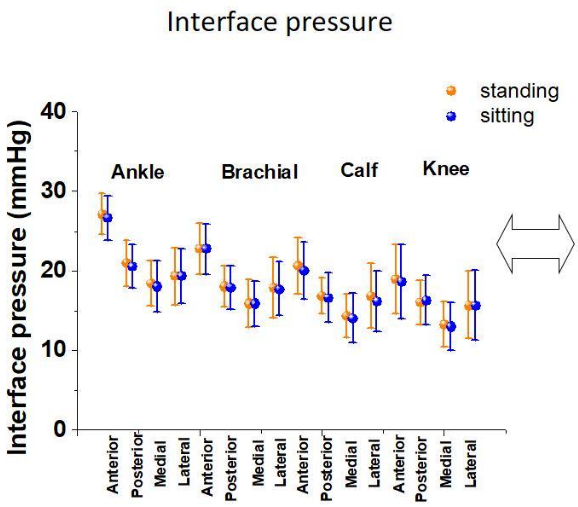
Interface pressure
standing
sitting
Interface pressure (mmHg)
Ankle
Brachial
Calf
Knee
Anterior
Posterior
Medial
Lateral

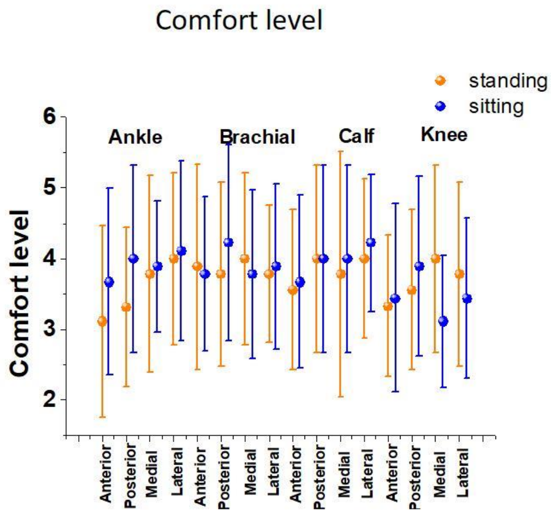
Comfort level
standing
sitting
Comfort level
Ankle
Brachial
Calf
Knee
Anterior
Posterior
Medial
Lateral

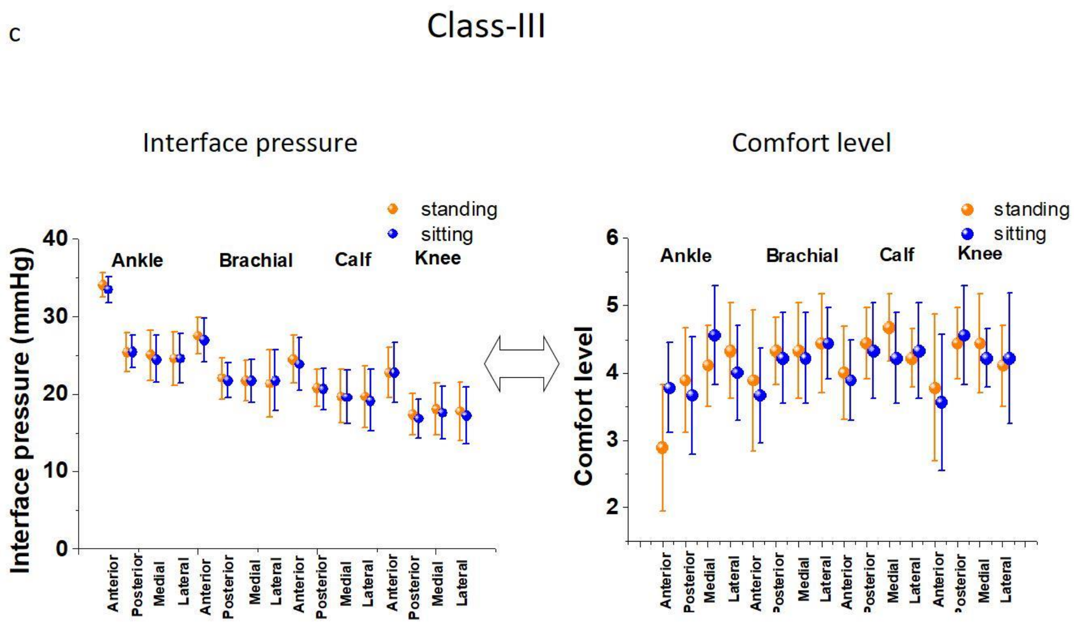

Figure 7.3 The detected subjective comfort levels under the applied interface pressure values at the sixteen specific regions along and around the lower limb when being worn ECSs with (a) Class-I, (b) Class-II; and (c) Class-III.

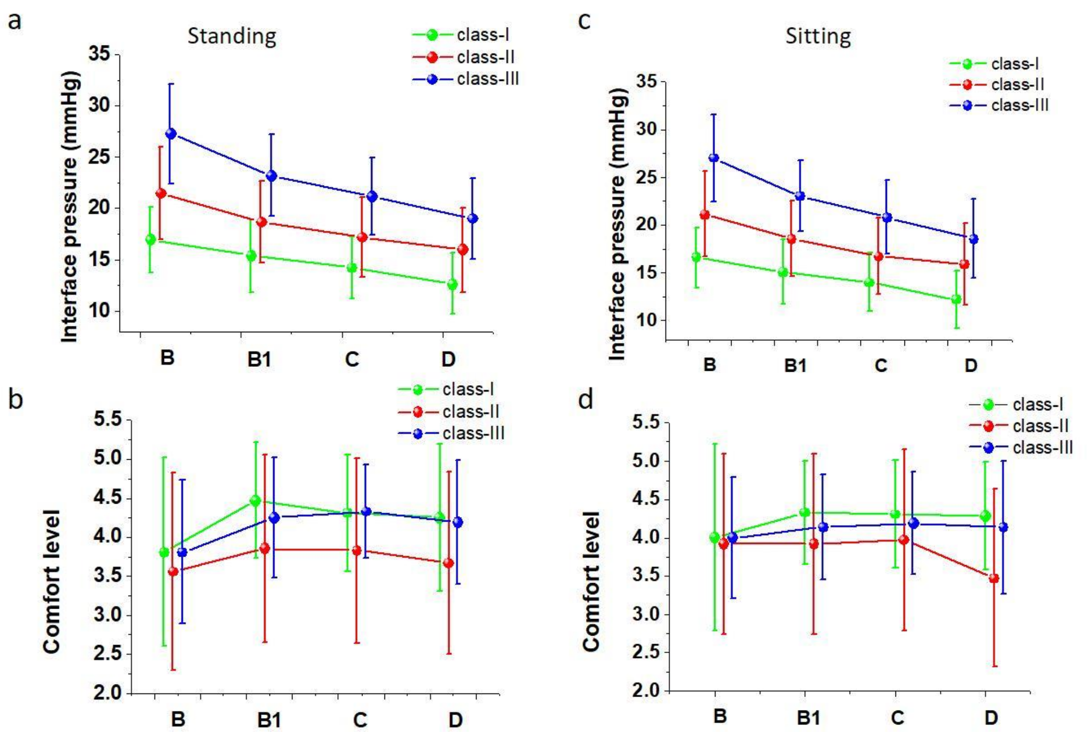

Figure 7.4 The overall interface pressure and comfort level induced by the studied ECSs along the lower limb longitudinally at the (a-b) standing and (c-d) sitting positions.

It can be seen that the measured pressure profiles for ECSs with Classes I, II, and III presented a degressive gradient trend from the ankle (B) to the knee (D), presenting a required therapeutic gradient compression effects, where the pressure gradient ratios from the ankle (B), brachial (B1), to the calf (C) were 100 %, 83.9 %, and 77.8 % for the Class-I ECS; 100 %, 84.4 %, and 76.0 % for the Class-II ECS; and 100 %, 82.3 %, and 74.3 % for the Class-III ECS, respectively, which follows the pressure gradients as indicated by RAL-GZ 387/1 standard.

The potential reason for pressure differences could be the differences in muscle stiffnesses existed among the studied subjects, and the irregular leg shape cross-section may vary the contract conditions between the ECSs and the skin surface. The body postures influenced the skin pressure values. The average interface pressure in standing posture was 18.6 ±5.5 mmHg of all of testing pressure which were slightly greater than those in sitting posture (18.3±5.5mmHg). The interface pressure at anterior point was greater than that at other positions (posterior, medial, and lateral) in both sitting and standing postures, which was similar with the simulated results as shown in Chapter 5. This is mostly due to less muscles distributed at anterior point.

In general, the subjective comfort level ranged from 3 to 4.5 for all the studied ECS fabrics, among which comfort level in the sitting posture (4.06±1.0) was slightly higher than those in the standing posture (4.03±1.0). These results indicated that our prepared ECSs brought the subjects comfortable perception in use generally. However, some discomfort response appeared in the anterior site for individual subjects due to relatively higher pressure occurred at anterior side due to less muscle distributes at the anterior side. In addition, it can be seen that the subjects feel more comfortable when ECSs with lower pressure levels were applied than those applied by ECSs with higher pressure level.

7.3.2. Relationships between the Subjective Comfort and the Applied Pressure

Figure 7.5 indicated that there existed significant difference between the standing and sitting postures towards the comfort perception and pressure performances. It can be seen that the no significant difference on the comfort level between the standing and sitting position (p>0.05), and no significant difference towards comfort level among ECSs with three different classes. And the significant difference (p<0.05) towards interface pressure among ECSs with three classes level, among them, the extremely significant difference (p<0.01) towards interface pressure level among ECSs with Class-I and Class-III.

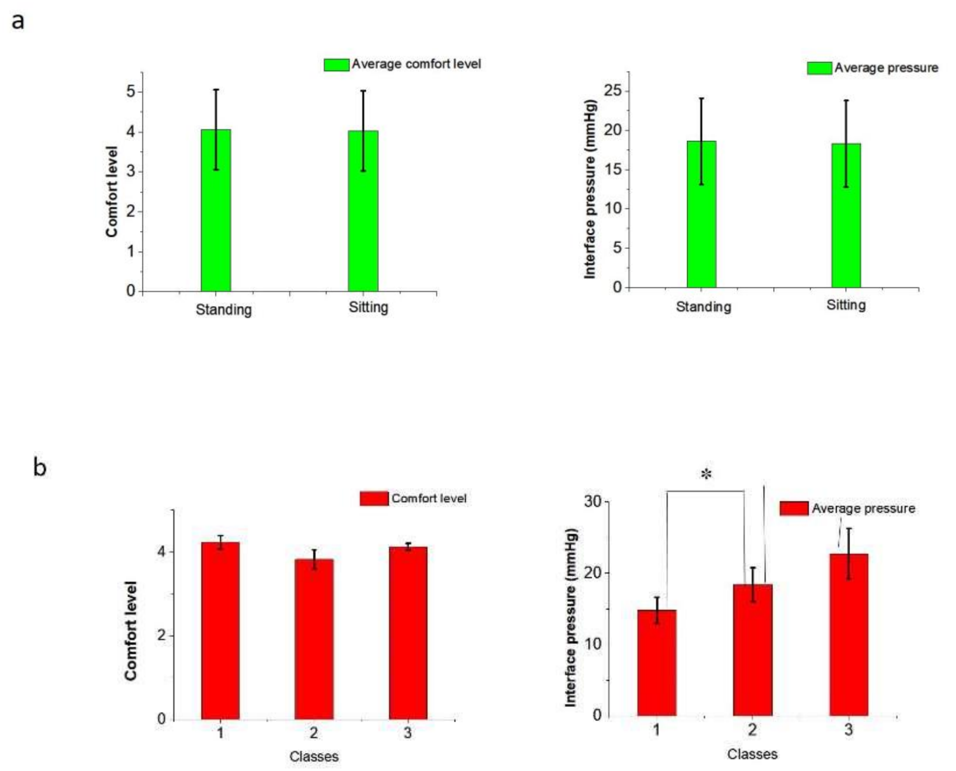

Figure 7.5 (a) The comfort level and interface pressure exist significant difference between the standing and sitting postures; (b) the comfort level and interface pressure exist significant difference among three classes (*: $p<0.05$ (significant difference); **:$p<0.01$ (extremely significant difference)).

The qualitative relationship between the pressure and comfort responses has been established based on the subjective and objective studies by applying a correlation analysis. It can be seen that there existed a negative correlation between the comfort level and interface pressure for ECSs application generally. That is, the discomfort response occurred at the higher-pressure position.

Table 7.2 Correlation coefficients between the subjective comfort level and the applied interface pressure of ECSs under different postures.

Classes of ECSs	**Standing**	**Sitting**
Class-I	-0.54	-0.71
Class-II	-0.47	0.56
Class-III	-0.80	-0.83

Based on the above analysis, the major findings are as follows,

(i) there was no significant difference ($p > 0.05$) on the comfort level and interface pressure performance between the standing and sitting postures among the studied elderly subjects.

(ii) there was no significant difference ($p > 0.05$) towards comfort level among ECSs with three different classes (the studied ECSs brought the comfort sensation to the studied subjects).

(iii) significant difference ($p < 0.05$) on the interface pressures existed among the ECSs with three different classes.

It can be seen that the changes of the body postures in the standing and sitting in use may not influence the comfort and pressure performances of ECSs; while the ECSs with higher pressure levels could influence users' comfort feeling. ECS with lower pressure values could be more acceptable for the end users to keep use for treatment.

7.4 Summary

In this Chapter, the comfort level and correspondingly applied pressure magnitudes were estimated when nine subjects applied ECSs with three different pressure levels based on RAL-GZ 387/1 standard (Class I: 18-21 mmHg; Class I: 23-32 mmHg; Class III: 34-46 mmHg) under two different body postures (sitting and standing). The subjective comfort perception was investigated by using the subjective questionnaire survey combined with the statistical analysis and interface pressure measurements using flexible pressure sensor probe. The results showed that there was no significant difference towards the comfort responses and pressure profiles when being sitting and standing postures with use of ECSs. With increase of pressure classes, the comfort perceptions would reduce, while the general comfort range sustained comfort level (3-4.5) corresponding to the moderate to comfortable level, indicating that the designed ECSs achieved the proper pressure levels and comfortability in user application.

CHAPTER 8 OPTIMIZATION AND IMPROVEMENT OF ECS DESIGN FOR END USE

8.1 Introduction

In the ECS-leg system, the parameter optimization is commonly used to determine an optimum geometric model and material properties with proper mechanical-physical characteristics. The results of the parameter optimization facilitate users or physicians to select ECSs with fitted sizes for achieving targeted pressure levels in treatment. The existing studies mainly focused to optimize the parameters via response surface model (RSM) based on the FE simulation results (Lin, et al. 2011); where this method focused on a group number to achieve a special pressure rather than pressure range. Moreover, no systematic analysis to detect what parameters was directly correlated with the interface pressure (or more sensitive to the interface pressure), and few studies systematically analyse how to set the sensitive parameters ranges (e.g., ECS sizes, mechanical properties such as Young's modulus, Poisson's ratio, and shear modulus, and users' leg circumferences) to achieve the expected pressure levels combined with FE simulation system.

In this Chapter, an analytical model combined with the Sobol algorithm was developed to determine the sensitive parameters that affect the interface pressure values. After that, a parameter optimization system was constructed through formulating the relationships among the sensitive parameters (leg geometry models, ECS fabrics mechanical properties, and ECS dimension design) via FE parameter set module based on the meshing, boundary conditions, and contact settings in Chapter 3, thus guiding to design the suitable ECS fabrics with fitted sizes for special end users to achieve the target pressure levels.

8.2 Study Methods

8.2.1 Determination of Sensitive Parameters Influencing Pressure Levels

Analysis of Interactive Factors within the ECS-Leg System

The interface pressure between the lower limb and ECS fabrics has been analyzed and simulated in Chapter 3 and Chapter 5 by using FE model. However, the interactive factors cannot be obtained by the FE model quantitatively. To obtain the interactive factors in the ECS-leg system, an analytical model was constructed based on the mechanical equilibrium equation to quantitatively analyze the relationship among the determined interactive parameters and pressure values.

Sensitive analysis studies the impact of certain changes in relevant factors on an important indicator or a group of indicators from the quantitative analysis (Saltelli, et al. 2006). In the ECS-leg system, sensitive analysis can be applied to quantitatively analyse the effects of ECS parameters changes on the pressure values, to provide an guidance to optimize pressure performances through the determined sensitive parameters.

In the existing studies, Laplace's law is commonly applied to analyse the interface pressure between the soft tissues and ECSs (Basford, et al. 2002). However, Barhoumi et al. found that the predicted interface pressure may not be accurate considering the errors caused by the tension measurement (Barhoumi, et al. 2020). Hence, a modified Laplace's law was developed to optimize the interface pressure computation through determining the relationships between the tension and stress of the ECS fabrics. Whereas this modified Laplace's Law can only reveal a fundamental relation between body dimension, fabric thickness, the applied extension, and corresponding Young's modulus, but does not involve the Poisson's ratio properties of the ECS materials in the simulation, which would influence the prediction precision of the pressure values.

Therefore, in this study, a new 3D FE model of the ECS-lower limb system has been developed in Chapters 3 and 5 for the rigid leg and soft leg. The developed FE model simulated the interface pressure profile and reveal the working mechanisms behind the interactions of the two bodies (ECS and lower limb). However, the quantitative relationship among the materials, pressure, and size fitting parameters still cannot be obtained. Thus, a new analytic modelling was developed in this Chapter through a sensitive analysis.

Considering the tension forces produced by the ECS around the cross-sectional lower limb dominate the interface pressure (the normal force) function during the dynamic wear, Fig. 8.1 illustrates the normal forces exerted by the ECSs to the leg tissues. The mechanical balance of the ECS in the arbitrary cross-section can be expressed based on the mechanical balance analysis,

$$\begin{aligned}&\frac{\partial\sigma_\rho}{\partial\rho}+\frac{1}{\rho}\frac{\partial\tau_{\varphi\rho}}{\partial\varphi}+\frac{\sigma_\rho-\sigma_\varphi}{\rho}+f_\rho=0\\&\frac{1}{\rho}\frac{\partial\sigma_\varphi}{\partial\varphi}+\frac{\partial\tau_{\rho\varphi}}{\partial\rho}+\frac{2\tau_{\rho\varphi}}{\rho}+f_\varphi=0\end{aligned}\tag{8.1}$$

where σ_ρ and σ_φ are the normal stress of the ECS fabrics along the radial (thickness) and the circumferential (course) directions, respectively; $\tau_{\rho\varphi}$ and $\tau_{\varphi\rho}$ denote the shear stress of the ECS fabrics within the course-thickness (*x*-*z*) plane (Fig. 8.1); and f_ρ and f_φ are the volume forces along the radial (thickness) and the circumferential (course) directions, respectively. Based on the Hooke's Law and plane stress state, the relationship between the stress and strain of the ECS fabric can be expressed as

$$\varepsilon_\rho = \frac{1}{E}(\sigma_\rho - v\sigma_\varphi);\ \varepsilon_\varphi = \frac{1}{E}(\sigma_\varphi - v\sigma_\rho);\ \gamma_{\rho\varphi} = \frac{1}{G}\tau_{\rho\varphi} \tag{8.2}$$

where E and v are the Young's modulus and Poisson's ratio at the course direction of the ECS fabric, and G is the shear modulus of the ECS fabric within the *x*-*z* plane.

Through the coordinate transversion, the Airy's stress function can be derived as

$$\rho^4 \frac{d^4\Phi}{d\rho^4} + 2\rho^3 \frac{d^3\Phi}{d\rho^3} - \rho^2 \frac{d^2\Phi}{d\rho^2} + \rho \frac{d\Phi}{d\rho} = 0 \tag{8.3}$$

The solution of Euler Equation can be employed to solve Eq. 8.3. Hence, the solution of Eq. 8.3 can be expressed as

$$\Phi = A\ln\rho + B\rho^2\ln\rho + C\rho^2 + D \tag{8.4}$$

where A, B, C, and D are the undetermined coefficients. With consideration of the axial symmetric property of the ECS's shell in the cross-section (Fig. 8.1), the stress component of the ECS fabric can be expressed as

$$\sigma_\rho = \frac{A}{r^2} + 2C;\ \sigma_\varphi = -\frac{A}{r^2} + 2C;\ \tau_{r\varphi} = 0 \tag{8.5}$$

The interface pressure (P) is resulted from the interaction between the ECS and leg tissues. The boundary conditions of the ECS fabric in the interaction with tissues can be expressed as follows,

$$(\sigma_r)_{r=a} = -P;\ (\sigma_r)_{r=b} = 0;\ (\tau_{r\varphi})_{r=a} = 0;\ (\tau_{r\varphi})_{r=b} = 0 \tag{8.6}$$

where P is the interface pressure. Based on the boundary conditions of the ECS fabric, the undetermined coefficients (A and C) in Eq. 8.4 can be computed as,

$$A=\frac{-a^2b^2P}{b^2-a^2};\ C=\frac{Pa^2}{2(b^2-a^2)} \tag{8.7}$$

where a and b are the internal radius and external radius of the ECS shell in the cross-section view (Fig. 8.1).

The stress component of ECS fabrics includes the σ at the thickness and course directions, and the τ within the x-z plane, which can be predicted through substituting Eq. 8.5 into Eq. 8.7. Thus, the stress component of the ECS fabric (shell) can be expressed as

$$\sigma_\rho=-\frac{\frac{b^2}{r^2}-1}{\frac{b^2}{a^2}-1}P;\ \sigma_\varphi=-\frac{\frac{b^2}{r^2}+1}{\frac{b^2}{a^2}-1}P;\ \tau_{r\theta}=0 \tag{8.8}$$

The relationship between the stress and strain properties of the ECS shell can be expressed based on Hooke's Law as follows:

$$\varepsilon_\rho=\frac{1}{E}(\sigma_\rho-\mu\sigma_\varphi);\ \varepsilon_\varphi=\frac{1}{E}(\sigma_\varphi-\mu\sigma_\rho);\ \gamma_{\rho\varphi}=\frac{1}{G}\tau_{\rho\varphi} \tag{8.9}$$

Through substituting Eq. 8.8 into Eq. 8.9, the strain component of the ECSs can be derived as

$$\varepsilon_\rho=\frac{1}{E}(\sigma_\rho-\mu\sigma_\varphi)=\frac{P}{E(\frac{b^2}{a^2}-1)}[1-\frac{b^2}{r^2}+\mu(\frac{b^2}{r^2}+1)];\ \varepsilon_\varphi=\frac{1}{E}(\sigma_\varphi-\mu\sigma_\rho)=\frac{P}{E(\frac{b^2}{a^2}-1)}[\mu(1-\frac{b^2}{r^2})-(\frac{b^2}{r^2}+1)];\ \gamma_{\rho\varphi}=\frac{1}{G}\tau_{\rho\varphi}=0 \tag{8.10}$$

The strain of the ECS is a description of the deformation in terms of relative displacement of the ECS fabric under the stretch. Thus, the relationship between the strain and the deformation (displacement) of the ECS shell can be expressed as

$$\varepsilon_\rho = \frac{\partial u_\rho}{\partial r};\ \varepsilon_\varphi = \frac{u_\rho}{\rho} + \frac{1}{\rho}\frac{\partial u_\varphi}{\partial \varphi} \tag{8.11}$$

Based on the relationship between the strain and the deformation (Eq. 8.11), the material deformation of the ECS shell can be expressed as

$$u_\rho = \frac{1}{E}[-(1+v)\frac{A}{r} + 2(1-v)Cr] = \frac{1}{E}[(1+v)\frac{a^2b^2P}{r(b^2-a^2)} + (1-v)\frac{Pa^2}{(b^2-a^2)}r];\ u_\varphi = 0 \tag{8.12}$$

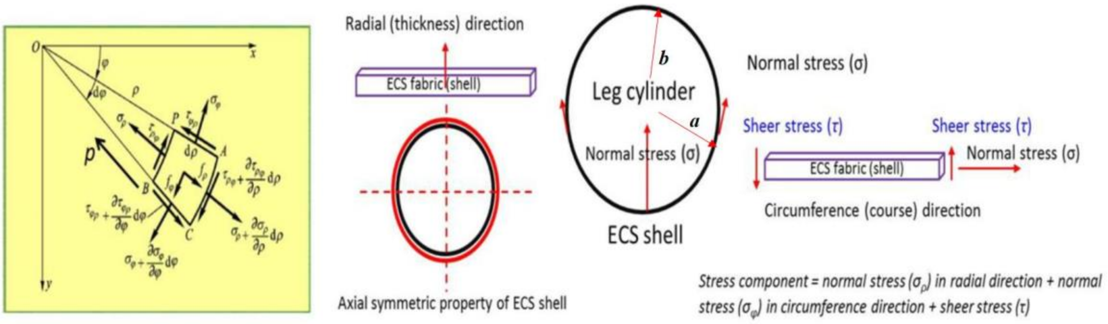

Figure 8.1 The micro-element mechanical balance analysis of the ECS cross section.

Based on Eq. 8.12, the interface pressure (P) between the studied ECS and the contacted tissues can be calculated as follow,

$$P = \frac{((a+h)^2 - a^2)Eu_\rho}{(1+v)a(a+h)^2 + (1-v)a^3} \tag{8.13}$$

Based on the Eq. 8.13, the relationship between the interface pressure and interactive parameters has been conducted, where the interactive parameters included Young's modulus (E), thickness (h), Poisson's ratio (v), deformation/displacement along the course direction (u_ρ), and radius in tubular (a) of the ECS. The interactive parameters would be applied to determine the sensitive parameters in the ECS-leg system by using the Sobol algorithms.

Sobol Algorithms for Determination of Sensitive Parameters

Sobol Algorithms is a global model based on variance decomposition (Nossent, et al

2011), which can be dealt with nonlinear mechanical models to determine the sensitive level (index) to analyze the sensitive parameters which most significantly influence the interface pressure in the ECS-leg system. To obtain the parameter ranges to achieve the target pressure level, the sensitive parameters were input to the optimization system. The first order sensitivity index (S_i) was applied to assess the sensitivity level, where S_i ranges from 0 to 1, and the value of S_i is closer to 1, which means that the corresponding parameter was sensitive parameters to affect the interface pressure. The equation to calculate sensitivity indices is as follow:

$$S_i = \frac{V_{X_i}(E_{X\sim i}(Y|\ X_i))}{V(Y)} \tag{8.14}$$

Based on Eq. 8.13, the following parameters relating to the pressure values were examined for the calculation of the sensitive index: (1) Young‘s modulus (E); (2) Poisson‘s ratio (v); (3) thickness (h); and (4) ECS deformation (displacement) along course direction (u_ρ). Among them, the E and v are the mechanical properties of the ECS fabrics, and h and u_ρ are the geometric properties in the ECS-leg system. To determine the sensitive index of the aforementioned parameters, the parameter range were determined in practice. Based on our previously described methods on the uniaxial tension testing in Chapters 3 and 5, the ranges of interactive parameters (E, v, and h) used in our developed sensitive model were 0.3 to 0.75 MPa, 0.2 to 0.3, and 0.7 to 1 mm, respectively.

In addition, the deformation of the ECS fabrics relates to both leg girth and ECS girth. Ankle section are the key part to be used to classify the pressure level (Class-I: 18 to 21 mmHg; Class-II: 23 to 32 mmHg; and Class-III 34 to 46 mmHg). Thus, in this

Chapter, the ankle size charts of the ECSs applied in the Hong Kong market that fit Asian ankle girth were used as a reference to determine the deformation range of the ECS fabrics (Table 8.1).

Table 8.1 The ankle girths measured based on the size charts of the commercial ECSs sold in Hong Kong market.

Brand	JOBST (US)				JUZO (UK)				
(Country/region)	S	M	L	XL	S	M	L	XL	XXL
ECS girth (cm)	14-16	16.8-19.8	20-22.8	23-26	14-16.6	16.6-19	19-21.6	21.6-24.6	24.6-27.6
Leg girth (cm)	18-21	21-25	25-29	29-33	18-21	21-24	24-27	27-31	31-35

Based on RAL-GZ 387/1 standard, the interface pressure at the ankle part was important to determine the pressure level (Class-I: 18-21 mmHg, Class-II: 23-32 mmHg, and Class-III: 34-46 mmHg), thus, only ankle size of the ECS fabrics was referred in this Chapter to design the ECS fabrics, and other parts were satisfied with the pressure gradients according to RAL-GZ 387/1 standard.

Table 8.2 shows the reported size ranges of the ankle girths from different countries in Asian. For example, for the male Iranian and Malaysian, the ankle girth was 27.9 cm and 26.0 cm, respectively, and for the female Iranian and Malaysian, the ankle girth were 23.9 cm and 24.5 cm for obese group. Based on these data, our selected ankle girth were 22.5 cm for obese group, 20.3 cm for the medium group, and 18.0 cm for thin group. Our developed ECS size at ankle and calf sections was determined based on RAL-GZ 387/1 standard (Medical Compression Hosiery Quality Assurance) and ankle sizes applied in Asian and commercial ECS products, which is listed as follow.

Table 8.2 The ankle girth measured on users among Asian countries/regions based on the public reported data.

	Ankle girth (cm)		
Country/Region	Obese	Medium	Thin
Iran	27.9 (M*)/23.9 (F*)	23.5 (M)/21.3 (F)	20.6 (M)/19.3 (F)

China mainland	-	20.9	-
China Hong Kong	-	21.2	-
Malaysia	26.0 (M)/24.5 (F)	22.6 (M)/20.9 (F)	19.4 (M)/17.8 (F)
Korea	24.1	19.9	16.7
Our developed leg size	22.5	20.3	18.0

M*: Male; F*: Female

Table 8.3 Our developed ECS size at ankle and calf sections.

Determined girth (cm)	S	M	L	XL	XLL
Ankle	15.8	16.6	17.4	18.2	19.0
Calf	22.2	23.2	24.4	25.6	26.6

Based on the Table 8.2 and Table 8.3, the range of u_ρ was 0.5 to 2 cm. Thus, by using the above interactive parameter ranges, the sensitive index can be determined based on Eq. 8.14 (Table 8.4).

Table 8.4 The studied parameters range and corresponding sensitivity index.

Parameters	Parameters range	Unit	Sensitivity index
E	0.3 - 0.75	MPa	0.33
v	0. 2 - 0.3	/	0.02
h	0.7 - 1	mm	0.05
u_ρ	0.5 - 2	cm	0.65

The determined sensitive indexes were 0.33, 0.02, 0.05, and 0.65 for Young's modulus, Poisson's ratio, thickness, and ECS fabrics deformation along the course direction, respectively, where the sensitive indices of the ECS fabrics deformation/displacement (0.65) and Young's modulus (0.33) are greater than those of Poisson's ratio (0.02) and thickness (0.05) based on the determined sensitive indexes.

Therefore, the ECS displacement/deformation (u_ρ) and Young's modulus (E) were the determined sensitive parameters to optimize the sensitive parameter values to achieve target interface pressure level by using FE parameter set module in Chapter 8.2.2.

8.2.2 Optimization of the Determined Sensitive Parameters for Targeted Pressure Levels

Based on the sensitive analysis results, the sensitive parameters (u_ρ and E) were applied to optimize our ECS design and corresponding proper human group users. The ECS displacement/deformation along the course direction wear on the lower limb were effected by ECS size and leg ankle girth. Therefore, ECS Young's modulus, ECS radius, and leg radius as the sensitive parametric variations that influence the interface pressure were input to Ansys workbench parameter set module (v19.2, ANSYS, Pennsylvania, Pittsburgh, USA). The parameter set module could be applied to study and optimize product performance under different design schemes by changing the geometric properties (leg and ECS circumference and thickness) and mechanical properties (Young's modulus, Poisson's ratio, and shear modulus), mesh parameters (mesh size), and boundary conditions, etc.

The setting of geometry model, meshing construction, and boundary conditions of the FE optimization ECS-Rleg system was referred to Chapter 3. The optimization pressure was based on RAL-GZ 387/1 standard, e.g. the Class-I interface pressure ranges from 18 to 21 mmHg; Class-II interface pressure ranges from 23 to 32 mmHg; and Class-III interface pressure ranges from 34 to 46 mmHg, respectively. The E of ECS was determined based on uniaxial tension testing by using our developed ECS fabrics with the same yarn materials in Chapter 5. The E of Class-I ECS fabrics ranges from 0.3 to 0.45 MPa; the E of Class-II ECS fabrics ranges from 0.45 to 0.6 MPa; and E of Class-III ECS fabrics ranges from 0.6 to 0.75 MPa for all sizes of the ECS fabrics, respectively. The upper and lower limits of ECS size was referred from the parameter range in Chapter 8.1.

Based on the determination ECS sizes, Young's moduli of the ECS fabrics, and the

RAL-GZ 387/1 pressure class standard, the leg circumference and leg size chart at ankle and calf sections were optimized via Ansys workbench parameter set module for further design optimization.

8.3 Results and Discussion

Since the ankle section was the key position to determine the Class level, and the calf section was normally the widest section in the knee-length ECS design, Fig. 8.2 showed the optimized ECS size chart at calf and ankle sections and corresponding human groups based on the parameter optimization methods.

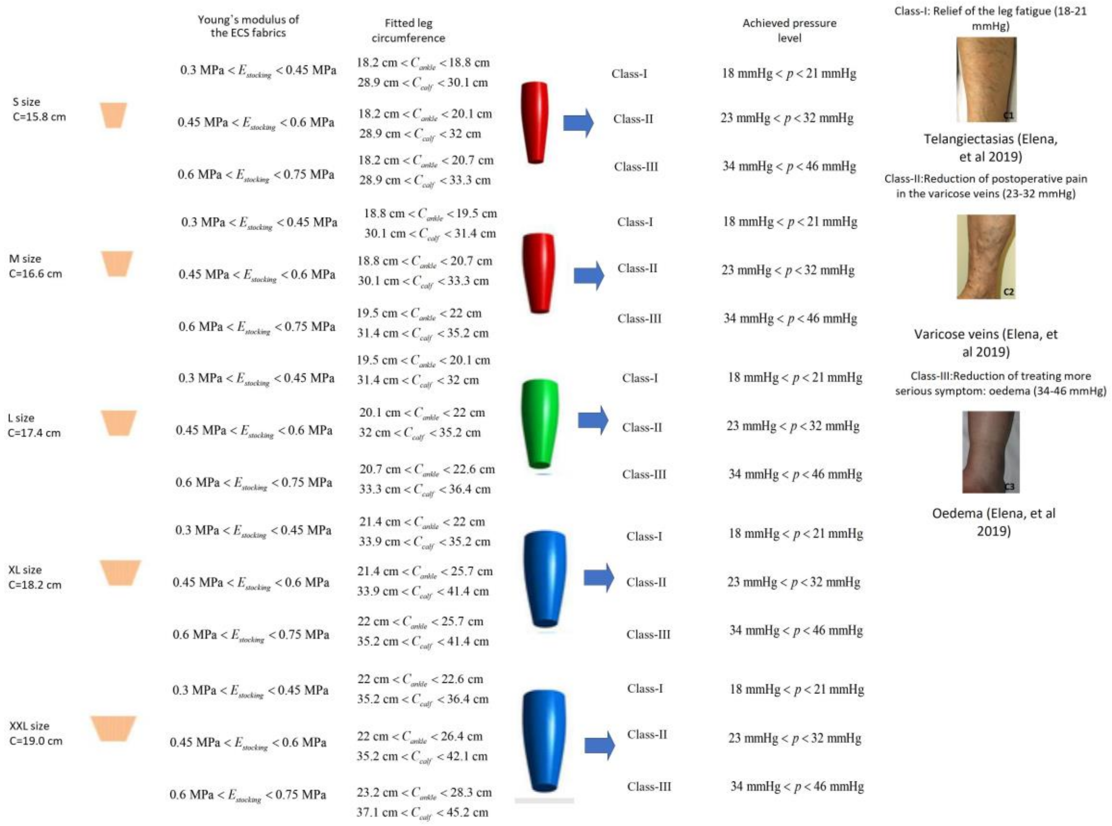

Figure 8.2 The optimized leg circumference, and corresponding ECS Young's modulus and size to fit the target pressure level.

It can be seen that our designed ECSs with S, M, L, XL, and XXL sizes for achieving

Class-I pressure level (18-21 mmHg) could fit the human group with the ankle circumference from 18.2 to 18.8 cm, from 18.8 to 19.5 cm, from 19.5 to 20.1 cm, from 21.4 to 22 cm, and from 22 to 22.6 cm, respectively, for relief of leg fatigue, tiredness, and heaviness.

Correspondingly, our designed ECSs with S, M, L, XL, and XXL sizes for achieving Class-II pressure level could fit the human group with the ankle circumference from 18.2 to 20.1 cm, from 18.8 to 20.7 cm, from 20.1 to 22 cm, from 21.4 to 25.7 cm, and from 22 to 26.4 cm, respectively, for prevention or treatment of CVI or the reduction of postoperative pain in the primary varicose treatment. Similarly, our designed ECSs with S, M, L, XL, and XXL size for achieving Class-III pressure level could fit the human group with the ankle circumference from 18.2 to 20.7 cm, from 19.5 to 22 cm, from 20.7 to 22.6 cm, from 22 to 25.7 cm, and from 23.2 to 28.3 cm, respectively, for treatment of CVI or the reduction of postoperative pain in the primary varicose treatment as well as relieving CVI symptoms or treating more serious symptoms such as lymphatic edema.

Figure 8.3 showed the leg size chart based on our optimization results and comparison with our experienced results. Most of the optimized leg size data presented agreement with the experienced leg sizes, especially for Class III, which demonstrated the applicability of the developed optimization method in leg size assessment that facilitates the selection of ECSs for pressure treatment.

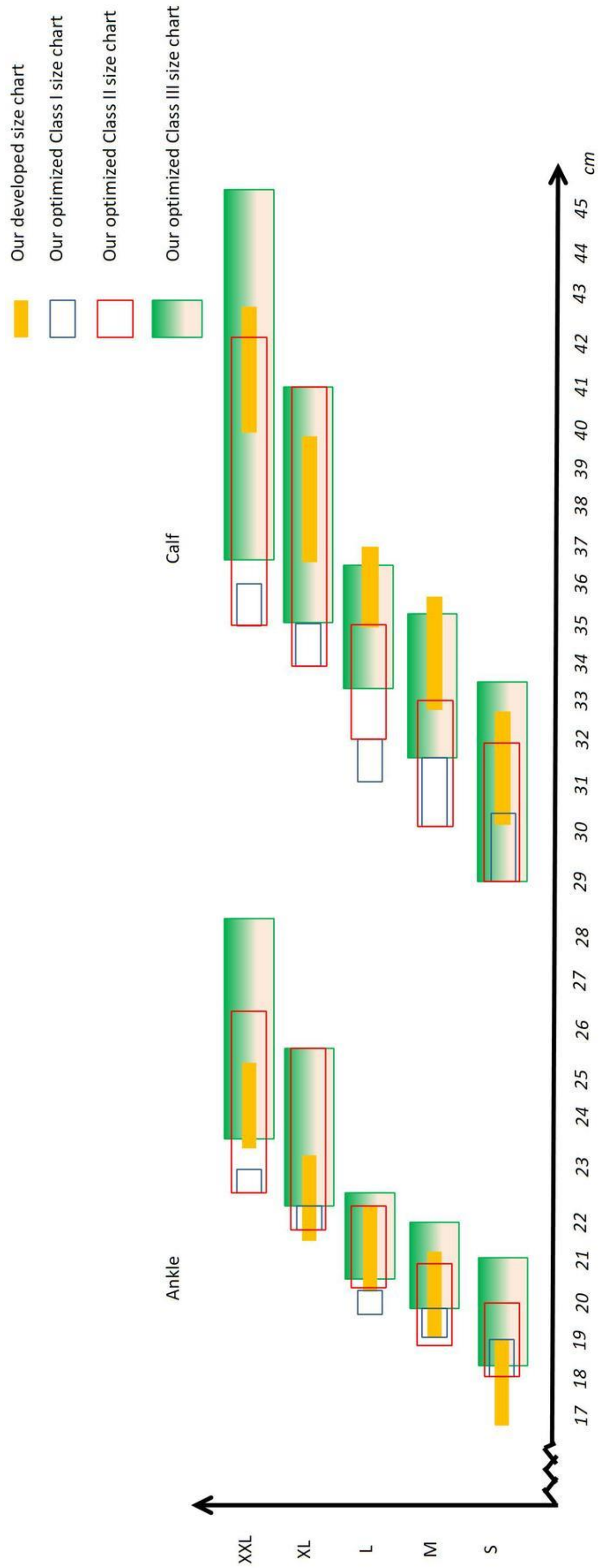

Figure 8.3 The optimization ECS size chart.

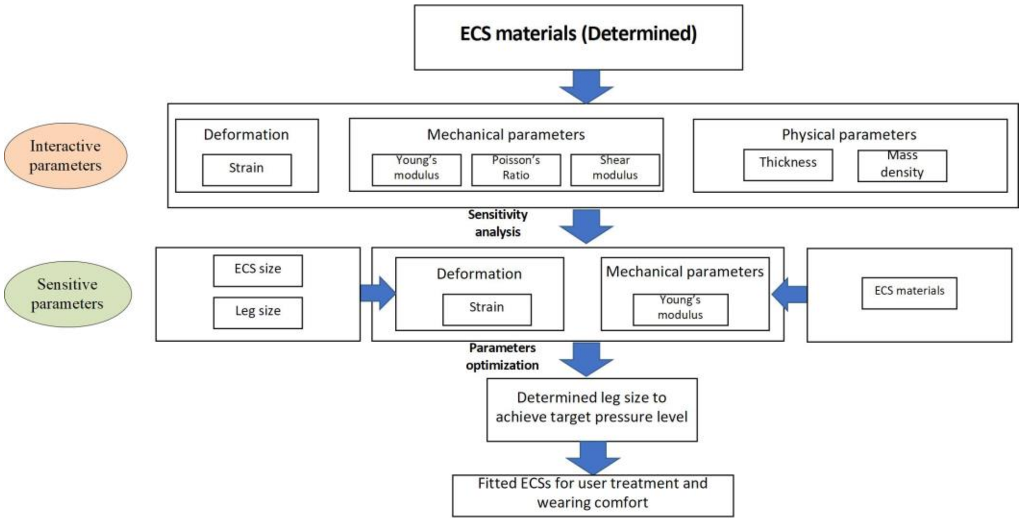

Figure 8.4 Framework of the Chapter 8.

8.4 Summary

In this chapter, a parameter optimization method in the ECS-leg system has been developed to optimize design the ECS fabrics to fit different human groups for achieving multiple pressure levels based on our developed simulation methods in Chapter 3 and Chapter 5. To determine the sensitive parameters that influence the pressure levels, an analytic model was proposed to construct the relationship among the interface pressure, ECS mechanical properties, and fabrics deformation along the course direction based on Sobol method. The determined sensitive parameters (ECS fabrics deformation and mechanical properties) were input into the Ansys workbench parameter set module to optimize ECS deformation and Young's modulus range for achieving the target pressure levels. Based on the optimized parameter ranges for ECS deformation and Young's modulus, a new ECS fitting system has been constructed to offer guidance for ECS dimensional design and selection for end users to satisfy the specific pressure level and wearing comfortable requirements.

CHAPTER 9 CONCLUSIONS AND SUGGESTIONS FOR FUTURE RESEARCH

9.1 Conclusions

In this study, the FE ECS-leg models were proposed to analyze the biomechanical mechanisms of ECS-leg system using the optimized ECS materials, leg geometry models, and tissue properties. This study also proposed the new simulation approach to optimize ECS design for improving compression therapeutic efficacy. The results revealed that the optimized methods can be used to investigate the biomechanical mechanisms of the ECS-leg system and optimize the ECS design with different material properties and dimensions. The mechanical performance of the interface pressure and tissue stress between the lower limb and the ECSs as well as the stress transmission from the skin surface to the underlying bones and deeper tissues (including venous system) was affected by the ECSs with different pressure design. The optimization of the sensitive parameters can assist ECS design to achieve the target pressure levels.

To achieve the proposed research objectives, the following research works have been conducted.

(i) To achieve objective 1 (analyze and determine physical-mechanical properties of ECS fabrics in two- and three-dimensions), a novel approach has been developed to determine the physical-mechanical properties of the ECS materials especially for the numerical simulation and analysis in the both 2D (i.e., along fabric wale and course directions) and 3D scales (i.e., along fabric wale, course, and thickness directions) in Chapter 3. A theoretical analysis and calculation method on the shear modulus of the ECS fabrics in a 3D-scale has been proposed, which described the relationship among the deflection, bending loading, and shear modulus of the ECS fabrics within the course-thickness and wale-thickness planes based on Airy's Stress Function. Based on the both 2D and 3D scale ECS material properties, a FE ECS-Rleg model was constructed to assess the simulation interface pressure deviations. The results revealed that the simulated pressure values of FE-Rleg by using both 2D and 3D ECS material properties were consistent with the measure pressure, especially by using 3D ECS material properties. The simulation precision was improved by using the determined 3D mechanical properties of the ECS fabrics in the ECS-leg system.

(ii) To achieve objective 2 (build finite element model to characterize the mechanical transmission effects of ECS fabrics from the skin to the deeper soft tissues of lower limb), 3D geometric leg-ECS models have been constructed based on the MRI scanning using reverse engineering techniques to simulate the biomechanical properties of the soft tissues, bones, and veins with three subjects aged 40 to 60 yrs old in Chapter 4. Based on the reconstituted geometry model as well as the experimentally determined ECS material properties and both referred and determined tissue properties, 3D FE models have been constructed to analyze mechanical performance of the ECS-leg system in Chapter 5. The developed 3D FE models included the simulation of the interface pressure, tissue stress, and tissue deformation, with the aim to investigate mechanical transmission and deformation distribution within the soft tissues, and to predict biomechanical performance of the lower limb affected by the application of the ECSs with different pressure levels. The tissue stress decreased from the skin surface to the deeper soft tissues till vein walls gradually, which revealed that the larger pressure acted on the GSV and SSV wall, and the less pressure acted on the PV wall. The simulated interface pressures presented a good agreement with the measured values. To further reduce the deviation of the simulation results, a refined subject-specific model has been constructed. The results indicated that the deviations of the simulated interface pressure were reduced by 0.3%.

The simulated interface pressures presented a good agreement with the measured values. The measured and simulated pressure levels (Class-I: 18-21 mmHg; Class-II: 23-32 mmHg; and Class-III: 34-46 mmHg) and the gradient distributions of the studied ECSs satisfied to the RAL-GZ/387 standard. The results demonstrated that the developed 3D FE model through the optimization of the geometry model and material properties contributed to predicting interfacial pressure and stress transmission induced by ECSs in practice.

(iii) To achieve objective 3, 3D FSI models have been constructed based on the 3D FE leg-ECS models and the material properties determined at the stages of (i-ii). The built FSI models simulated the venous hemodynamic responses towards the application of the ECSs with different pressure profiles.

The results indicated that the venous flow was influenced by the external pressure. With the increase of the interface pressure, the venous flow velocities appeared an increased trend under the ECS compression. Among them, the flow velocities of GSV and SSV are greater than those of PV. The coupled FE and FSI models contributed to predicting the interfacial pressure, stress transmission, and hemodynamic responses induced by ECSs, thus facilitating us to understanding in depth the mechanical mechanisms of the ECS-leg system for optimizing the structural design and material properties of the ECSs for an improved effectiveness of compression therapy.

(iv) To achieve objective 4 (develop optimization algorithms to determine the optimal fabric parameters for achieving a balanced mechanical function and wearing comfort of ECSs). Based on the experimental and numerical results obtained from the work conducted in Chapters 5 and 6, parameters optimization and comfort assessment for improving pressure function and fitting for the specific users were performed. Optimization algorithm and a series of calculation and mechanical analysis were conducted to evaluate the effects of the applied material parameters on the pressure magnitudes and wearing comfort sensation in Chapters 7 and 8. Based on the results, the optimal parameter ranges for new ECS design and development in terms of ECS Young's modulus as well as the size of the ECS fabrics and lower limb were determined to achieve the required medical pressure levels in treatment, which provide an optional guidance for structure and material design of ECSs to optimize their practical performance in application.

Research Contributions

Based on our developed FE ECS-leg model and optimization method in the ECS-leg system, the major findings were listed as follow.

(i) The simulated pressure precision of the ECS-leg system can be improved by using the mechanical properties of the ECS fabrics in a 3D-scale.

(ii) The interface pressures predicted by the developed FE models show agreement with the experimental measurements and the pressure standard.

(iii) The maximum interface pressure exists at the anterior ankle section, and gradually decreased from the ankle to the knee.

(iv) The venous velocities of the studied lower limbs with wearing ECS were slightly greater than those without the ECS.

(v) The sensitive parameters (mechanical properties of the ECS fabrics and ECS deformation) can be used to optimize ECSs for achieving the target pressure level.

In summary, this study provides a new FE simulation approach and an optimization system to enhance the understanding of the mechanisms underlying the interactions between elastic compression textiles and the human body, thereby facilitating the optimization design of compression materials and pressure control for the improved compression therapeutic efficacy.

9.2 Suggestions for Future Research

In this study, a simulated ECS-leg system has been constructed and optimized. The deviations of the simulation results have been reduced compared with the previous studies, however, the study limitations remain exist. For example, the microstructure of the ECS fabrics, skin, and muscle were not considered which may cause the simulation deviations, and wall shear stress and venous pressure still need to be investigated to reflect the whole venous hemodynamics responses. The details of the limitations were listed as follow.

In our developed 3D FE ECS-leg model, the ECS tubular was assumed as a shell material without knitted loop structures, which may not reflect micro-effects of materials on the pressure applied at the skin surface and soft tissues, resulting in certain deviation in the simulated pressure values compared to the measured ones.

Considering the volumes of muscles occupies the major proportions of the lower limb soft tissues, the muscular tissues were considered as the tissue properties, while the tissue properties of the thin skin layer were ignored in this numerical study, which may cause certain simulation deviations.

The wall shear stress and venous pressure are not considered and simulated due to the limited measurement technology of the venous pressure and wall shear stress. The results may not fully reflect the venous hemodynamic response towards ECS application in the ECS-leg system.

There lacks of comfort response comparison between healthy people and patients with CVIs, which might only reflect the relationship among the pressure level, comfort response, and posture, rather than the relationship between the pressure level and CVI treatment.

To address the aforementioned limitations, more investigations will be carried out from the several aspects in the future research work.

(i) To further improve FE methods to predict and analyse the mechanical function of ECSs with different structural designs, distinct ECS fabrics will be applied and assessed to determine their physical-mechanical properties in a 3D scale for further verification and optimization of the developed FE models with an improved simulation accuracy. The updated relationships between the stress-strain properties and elastic moduli of the new compressive materials will be obtained by numerical analysis and experimental measurements.

(ii) To further improve FE methods to predict and analyse the mechanical function of tissue properties, a novel method will be applied to determine skin and muscle properties by the shear wave testing. The novel FE ECS-leg model will be constructed to simulate the mechanical responses. The updated simulated interface pressure will be validated to optimize the FE ECS-leg simulation system.

(iii) To further improve FSI models for predicting the biomechanical parameters and their variations (e.g., venous velocity, pressure, and wall shear stress), the physiological responses of the lower limbs towards the applications of ECSs with different structural design will be studied, including interface pressure, tissue stress transfer, and flow performance. These studies would facilitate the selection and determination of the optimized material parameters of the ECSs for the specific users or pressure requirement in practical applications.

(iv) Considering the existing Laplace's law involves only the limited factors influencing pressure magnitudes, more studies would be conducted to further optimize the existed Laplace's law to predict interface pressure between the ECS fabrics and soft tissues with consideration of the mechanical properties of soft tissues and the strains of the ECS fabrics and soft tissues, which can improve the prediction accuracy of the interface pressure using formula-based approach, thus exploring more fast manner to estimate pressure performance and function in material design.

(v) To further evaluate the compression therapeutic efficiency of the ECSs, more subjects with CVIs will be recruited to numerically simulate the mechanical performances of the tissues and veins with time and limb movements, thus, exploring the tissue responses towards the ECS function.

REFERENCES

Akbarzadeh, V., & Hrymak, A. N. (2016). Coupled CFD–DEM of particle-laden flows in a turning flow with a moving wall. *Computers & Chemical Engineering*, 86, 184-191.

Aleti, A., Buhnova, B., Grunske, L., Koziolek, A., & Meedeniya, I. (2012). Software architecture optimization methods: A systematic literature review. *IEEE Transactions on Software Engineerin*g, 39(5), 658-683.

Altuntop, N., Kilik, Z., Ozceyhan, V., & Kincay, O. (2006). Effect of water inlet velocity on thermal stratification in a mantled hot water storage tank. *International Journal of Energy Research*, 30(3), 163-176.

Alves, R. J., Magalhaes, M. D. C., & Carrasco, E. V. M. (2013). Determination of the transverse Young's modulus (TYM) of wood by means of an input power technique. *Construction and Building Materials*, 42, 11-21.

Amans, M. R., Haraldsson, H., Kao, E., Kefayati, S., Meisel, K., Khangura, R., ... & Saloner, D. (2018). MR venous flow in sigmoid sinus diverticulum. *American Journal of Neuroradiology*, 39(11), 2108-2113.

Avril, S., Bouten, L., Dubuis, L., Drapier, S., & Pouget, J. F. (2010). Mixed experimental and numerical approach for characterizing the biomechanical response of the human leg under elastic compression. *Journal of Biomechanical Engineering*, 132(3).

Ayala, A., Guerra, J. D., Ulloa, J. H., & Kabnick, L. (2019). Compliance with compression therapy in primary chronic venous disease: results from a tropical country. *Phlebology*, 34(4), 272-277.

Balcıoğlu, H. E, & Ahmet C. S. (2021) Comparison of machine learning methods and finite element analysis on the fracture behavior of polymer composites. *Archive of Applied Mechanics*, 91, 223-239.

Balea, L., Dusserre, G., & Bernhart, G. (2014). Mechanical behaviour of plain-knit reinforced injected composites: effect of inlay yarns and fibre type. *Composites Part B: Engineering*, 56, 20-29.

Barhoumi, H., Marzougui, S., & Abdessalem, S. B. (2020). Clothing pressure modeling using the modified Laplace's law. *Clothing and Textiles Research Journal*, 38(2), 134-147.

Basford, J. R. (2002). The Law of Laplace and its relevance to contemporary medicine and rehabilitation. *Archives of physical medicine and rehabilitation*, 83(8), 1165-1170.

Beer, F.P (2020). Mechanics of Materials. *New York, NY: McGraw-Hill Education*.

Bini, T. B., Ramakrishna, S., Huang, Z. M., & Lim, C. T. (2001). Structure–tensile property relationship of knitted fabric composites. *Polymer composites*, 22(1), 11-21.

Blemker, S. S., Asakawa, D. S., Gold, G. E., & Delp, S. L. (2007). Image‐based musculoskeletal modeling: applications, advances, and future opportunities. *Journal of Magnetic Resonance Imaging: An Official Journal of the International Society for Magnetic Resonance in Medicine*, 25(2), 441-451.

Bonnefous, O., & Pesque, P. (1986). Time domain formulation of pulse-Doppler ultrasound and blood velocity estimation by cross correlation. *Ultrasonic Imaging*, 8(2), 73-85.

Butros, S. R., Liu, R., Oliveira, G. R., Ganguli, S., & Kalva, S. (2013). Venous compression syndromes: clinical features, imaging findings and management. *The British journal of radiology*, 86(1030), 20130284.

Carbone, V., Fluit, R., Pellikaan, P., Van Der Krogt, M. M., Janssen, D., Damsgaard, M., ... & Verdonschot, N. (2015). TLEM 2.0–A comprehensive musculoskeletal geometry dataset for subject-specific modeling of lower extremity. *Journal of biomechanics*, 48(5), 734-741.

Carr, C. M. (1988). Investigation of the Effect of Water Repellent Finishes on the Mechanical Properties of Textiles Using the Kawabata Evaluation System for Fabrics. *Journal of Coated Fabrics*, 18(2), 106-113.

Chandra, S., & Saini, H. (2021). Computational Fluid Dynamics Analysis of Non Slender Cropped Delta Wingsuit. *Global Journal of Research in Engineering*.

Chen, D., Liu, H., Zhang, Q., & Wang, H. (2013). Effects of mechanical properties of fabrics on clothing pressure. *Przeglad Elektrotechniczny*, 89, 232–235.

Cheng, J. C. Y., Evans, J. H., Leung, K. S., Clark, J. A., Choy, T. T. C., & Leung, P. C. (1984). Pressure therapy in the treatment of post-burn hypertrophic scar—a critical look into its usefulness and fallacies by pressure monitoring. *Burns*, 10(3), 154-163.

Colognesi, V., Ronsse, R., & Chatelain, P. (2021). A model coupling biomechanics and fluid dynamics for the simulation of controlled flapping flight. *Bioinspiration & Biomimetics*.

Courant, R. (1994). Variational methods for the solution of problems of equilibrium and vibrations. *Lecture Notes in Pure and Applied Mathematics*, 1-23.

Dai, X. Q., Liu, R., Li, Y., Zhang, M., & Kwok, Y. L. (2007). Numerical simulation of skin pressure distribution applied by graduated compression stockings. *In Computational Textile*. *Springer, Berlin, Heidelberg*, 301-309.

Dan, R., Fan, X. R., Chen, D. S., & Wang, Q. (2011). Numerical simulation of the relationship between pressure and displacement for the top part of men's socks. *Textile*

Research Journal, 81(2), 128-136.

Dombrowski, S. M., Deshpande, A., Dingwall, C., Leichliter, A., Leibson, Z., & Luciano, M. G. (2008). Chronic hydrocephalus–induced hypoxia: Increased expression of VEGFR-2+ and blood vessel density in hippocampus. *Neuroscience*, 152(2), 346-359.

Downie, S. P., Raynor, S. M., Firmin, D. N., Wood, N. B., Thom, S. A., Hughes, A. D., Parker K. H., Wolfe J.H., & Xu, X. Y. (2008). Effects of elastic compression stockings on wall shear stress in deep and superficial veins of the calf. *American Journal of Physiology-Heart and Circulatory Physiology*, 294(5), H2112-H2120.

Dubuis, L., Avril, S., Debayle, J., & Badel, P. (2012). Identification of the material parameters of soft tissues in the compressed leg. *Computer Methods in Biomechanics and Biomedical Engineering*, 15(1), 3-11.

Dubuis, L., Rohan, C. Y., Avril, S., Badel, P., & Debayle, J. (2013). Patient-specific computational models: Tools for improving the efficiency of Medical Compression Stockings. In Computational Biomechanics for Medicine (pp. 25-37). *Springer, New York*.

Eberhardt, R. T., & Raffetto, J. D. (2014). Chronic venous insufficiency. *Circulation*, 130(4), 333-346.

Eby, S. F., Song, P., Chen, S., Chen, Q., Greenleaf, J. F., & An, K. N. (2013). Validation of shear wave elastography in skeletal muscle. *Journal of biomechanic*s, 46(14), 2381-2387.

Elderman, J. H., Krasznai, A. G., Voogd, A. C., Hulsewé, K. W., & Sikkink, C. J. (2014). Role of compression stockings after endovenous laser therapy for primary varicosis. *Journal of Vascular Surgery: Venous and Lymphatic Disorders*, 2(3), 289-

296.

Elena, C. M. (2019). CEAP Classification of Chronic Venous Disorders: Let’s all speak the same language.

Eren, O., Durur, G., & Cansunar, H. E. (2018). A new technique to measure pressure in medical compression stockings. *Textile Research Journal*, 88(22), 2579-2589.

Figueroa, R. L., Zeng-Treitler, Q., Kandula, S., & Ngo, L. H. (2012). Predicting sample size required for classification performance. *BMC medical informatics and decision making*, 12, 1-10.

Finnie, A. (2000). Interface pressure measurements in leg ulcer management. *British Journal of Nursing*, 9 (Sup1), S8-S18.

Flaud, P., Bassez, S., & Counord, J. L. (2010). Comparative in vitro study of three interface pressure sensors used to evaluate medical compression hosiery. *Dermatologic Surgery*, 36(12), 1930-1940.

Gandzha, S., Aminov, D., & Kosimov, B. (2019). Development of engineering method for calculation of magnetic systems for brushless motors based on finite element method. *International Conference on Industrial Engineering*, IEEE, 1-5.

Gao, L., Parker, K. J., Lerner, R. M., & Levinson, S. F. (1996). Imaging of the elastic properties of tissue—A review. *Ultrasound in medicine & biology*, 22(8), 959-977.

Gercek, H. (2007). Poisson's ratio values for rocks. *International Journal of Rock Mechanics and Mining Sciences*, 44(1), 1-13.

Geng, Z., & Bidanda, B. (2021). Medical applications of additive manufacturing. Bio-materials and prototyping applications in medicine, 97-110.

Gopalakrishnan, K. (2018). Compression Garment Engineering for Health Care Applications.

Gotoh, M. (1977). A theory of plastic anisotropy based on a yield function of fourth order (plane stress state)—I. *International Journal of Mechanical Sciences*, 19(9), 505-512.

Gravouil, A., Elguedj, T., & Maigre, H. (2009). An explicit dynamics extended finite element method. Part 2: Element-by-element stable-explicit/explicit dynamic scheme. *Computer Methods in Applied Mechanics and Engineering*, 198(30-32), 2318-2328.

Harries, C. A., & Pegg, S. P. (1989). Measuring pressure under burns pressure garments using the Oxford Pressure Monitor. *Burns*, 15(3), 187-189.

Hedigalla, D., Ehelagasthenna, M., Nissanka, I. D., Amarasinghe, R., & Nandasiri, G. K. (2022). Numerical Study to Investigate the Pressure Propagation Patterns by a Compression Sleeve with Miniaturised Air-Bladders. *Moratuwa Engineering Research Conference* (MERCon) IEEE, 1-5.

Hinton, E., & Irons, B. (1968). Least squares smoothing of experimental data using finite element. *Strain*.

Hortobágyi, T., & DeVita, P. (2000). Muscle pre-and coactivity during downward stepping are associated with leg stiffness in aging. *Journal of Electromyography and Kinesiology*, 10(2), 117-126.

Hosford, W. F. (2010). Solid Mechanics. *Cambridge: Cambridge UP*.

Hoskins, P. R. (1999). A review of the measurement of blood velocity and related quantities using Doppler ultrasound. *Proceedings of the Institution of Mechanical Engineers, Part H: Journal of Engineering in Medicine*, 213(5), 391-400.

Hrennikoff, A. (1941). Solution of problems of elasticity by the framework method. *Journal of applied mechanics*. 8.4: 169–175.

Hsu, T. R. (2012). The finite element method in thermomechanics. *Springer Science*

& Business Media.

Hu, J., Jiang, Y., & Ko, F. (1998). Modeling uniaxial tensile properties of multiaxial warp knitted fabrics. *Textile Research Journal*, 68(11), 828-834.

Huang, T., Li, J., Xie, Y., Niu, J., & Mak, C. M. (2017). Simultaneous environmental parameter monitoring and human subject survey regarding outdoor thermal comfort and its modelling. *Building and Environment,* 125, 502-514.

Huang, Z. M (2004). Progressive flexural failure analysis of laminated composites with knitted fabric reinforcement. *Mechanics of Materials*, 36.3: 239-260.

Hursa, A., Rolich, T., & Ražić, S. E. (2009). Determining pseudo Poisson's ratio of woven fabric with a digital image correlation method. *Textile Research Journal*, 79(17), 1588-1598.

Hutton, D. V. (2004). Fundamentals of finite element analysis. *McGraw-hill*.

Jamshaid, H., Ahmad, N., Hussain, U., & Mishra, R. (2022). Parametric optimization of durable sheeting fabric using Taguchi Grey Relational Analysis. *Journal of King Saud University-Science*, 34(4), 102004.

Jinyun, Z., Yi, L., Lam, J., & Xuyong, C. (2010). The Poisson ratio and modulus of elastic knitted fabrics. *Textile Research Journal*, 80(18), 1965-1969.

Jungbeck, C., Thulin, I., Darenheim, C., & Norgren, L. (1997). Graduated compression treatment in patients with chronic venous insufficiency: a study comparing low and medium grade compression stockings. *Phlebology*, 12(4), 142-145.

Kahn, S. R., Galanaud, J. P., Vedantham, S., & Ginsberg, J. S. (2016). Guidance for the prevention and treatment of the post-thrombotic syndrome. *Journal of Thrombosis and Thrombolysis*, 41(1), 144-153.

Khaburi, J., Dehghani-Sanij, A. A., Nelson, E. A., & Hutchinson, J. (2011, September). The use of PicoPress transducer to measure sub-bandage pressure. In: *Proceedings of World Academy of Science, Engineering and Technology*, 267-271.

Khan, A. M., Liang, L., Mia, M., Gupta, M. K., Wei, Z., Jamil, M., & Ning, H. (2021). Development of process performance simulator (PPS) and parametric optimization for sustainable machining considering carbon emission, cost and energy aspects. *Renewable and Sustainable Energy Reviews*, 139, 110738.

Kumar, D. S. (2020). Fluid mechanics and fluid power engineering. Springer.

Labropoulos, N., Webb, K. M., Kang, S. S., Mansour, M. A., Filliung, D. R., Size, G. P., ... & Baker, W. H. (1999). Patterns and distribution of isolated calf deep vein thrombosis. *Journal of vascular surgery*, 30(5), 787-793.

Lao, S., Edher, H., Saini, U., Sixt, J., & Salehian, A. (2019). A novel capacitance-based in-situ pressure sensor for wearable compression garments. *Micromachines*, 10(11), 743.

Lattimer, C.R., Kalodiki, E., Azzam, M., & Geroulakos, G. (2016). Haemodynamic performance of low strength below knee graduated elastic compression stockings in health, venous disease, and lymphoedema. *European Journal of Vascular and Endovascular Surgery*, 52(1), 105-112.

Leung, W. Y., Yuen, D. W., Ng, S. P., & Shi, S. Q. (2010). Pressure prediction model for compression garment design. *Journal of burn care & research*, 31(5), 716-727.

Li, H., Priest, A. N., Patterson, I., Graves, M. J., & Lomas, D. J. (2019). Subtractive non‐contrast‐enhanced MRI of lower limb veins using multiple flow-dependent preparation strategies. *Magnetic Resonance in Medicine*, 81(3), 1769-1783.

Li, Y., & Dai, X. Q. (2006). Biomechanical engineering of textiles and clothing.

Woodhead Publishing.

Liang, R., Yip, J., Yu, W., Chen, L., & Lau, N. M. (2019). Numerical simulation of nonlinear material behaviour: Application to sports bra design. *Materials & Design*, 183, 108177.

Liang, R. (2020). Optimization of the comfort of compression sports bras. Dissertation. The Hong Kong Polytechnic University.

Lim, C. S., & Davies, A. H. (2014). Graduated compression stockings. *Cmaj*, 186(10), E391-E398.

Liu, G. R., & Quek, S. S. (2013). The finite element method: a practical course. *Butterworth-Heinemann*.

Liu, R., Kwok, Y. L., Li, Y., Lao, T. T., & Zhang, X. (2005). Effects of material properties and fabric structure characteristics of graduated compression stockings (GCS) on the skin pressure distributions. *Fibers and Polymers*, 6(4), 322-331.

Liu, R., Kwok, Y. L., Li, Y., Lao, T. T., Zhang, X., & Dai, X. Q. (2006). A three-dimensional biomechanical model for numerical simulation of dynamic pressure functional performances of graduated compression stocking (GCS). *Fibers and Polymers*, 7(4), 389-397.

Liu, R., Lao, T. T., Kwok, Y. L., Li, Y., & Ying, M. T. C. (2008). Effects of graduated compression stockings with different pressure profiles on lower-limb venous structures and haemodynamics. *Advances in Therapy*, 25(5), 465-478.

Liu, R., Guo, X., Lao, T. T., & Little, T. (2017). A critical review on compression textiles for compression therapy: textile-based compression interventions for chronic venous insufficiency. *Textile Research Journal*, 87(9), 1121-1141.

Liu, R., Lao, T. T., Little, T. J., Wu, X., & Ke, X. (2018). Can heterogeneous compression textile design reshape skin pressures? *A fundamental study. Textile Research Journal*, 88(17), 1915-1930.

Liu, X., Du, Z., Han, T., Ghista, D. N., Lin, S., Wang, V., ... & Pan, Z. (2018). Quantitative analysis of blood flow in cerebral venous sinus with stenosis by patient-specific CFD modeling. *IEEE Access*, 7, 3848-3854.

Liu, R., Xu, B., & Ye, C. (2020). Biodigital Design and Functional Visualization of Multi-Class Personalized Compression Textiles for Ergonomic Fit. In Advances in Design for Inclusion. Proceedings of the AHFE 2019 International Conference on Design for Inclusion and the AHFE 2019 International Conference on Human Factors for Apparel and Textile Engineering, July 24-28, 2019, Washington DC, USA 10, 488-499. Springer International Publishing.

Lin, Y., Choi, K. F., Zhang, M., Li, Y., Luximon, A., Yao, L., & Hu, J. (2012). An optimized design of compression sportswear fabric using numerical simulation and the response surface method. *Textile Research Journal*, 82(2), 108-116.

Lin, Y. (2011). Computational modeling and mechanical analysis of compression sportswear. Dissertation. The Hong Kong Polytechnic University.

Lyndon, A. E., Crowe, A., Wuensch, K. L., McCammon, S. L., & Davis, K. B. (2019). College students’ stigmatization of people with mental illness: familiarity, implicit person theory, and attribution. *Journal of mental health*, 28(3), 255-259.

Manafi-Khanian, B., Arendt-Nielsen, L., & Graven-Nielsen, T. (2016). An MRI-based leg model used to simulate biomechanical phenomena during cuff algometry: a finite element study. *Medical & biological engineering & computing*, 54(2-3), 315-324.

Ma, Y., Shahsavar, A., Moradi, I., Rostami, S., Moradikazerouni, A., Yarmand, H., & Zulkifli, N. W. B. M. (2019). Using finite volume method for simulating the natural convective heat transfer of nano-fluid flow inside an inclined enclosure with conductive walls in the presence of a constant temperature heat source. *Physica A: Statistical Mechanics and Its Applications*, 123035.

McNaught, A. D., & Andrew. W. (1997). Compendium of Chemical Terminology: IUPAC Recommendations. *Oxford: Blackwell Science*, 1997.

Momota, H., Makabe, H., Mitsuno, T., & Ueda, K. (1993). A study of clothing pressure caused by Japanese men's socks. *Journal-Japan Research Association for Textile end Uses*, 34, 23-23.

Moser, M., & Kenner, T. (1988). Blood flow and blood volume determinations in aorta and in coronary circulation by density dilution. *Basic research in cardiology*, 83, 577-589.

Mosti, G., & Partsch, H. (2010). Duplex scanning to evaluate the effect of compression on venous reflux. *International angiology: a journal of the International Union of Angiology*, 29(5), 416-420.

Muhammad, N., Nadeem, S., & Issakhov, A. (2020). Finite volume method for mixed convection flow of Ag–ethylene glycol nanofluid flow in a cavity having thin central heater. *Physica A: Statistical Mechanics and its Applications*, 537, 122738.

Nossent, J., Elsen, P., & Bauwens, W. (2011). Sobol’ sensitivity analysis of a complex environmental model. *Environmental Modelling & Software*, 26(12), 1515-1525.

Olsen, B. A. (2019). Indo-European syntax in disguise: The Greek type ἱππεύς and related formations. *Indogermanische Forschungen*, 124(1), 279-304.

Partsch, H. (2012). Compression therapy: clinical and experimental evidence. *Annals of Vascular Diseases*, 5(4), 416-422.

Pierrat, B., MacManus, D. B., Murphy, J. G., & Gilchrist, M. D. (2018). Indentation of heterogeneous soft tissue: Local constitutive parameter mapping using an inverse method and an automated rig. *Journal of the mechanical behavior of biomedical materials*, 78, 515-528.

Porteous, M. L., Nicholson, E. A., Morris, L. T., James, R., & Negus, D. (1989). Thigh length versus knee length stockings in the prevention of deep vein thrombosis. *British Journal of Surgery*, 76(3), 296-297.

Rabe, E., Hertel, S., Bock, E., Hoffmann, B., Jöckel, K. H., & Pannier, F. (2013). Therapy with compression stockings in Germany–results from the Bonn Vein Studies. *JDDG: Journal der Deutschen Dermatologischen Gesellschaft*, 11(3), 257-261.

Raju, S., Hollis, K., & Neglen, P. (2007). Use of compression stockings in chronic venous disease: patient compliance and efficacy. *Annals of Vascular Surgery*, 21(6), 790-795.

Ramakrishna, S. (1997). Analysis and modeling of plain knitted fabric reinforced composites. *Journal of Composite Materials*, 31(1), 52-70.

Raous, J., Moreau, R. M., & Jean, M. (1995). Contact Mechanics. New York: Plenum.

Rhodes, J. M., Gloviczki, P., Canton, L. G., Rooke, T., Lewis, B. D., & Lindsey, J. R. (1998). Factors affecting clinical outcome following endoscopic perforator vein ablation. *The American Journal of Surgery*, 176(2), 162-167.

Rohan, C. Y., Badel, P., Lun, B., Rastel, D., & Avril, S. (2013). Biomechanical response of varicose veins to elastic compression: a numerical study. *Journal of Biomechanics*, 46(3), 599-603.

Rohan, P. Y., Badel, P., Lun, B., Rastel, D., & Avril, S. (2015). Prediction of the biomechanical effects of compression therapy on deep veins using finite element modelling. *Annals of Biomedical Engineering*, 43(2), 314-324.

Ruan, X., & Chou, T. W. (1996). Experimental and theoretical studies of the elastic behavior of knitted-fabric composites. *Composites Science and Technology*, 56(12), 1391-1403.

Saltelli, A., Ratto, M., Tarantola, S., & Campolongo, F. (2006). Sensitivity analysis practices: Strategies for model-based inference. *Reliability engineering & system safety*, 91(10-11), 1109-1125.

Shi, Y., Lawford, P., & Hose, R. (2011). Review of zero-D and 1-D models of blood flow in the cardiovascular system. *Biomedical Engineering Online*, 10(1), 1-38.

Shi, Y., Liu, R., & Lv, J. (2023). Effects of Knitting Variables for Pressure Controlling of Tubular Compression Fabrics. *International Journal of Materials and Textile Engineering*, 17(7), 90-94.

Sigovan, M., Rayz, V., Gasper, W., Alley, H. F., Owens, C. D., & Saloner, D. (2013). Vascular remodeling in autogenous arterio-venous fistulas by MRI and CFD. *Annals of Biomedical Engineering*, 41(4), 657-668.

Silva, D., & Clarence, W (2014). Mechanics of Materials. *Boca Raton: CRC/Taylor & Francis Group*.

Sitharam, T.G., Govindaraju, L (2021). Theory of Elasticity, first ed., Springer Singapore.

Smith, P. C., Hasty, J. H., & Scurr, J. H. (1991). Deep vein thrombosis: effect of graduated compression stockings. *British Journal of Surgery*, 78(6).

Spurk, A., & Aksel, N. (2020). Fluid Mechanics. *Cham: Springer*, 2020.

Stolk, R., Wegen Van Der‐Franken, C. P. M., & Neumann, H. A. M. (2004). A method for measuring the dynamic behavior of medical compression hosiery during walking. *Dermatologic Surgery*, 30(5), 729-736.

Stuart, B., Drumm, J., Fitzgerald, D. E., & Duignan, N. M. (1980). Fetal blood velocity waveforms in normal pregnancy. BJOG: *An International Journal of Obstetrics & Gynaecology*, 87(9), 780-785.

Sun, G., Yang, L., Wang, W., Zhang, S., Luo, Z., Wu, G., ... & Li, X. (2020). An Algorithm for the Noninvasive and Personalized Measurement of Microvascular Blood Viscosity Using Physiological Parameters. *BioMed Research International*, 2020.

Sun, H., Pan, N., & Postle, R. (2005). On the Poisson's ratios of a woven fabric. *Composite Structures*, 68(4), 505-510.

Swillens, A., Degroote, J., Vierendeels, J., Lovstakken, L., & Segers, P. (2010). A simulation environment for validating ultrasonic blood flow and vessel wall imaging based on fluid‐structure interaction simulations: Ultrasonic assessment of arterial distension and wall shear rate. *Medical Physics*, 37(8), 4318-4330.

Tabata, T., Thomas, J. D., & Klein, A. L. (2003). Pulmonary venous flow by Doppler echocardiography: revisited 12 years later. *Journal of the American College of Cardiology*, 41(8), 1243-1250.

Tandler, S. F. (2016). Challenges faced by healthcare professionals in the provision of compression hosiery to enhance compliance in the prevention of venous leg ulceration. *EWMA Journal*, 16(1).

Thomaszewski B, Wacker M, Stradber W. A consistent bending model for cloth simulation with corotational subdivision finite elements. *Europgraphics/ACM SIGGRAPH Symposium on Computer Animation*, 2006.

Toya, K., Takahashi, T., Fujimoto, Y., Nishimoto, T., Takasoh, T., Sasano, K., &

Kusaka, S. (2016). Effect of elastic stockings and ankle positions on the blood velocity in the common femoral vein. *Journal of Physical Therapy Science*, 28(9), 2608-2610.

Turl, L. H. (1956). The measurement of tearing strength of textile fabrics. *Textile Research Journal*, 26(3), 169-176.

Van, T. (2007). A new fracture mechanics theory for orthotropic materials like wood. *Engineering Fracture Mechanics*, 74(5), 771-781.

Wang, C. H., Feng, Y. Y., Yue, K., & Zhang, X. X. (2019). Discontinuous finite element method for combined radiation-conduction heat transfer in participating media. *International Communications in Heat and Mass Transfer*, 108, 104287.

Wang, S. M., & Hu, Z. J. (2007). The present status and development of clinical research on venous surgery in China. *In: Proceedings-Chinese Symposium for Medical Research Methods and Cross Knowledge Innovation*, Guangzhou, China, 2007, 23–35.

Wang, X., Du, Z., Chen, Y., Li, S., Lan, D., Wang, G., & Chen, Y. (2008). An autonomic provisioning framework for outsourcing data center based on virtual appliances. *Cluster Computing*, 11, 229-245.

Wang, Y., Downie, S., Wood, N., Firmin, D., & Xu, X. Y. (2013). Finite element analysis of the deformation of deep veins in the lower limb under external compression. *Medical Engineering & Physics*, 35(4), 515-523.

Watson, R. E. (2015). Lessons learned from MRI safety events. *Current Radiology Reports*, 3, 1-7.

Wei, K., Jayaweera, A. R., Firoozan, S., Linka, A., Skyba, D. M., & Kaul, S. (1998). Quantification of myocardial blood flow with ultrasound-induced destruction of microbubbles administered as a constant venous infusion. *Circulation*, 97(5), 473-483.

Wei, W., Shen, J., Yu, H., Chen, B., & Wei, Y. (2021). Optimization design of the lower rocker arm of a vertical roller mill based on ANSYS workbench. *Applied Sciences*, 11(21), 10408.

Williams, A. M., Rhys-Davies, P., & Sweetham, D. (1994). Graduated compression stockings in the prevention of deep vein thrombosis and the case for knee length versus thigh length stockings. *Journal of Bone and Joint Surgery-British Volume*.

Ye, C., Ali, S., Sun, Q., Guo, M., Liu, Y., Gao, Y., & Huo, B. (2019). Novel cone-and-plate flow chamber with controlled distribution of wall fluid shear stress. *Computers in biology and medicine*, 106, 140-148.

Yu, A., Yick, K. L., Ng, S. P., Yip, J., & Chan, Y. F. (2016). Numerical simulation of pressure therapy glove by using finite element method. *Burns*, 42(1), 141-151.

Yu, V., Yu Kirill, Ovcharenko E, et al. (2019). Finite element analysis-based approach for prediction of aneurysm-prone arterial segments. *J. Med. Biol. Eng.* 39**,** 102–108.

Zednik, C., & Jakel, F. (2014). How does Bayesian reverse-engineering work? *In Proceedings of the Annual Meeting of the Cognitive Science Society* (Vol. 36, No. 36).

Zhang, L., Sun, G., Li, J., Chen, Y., Chen, X., Gao, W., & Hu, W. (2019). The structure and pressure characteristics of graduated compression stockings: experimental and numerical study. *Textile Research Journal*, 89(23-24), 5218-5225.

Zhang, P., Li, Y., Tang, Y., Zhang, R., Li, H., & Gu, J. (2023). Multi-objective optimization and dynamic response predictions of an articulated offshore wind turbine. *Ocean Engineering*, 273, 114017.

Zhang, X., Yeung, K. W., & Li, Y. (2002). Numerical simulation of 3D dynamic garment pressure. *Textile Research Journal*, 72(3), 245-252.

Zhao, Y., Ping, J., Yu, X., Cui, Y., Yin, J., Sun, C., ... & Tang, L. (2021). Computational fluid dynamics simulation of time-resolved blood flow in Budd-Chiari syndrome with inferior vena cava stenosis and its implication for postoperative efficacy assessment. *Clinical Biomechanics*, 82, 105256.